DISSERTATION

COLD POOL PROCESSES IN DIFFERENT ENVIRONMENTS

Submitted by

Leah Danielle Grant

Department of Atmospheric Science

In partial fulfillment of the requirements

For the Degree of Doctor of Philosophy

Colorado State University

Fort Collins, Colorado

Spring 2018

Doctoral Committee:

    Advisor: Susan C. van den Heever

    David A. Randall
    Steven A. Rutledge
    Jeffrey D. Niemann

ABSTRACT

COLD POOL PROCESSES IN DIFFERENT ENVIRONMENTS

Cold pools are localized regions of dense air near Earth's surface. They form in association with precipitating clouds in many environments ranging from moist tropical to semi-arid continental conditions, and they play important roles in weather in climate. The overarching goal of this dissertation research is to improve our process-level understanding of cold pool interactions with different components of the Earth system, focusing on two key knowledge gaps: (1) interactions with Earth's surface in continental environments; and (2) interactions with organized convective systems in tropical oceanic environments.

The primary goal of the first study conducted in this dissertation is to evaluate how surface sensible heat fluxes impact cold pool dissipation in dry continental environments via two pathways: (a) by directly heating the cold pool, and (b) by changing mixing rates between cold pool air and environmental air through altering turbulence intensity. Idealized 2D simulations of isolated cold pools are conducted with varying sensible heat flux formulations to determine the relative importance of these two mechanisms. The results demonstrate that the impact of sensible heat fluxes on mixing, i.e. mechanism (b), contributes most significantly to cold pool dissipation.

Cold pool – land surface interactions in semi-arid continental conditions are investigated in the second study. Two questions are addressed: (1) how does the land surface respond to the cold pool; and (2) to what extent do land surface feedbacks modulate the cold pool evolution? Idealized 3D simulations of a cold pool evolving in a turbulent boundary layer are conducted to answer these questions. The land surface cools in response to the cold pool, resulting in

suppressed sensible heat fluxes in the center of the cold pool. However, sensible heat fluxes are enhanced near the edge of the cold pool in association with higher wind speeds, leading to cold pool dissipation from the edge inwards. The land surface interactions are shown to strongly affect the cold pool, reducing its lifetime, size, and intensity by up to 50%.

Preliminary analysis of a cold pool that was observed in northeastern Colorado on 17 May 2017 ("The Bees Day") during the C^3LOUD-Ex field campaign is presented in the third study. The observed case exhibits similar environmental and cold pool characteristics to the first two numerical studies, thereby providing observational context for their hypotheses and conclusions.

The objective of the fourth study presented in this dissertation is to determine the role of cold pools in organized tropical oceanic convective systems. To address this goal, two convective systems embedded in a weakly sheared cloud population approaching radiative-convective equilibrium are simulated at high resolution. The cold pools are weakened in the sensitivity tests by suppressing evaporation rates below cloud base. Both of the convective systems respond in a consistent manner as follows: (a) when cold pools are weakened, the convective intensity increases; and (b) the mesoscale structure, propagation speeds, and system lifetimes are insensitive to the changes in the cold pools, in contrast to the prevailing (RKW) theory that cold pools are critical to the mesoscale organization of convective systems.

In summary, these high-resolution modeling and observational studies demonstrate new insights into cold pool – surface – convection interactions. The results suggest that cold pool interactions with different components of the Earth system are not all created equally; rather, these interactions depend on the environment in which the cold pools find themselves.

ACKNOWLEDGEMENTS

Many people deserve acknowledgement for their inspiration and support as I worked toward completion of this dissertation. First and foremost, I would like to thank my adviser, Dr. Susan van den Heever, for her outstanding guidance throughout my graduate studies. Sue has expertly cultivated in me a confident and independent scientist with a great passion for thought-provoking, exciting, novel, and high-quality science. I could not imagine graduate school with any other adviser, and I look forward to the many years of collaboration and friendship ahead.

I thank my doctoral committee, Drs. David Randall, Steven Rutledge, Jeffrey Niemann, and Subhas Karan Venayagamoorthy for their time in serving on my committee and for their valuable suggestions to improve both the science and the writing in this dissertation.

I would like to acknowledge fruitful and productive discussions with many colleagues. I thank Dr. Todd Lane for hosting my three-month visit to the University of Melbourne and for enlightening me about tropical convection and the enigmas of gravity waves. I thank everyone on the C^{3}LOUD-Ex team for working with me as I learned to navigate the position of Project Manager: Sue van den Heever (PI) for providing unending encouragement, excitement, and focus on the science; Sean Freeman (Technical Manager) for many hours of effort devoted to all technical aspects of the field work, particularly the drones; Peter Marinescu (Operations Manager) for overseeing the day-to-day tasks; Jennie Bukowski for detailed attention to and care for the surface stations; Chris Slocum for leading the operations team and for excellent forecasts in combination with Erik Nielsen and Greg Herman; to the entire field crew including Julie Barnum, Ellie Delap, Aryeh Drager, Brody Fuchs, Stacey Hitchcock, Minnie Park, Kristen Rasmussen, Naufal Razin, Ryan Riesenburg, Emily Riley, Ben Toms, and those people already

iv

mentioned above for hard work and devoted effort to ensuring each field day was as successful as it could be; and last but not least, Pat Kennedy for operating CHILL and tolerating our at times unpredictable schedules. Many thanks as well to members of the van den Heever research group for always being available and willing to entertain discussions about cloud processes and convection, including many who have already been listed above for their involvement in C^3LOUD-Ex; my officemate for more than five years, Adele Igel, who was an endless sounding board for ideas, discussions, and laughs; my new officemate, Stacey Kawecki, for fresh ideas and countless generous gifts of coffee and tea; and Research Associates Steve Saleeby and Steve Herbener for cooperative, collaborative, and at times hair-pulling efforts regarding RAMS. I thank Mitch Moncrieff for enlightening discussions about tropical convection and cold pools.

I gratefully acknowledge the University Distinguished Professors Scholarship and am deeply thankful to my nominator for this award, Sue van den Heever. This scholarship opened new exciting opportunities and made possible my travel to the Understanding Clouds and Precipitation conference in Berlin, Germany, which provided inspiration for some of the conclusions to this dissertation. I also thank the CSU ATS department staff, without whom travel arrangements and day-to-day activities of the department would not be possible.

Finally, I thank my family, especially my parents, and my friends from prior walks of life and at CSU, who have cheered for me and supported me along this journey. Most of all, I thank Peter for his unwavering support, for being a constant source of inspiration and encouragement, and for never failing to make me laugh.

TABLE OF CONTENTS

CHAPTER 1: INTRODUCTION

1.1. A brief history of cold pools

The first collection of observations of cold pools associated with thunderstorms appears in the final report of The Thunderstorm Project, *The Thunderstorm* (Byers and Braham 1949). Byers and Braham referred to the region of cool and gusty air that spread out below the base of thunderstorms as "cold domes." The characteristics of these cold domes were primarily determined from a network of surface stations in Florida and Ohio and by occasional radiosonde launches. We now know these cold domes as cold pools, outflows, or density currents, and their leading edges as gust fronts. Byers and Braham remarked that the "discontinuity zone, which everywhere marks the limit of the cold downdraft air, is one of the most interesting of all surface weather features associated with the thunderstorm passage." Subjectively, this statement holds as true today as it did then because the leading edges of cold pools do indeed interact with the atmosphere and the land surface in interesting ways.

Cold pools are often modeled as density currents. Density currents are characterized by a deeper head region near the current's front and a shallower tail region; wave breaking and mixing occurs behind the head (Figure 1.1). Benjamin (1968) used steady fluid theory to demonstrate why the wave-breaking behind the head is ubiquitous in density currents. He also described the theoretical propagation speed of the current, which is related to the pressure gradient force and hence to the density contrast between the two fluids and the current depth. The theoretical speed therefore characterizes the overall density current strength and is widely used in studies of cold pools for this reason.

Early density current studies were largely theoretical (as in Benjamin 1968) or utilized laboratory tank experiments (e.g. Keulegan 1958; Simpson 1969; Britter and Simpson 1978). Laboratory tanks led to significant advancements in understanding the behavior and characteristics of density currents (Figure 1.1), including documentation of the head, tail, and wave breaking (Keulegan 1958); internal flow (Middleton 1966); lobe and cleft structure (Simpson 1969); and the influence of ambient turbulence (Linden and Simpson 1986). Although theory neglects effects such as mixing, and laboratory tank experiments cannot investigate Reynolds numbers high enough to represent atmospheric flows, observations of cold pools associated with thunderstorms have been shown to agree well with density current theory and laboratory tank behavior (Charba 1974; Wakimoto 1982). Charba's study of a severe gust front associated with an Oklahoma squall line was the first to compare observations to laboratory experiments and theory. Charba documented the deeper head and shallower tail region and the internal flow within the squall line's cold pool, inferred mixing behind the head, and found agreement between the observed and theoretical propagation speeds.

One of the earliest numerical modeling studies that adequately represented the fine scale structure of density currents was that by Droegemeier and Wilhelmson (1987). They showed that 100 m grid spacings were required to simulate the Kelvin-Helmholtz waves. They also examined controls on the propagation speed, depth, internal temperature structure and circulation, and turbulent characteristics, and compared their numerical results to theory and laboratory studies. This study set the stage for further investigations of atmospheric cold pools using numerical models. Models can represent significantly more complex scenarios than can be treated theoretically or in laboratory tanks including ambient stratification and wind shear; the influence of microphysical processes; and interactions with convection and Earth's surface.

Understanding cold pool processes and their sensitivities to and interactions with their environment, Earth's surface, and convection (Figure 1.1) is important because cold pools play a number of critical roles in the atmosphere with subsequent impacts on society. A few of these important roles are shown in Figure 1.2. Cold pools can be associated with severe winds that pose aviation and other societal hazards (Fujita 1978; Johns and Doswell 1992). Cold pools and cold pool collisions can initiate convection (Purdom 1976; Tompkins 2001; see Figure 1.2). Cold pools can also impact the structure and maintenance of organized convective systems (Rotunno et al. 1988), control convective system propagation speeds (Nicholls et al. 1988; Lane and Moncrieff 2015), and play a role in the transition from shallow to deep convection (Khairoutdinov and Randall 2006) and cloud mergers (Simpson et al. 1980). Surface winds within cold pools loft significant amounts of dust (Miller et al. 2008; Seigel and van den Heever 2012a; see Figure 1.2). Cold pools interact with boundary layer features (Achtemeier 1991), influence to the climatology of dry regions (Garcia-Carreras et al. 2013), and impact and the surface energy budget of tropical oceanic regions (Chuda et al. 2008). Several of these important roles of cold pools, and how they vary in different environments, are next examined in greater detail.

1.2. Importance of cold pools in different environments

Byers and Braham (1949) surmised that cold pools and their collisions could initiate new convection based on the observations from The Thunderstorm Project. Subsequent studies have documented this important role of cold pools, using both observations and numerical simulations (Purdom 1976, 1982; Droegemeier and Wilhelmson 1985; Wilson and Schreiber 1986; Tompkins 2001; Khairoutdinov and Randall 2006; Lima and Wilson 2008). Convective initiation

requires three basic ingredients: moisture, instability, and a lifting mechanism (Doswell 1987; Johns and Doswell 1992). The circulation associated with the cold pool head results in low-level ascent, and observations have reported that the strength of this ascent can reach 10 m s^{-1} (Wakimoto 1982; Martner 1997). Moreover, the ascent branch typically occurs outside of the cold pool and therefore lifts the warmer environmental air. It logically follows that cold pools influence convective initiation via the third ingredient, a lifting mechanism. An example of mechanical lifting-induced new cloud formation can be seen in Figure 1.2. Many studies (Thorpe et al. 1982; Rotunno et al. 1988; Xu 1992; Liu and Moncrieff 1996; etc.) have also discussed the effects of wind shear on the cold pool-induced lifting. Namely, when the environment contains horizontal vorticity associated with vertical shear of the horizontal winds, the vorticity associated with the cold pool's head circulation and the vorticity in the environment oppose one another on the downshear side of the cold pool. Resultant lifting by the cold pool is deeper and more upright than when wind shear is not present. These studies of cold pool – wind shear interactions have mainly been conducted for midlatitude conditions with shear magnitudes that are generally too large for tropical environments.

As mentioned, there are two other ingredients for convective initiation: moisture and instability. Using idealized simulations of cold pools over a tropical ocean with no wind shear, Tompkins (2001) postulated that cold pools influence convective initiation in these environments via their influence on the other two ingredients. Specifically, Tompkins demonstrated that the cold pools contained a ring of enhanced moisture within the head region. When the cold pools dissipated and their negative buoyancy anomaly disappeared, the remnant rings of moisture and the associated elevated instability relative to the surroundings were preferred regions of convective initiation. Tompkins' theory has sparked further investigations into this

4

thermodynamical initiation mechanism and its importance relative to the mechanical lifting, as well as processes leading to the moisture ring (e.g. Torri et al. 2015; Langhans and Romps 2015; Schlemmer and Hohenegger 2016; Torri and Kuang 2016b).

It therefore appears that the mechanism by which cold pools initiate convection may depend on whether the cold pool finds itself in the tropics or in midlatitudes. The efficiency of the mechanisms and their relative importance may also depend on environmental parameters that vary between the tropics and midlatitudes and/or between ocean and land surfaces. As discussed above, wind shear varies substantially from the tropics to the midlatitudes, and wind shear is known to influence the cold pool's head circulation. Atmospheric stability also varies in different environments. Low-level stability is especially sensitive to the heat capacity and therefore to the moisture content of the surface. Both shallow- and deep-layer stability affect the cold pool's propagation speed, its head height, and the strength and vertical extent of the head circulation (Thorpe et al. 1980; Jin et al. 1996; Liu and Moncrieff 2000; Seigel and van den Heever 2012b). Such sensitivities are relevant for both of the potential convective initiation mechanisms discussed above, as are changes to latent cooling rates that influence the magnitude and longevity of the cold pool's negative buoyancy anomaly. Humidity, microphysical processes, and aerosols regulate latent cooling rates. Humidity in the tropics is generally much higher than in midlatitudes, thus limiting evaporation potential and leading to weak cold pools (e.g. Lane and Moncrieff 2015; Moncrieff and Lane 2015). Since evaporation rates are also sensitive to hydrometeor surface areas and hence to their size distributions, changes to rain and hail sizes can influence the cold pool strength (Gilmore et al. 2004; van den Heever and Cotton 2004; Dawson et al. 2010; Seigel and van den Heever 2013). Aerosols are one mechanism that can alter microphysical size distributions, evaporation rates and cold pool strengths in different

environments (Tao et al. 2007; van den Heever and Cotton 2007; Storer et al. 2010; Morrison 2012; Grant and van den Heever 2015) because aerosols vary widely in concentration and composition throughout different regions of the world.

Another often-discussed role of cold pools is their influence on organized convective systems, which typically occur in environments containing wind shear. Thorpe et al. (1982) recognized that the influence of wind shear on the behavior of cold pools is an important consideration for organized convection. Rotunno et al. (1988) put forth what is now termed "RKW theory" regarding the structure and intensity of linearly-oriented convective systems (squall lines). RKW theory states that the vorticity balance between the cold pool's circulation on its downshear side and the vorticity associated with the low-level environmental wind shear influences the tilt, structure, and intensity of squall lines. When the cold pool's vorticity is stronger than the environmental vorticity, the squall line tilts back over the cold pool (a trailing-stratiform system); conversely, when the environmental vorticity is stronger than the cold pool's vorticity, the squall line tilts forward relative to its propagation direction (a leading-stratiform system). The goldilocks scenario, or "optimal state", occurs when the two circulations are of equal magnitude, resulting in the most upright and intense squall line. Rotunno et al. stated that their theory should explain the physics of both midlatitude and tropical squall lines.

Despite some shortfalls, RKW theory has been successfully applied in numerous studies of midlatitude squall lines, both in simulations (e.g. Parker and Johnson 2004b; Weisman and Rotunno 2004; Bryan et al. 2006; Trier et al. 2006) and in observations (e.g. Bluestein and Jain 1985; Bryan et al. 2005; Weisman and Rotunno 2005; Bryan and Parker 2010; Billings and Parker 2012). Some studies of tropical systems have also demonstrated behavior that appears to be consistent with RKW thinking (Nicholls et al. 1988; Keenan and Carbone 1992; Robe and

Emanuel 2001). However, not all linearly oriented tropical convective systems conform to RKW theory. Webster et al. (2002) and Aves and Johnson (2008) documented tropical convective systems in which the cold pool's propagation speeds were too slow to explain the speeds of the convective systems. Other investigations documented tropical convective systems whose propagation direction, system orientation, and/or region of preferred convective development were not located on the downshear side of the cold pool, as would be expected from RKW theory (Moncrieff and Miller 1976; Johnson et al. 2005; Lane and Moncrieff 2015; Liu and Moncrieff 2017). Overall, it appears that the mechanisms by which cold pools interact with organized convective systems may stray most often from RKW theory in tropical environments.

A third important role of cold pools that varies in different environments is their interaction with Earth's surface. Cold pools can affect the surface energy budget, while surface fluxes within cold pools can in turn alter the cold pool characteristics. Enhanced surface sensible heat fluxes in the cold pool will warm the cold pool and shorten its lifetime, while surface latent heat fluxes will add moisture to the cold pool. Momentum fluxes will influence the cold pool turbulence, which could impact the amount of entrainment into the cold pool. All of these effects may influence the cold pools' roles in convective initiation and organization discussed above, as well as their other effects described in section 1.1.

Over tropical oceans, since the SST is approximately constant throughout the lifetime of a cold pool, the presence of cooler, gusty, and generally drier conditions within the cold pool enhances both the sensible and latent heat fluxes. This effect has been documented in observations of isolated cold pools and in cold pools associated with organized convective systems, both in observational datasets from different field campaigns (Johnson and Nicholls 1983; Young et al. 1995; Saxen and Rutledge 1998; de Szoeke et al. 2017) and in simulation

results (Jabouille et al. 1996; Trier et al. 1996; Tompkins 2001; Ross et al. 2004; Feng et al. 2015; Langhans and Romps 2015). Over land, there are as yet no observational papers documenting how surface fluxes are perturbed within cold pools, and very few numerical modeling studies have discussed cold pool – surface flux interactions. Del Genio et al. (2012) simulated tropical convection over northern Australia and found that the land surface cooled in response to the cold pools' presence, which then shut down the sensible heat fluxes in the cold pools. As a result, the cold anomaly in the cold pools persisted until the environment cooled as nightfall approached. Drager and van den Heever (2017) also documented spatial and temporal variability in sensible and latent heat fluxes within cold pools in a tropical continental environment. They found that latent heat fluxes were enhanced but sensible heat fluxes suppressed in the cold pool center where rainfall from the parent convection had cooled and soaked the ground. These initial studies demonstrate that cold pool – surface interactions are more complicated over land than over ocean, and they will depend strongly on factors that influence the partitioning between sensible and latent heat fluxes such as soil moisture, soil temperature, vegetation type, and surface roughness. Therefore, cold pool – surface interactions should vary between ocean and land, between the tropics and midlatitudes, and even diurnally and seasonally.

In summary, there is evidence that three important aspects of cold pools – their ability to initiation convection, their influence on organized convective system intensity and structure, and their interactions with Earth's surface – are sensitive to environmental conditions and surface characteristics. Misrepresenting these interactions in numerical weather prediction models will hinder forecasts of convection with implications for their societal impacts. Furthermore, global models somehow need account for these significant cold pool effects. As such, efforts to develop

and improve parameterizations of cold pools have been undertaken in recent years (Qian et al. 1998; Mapes 2000; Rio et al. 2009; Grandpeix and Lafore 2010; Hohenegger and Bretherton 2011; Park 2014; Schlemmer and Hohenegger 2014; Del Genio et al. 2015). Cold pool parameterizations must be able to handle cold pool – convection – surface interactions in different environments. However, parameterizations cannot be improved without a complete process-level understanding of the extent to which cold pool interactions with convection and the surface depend on the environment.

1.3. Dissertation outline: Research objectives and key findings

The overarching goal of the research in this dissertation is to increase our process-level understanding of cold pool interactions with Earth's surface and with convection in continental and tropical oceanic environments, as summarized in Figure 1.1. Many outstanding questions remain regarding these interactions. How important is it that we distinguish between different surface types (e.g. water versus land; dry versus wet soils) and environments (tropics versus midlatitudes; oceanic versus continental; etc.) when considering cold pool-induced convective initiation and organization? How do cold pools interact with the land surface, and to what extent does this depend on the land surface properties? How do cold pools influence convection in the tropics? What observations are still necessary to evaluate cold pool process studies? These questions form the core motivation of this dissertation research.

Chapter 2 and Chapter 3 focus on cold pool – land surface interactions in semi-arid continental environments using idealized numerical experiments, with particular attention being paid to sensible heat fluxes. In Chapter 4, preliminary results from a case study observed during the C^3LOUD-Ex (CSU Convective CLoud Outflows and UpDrafts Experiment; van den Heever

9

et al. 2017, in prep.) field campaign are presented and related to the findings from the land surface studies. Chapter 5 turns to tropical oceanic environments, and the physical mechanisms by which cold pools impact organized convective systems are explored in idealized simulations. Finally, the studies are summarized in Chapter 6, and implications and future work are discussed.

In Chapter 2[1], a systematic investigation into the physical mechanisms by which surface sensible heat fluxes (SHFs) impact cold pool dissipation is conducted using idealized, two-dimensional numerical simulations and conditions characteristic of a semi-arid, continental, daytime environment. SHFs contribute to cold pool dissipation (a) by direct surface heating when SHFs are enhanced within the cold pool; and (b) by generating turbulent kinetic energy (TKE) in the environment and hence increasing mixing rates between the cold pool air and the environmental air. These two mechanisms and their relative importance are explored by varying the SHF formulation under the assumption of a fixed land surface temperature. Additionally, the grid spacings are systematically coarsened to investigate the resolution dependence of the two SHF mechanisms. The key findings from this study are the following: (1) the mixing effect of SHFs has a larger impact on the cold pool dissipation than the direct heating effect; and (2) horizontal and vertical grid spacings coarser than 100 m and 50 m, respectively, cannot properly represent the SHF effects on cold pool evolution.

The study presented in Chapter 3[2] addresses two questions in the context of a daytime, semi-arid continental environment: (1) how does the land surface respond to a cold pool in the

---

[1] This study, titled "Cold Pool Dissipation," has been published in *Journal of Geophysical Research: Atmospheres* (Grant and van den Heever 2016; © 2016 American Geophysical Union); the pre-typeset and copyedited version appears in this dissertation.

[2] The results from this study are currently in review at *Geophysical Research Letters* in a paper titled, "Cold Pool – Land Surface Interactions in a Dry Continental Environment" (Grant and van den Heever 2017, submitted).

absence of cloud effects such as precipitation and anvil shading? and (2) how do interactions between the land surface and the cold pool influence the subsequent evolution of the cold pool and the boundary layer? Two idealized, three-dimensional simulations of a cold pool evolving into a convective boundary layer are performed to address these questions; one simulation utilizes an interactive land surface while the other uses imposed, spatially homogeneous surface fluxes. The main findings from this study are: (1) SHFs are enhanced near the edge of the cold pool and suppressed in the center, leading to cold pool dissipation from the edge inwards; and (2) the use of an interactive land surface substantially reduces the cold pool speed, extent, and lifetime, and alters the resultant boundary layer structure compared to the imposed surface flux case. These results have significant implications for the representation of cold pool – land surface interactions in numerical models.

Preliminary analysis of a cold pool case that was observed in May 2017 in northeastern Colorado during C^{3}LOUD-Ex (van den Heever et al. 2017, in prep.) is discussed in Chapter 4[3]. Radar, sounding, and surface station measurements of the observed cold pool demonstrate that its environment and the cold pool characteristics are similar to those in the numerical continental cold pool studies discussed in Chapter 2 and Chapter 3. The observations therefore lend support to the conclusions drawn in the two cold pool – land surface studies regarding the importance of mixing and interactions with the land surface. Additionally, the simulation results provide intuition into process explanations of trends and features seen in the observations.

---

[3] This preliminary observational analysis is part of a larger study titled "Midlatitude cold pool variability from C^{3}LOUD-Ex observations" (Grant et al. 2017b, in prep.) which will be submitted to *Journal of the Atmospheric Sciences*.

The main objective of the study presented in Chapter 5[4] is to address the question, how do cold pools influence organized tropical oceanic convective systems, including characteristics such as their intensity, mesoscale structure, and propagation? In order to address this question, idealized simulations of two convective systems are conducted, one being linearly oriented and the other organized into a cluster. The cold pools are altered by changing evaporation rates in the sub-cloud layer. The sensitivity tests demonstrate that when the cold pools are weakened, the convection surprisingly intensifies in both systems, suggesting that the cold pools are not playing a role in convective initiation. The convective systems' propagation and mesoscale structure are also insensitive to the changes in the cold pools. Therefore, it is concluded that (1) cold pools weaken convective intensity by virtue of their initial negative buoyancy because cold pool air is transported within the updrafts; and (2) large-scale gravity waves, rather than the cold pools, modulate the convective systems' mesoscale structure and propagation speeds. The application of RKW theory to organized tropical convection, even in linearly oriented systems, is ultimately challenged.

Finally, a summary of this dissertation research and a synthesis of the findings and implications are presented in Chapter 6. Implications for high-resolution numerical and observational studies are pondered, and opportunities for observational evaluation of cold pool – surface interactions and cold pool – convective system interactions in both tropical continental and oceanic environments are discussed in the context of two upcoming field campaigns.

---

[4] This study, which is co-authored by T.P. Lane, is called "The Role of Cold Pools in Tropical Oceanic Convective Systems" (Grant et al. 2017a, submitted) and is currently under review in the *Journal of the Atmospheric Sciences*.

1.4. Figures
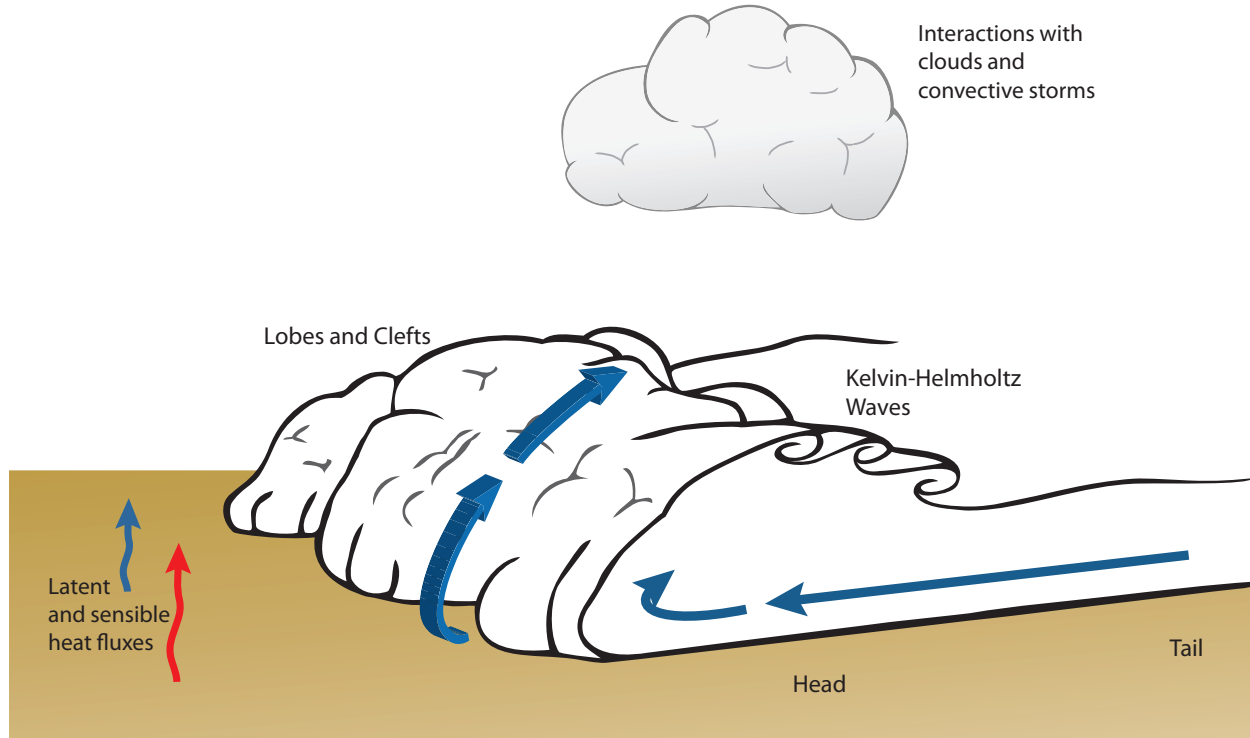
Figure 1.1: Schematic of a density current, its main features and flow regimes, and demonstration of its potential interaction with the surface and with clouds and convective storms. Density current outline adapted from Roberts and Knippertz (2012).

Figure 1.2. Astronaut photograph of intersecting cold pools over the Sahara, taken from the International Space Station. The cold pools are outlined by dust that has been lofted from the surface within the cold pool. Image (NASA photo ID STS049-92-71) courtesy of the Earth Science and Remote Sensing Unit, NASA Johnson Space Center (https://eol.jsc.nasa.gov/).

CHAPTER 2: COLD POOL DISSIPATION

2.1. Introduction

In the Aqua MODIS true-color image over the Sahara desert shown in Figure 2.1, both young and mature cold pools generated by latent cooling associated with precipitation, and their associated outflow boundaries or gust fronts, are apparent from the shallow cloud features that form along their leading edges. Cold pools are common over the Sahara, and they have been shown to play important roles in dust lofting and in the climatology of dry continental regions (e.g. Miller et al. 2008; Garcia-Carreras et al. 2013). The most prominent outflow boundary in Figure 2.1 (indicated by the lower arrow) has spread laterally away from its parent convective storm and is serving as a focal point for new convective development along its northernmost periphery. Although it is widely known that cold pools may initiate convection, several questions arise regarding the details depicted in Figure 2.1. Is the rate of dissipation of the cold pool important in determining the temporal and spatial scales over which cold pools can initiate convection? What processes are responsible for cold pool dissipation? What role do surface sensible heat fluxes, which are large over dry land surfaces such as the Sahara, play in this dissipation? In this study, we explore several aspects pertinent to these broader questions.

Cold pool outflows play important roles in the organization and structure of clouds and cloud systems on all scales, from trade cumulus (e.g. Rauber et al. 2007; Zuidema et al. 2012) and stratocumulus (e.g. Wood et al. 2011; Terai and Wood 2013) to deep convection (e.g. Rotunno et al. 1988; Tompkins 2001, hereafter T01; Khairoutdinov and Randall 2006). As discussed above, cold pools can initiate deep convection, providing a lifting or triggering mechanism on their own or through their interaction with mesoscale boundaries such as sea

breeze (e.g. Kingsmill 1995; Carbone et al. 2000; Grant and van den Heever 2014) and other gust fronts (e.g. Purdom 1982; Droegemeier and Wilhelmson 1985; Wilson and Schreiber 1986).

Idealized modeling simulations have been instrumental in advancing our understanding of varying aspects of cold pool, or density current, characteristics. These modeling studies have examined the turbulent and dynamic characteristics of density currents and the impact of the environment, such as the background stability and shear, on the cold pool dynamics (e.g. Droegemeier and Wilhelmson 1987, hereafter DW87; Xu 1992; Liu and Moncrieff 2000, hereafter LM00; Seigel and van den Heever 2012b, hereafter SvdH12; Bryan and Rotunno 2014; Rooney 2015). Other studies have examined the role of microphysical processes and the subsequent thermodynamic characteristics of cold pools (e.g. Gilmore et al. 2004; van den Heever and Cotton 2004; Dawson et al. 2010). However, relatively few studies have quantitatively investigated the impact of surface energy fluxes on density currents, although both observational and cloud-resolving modeling studies have documented enhancements in surface sensible heat fluxes (SHFs) and latent heat fluxes (LHFs) within cold pools over tropical oceanic regions (Johnson and Nicholls 1983; Young et al. 1995; Jabouille et al. 1996). T01 suggested that the enhanced surface fluxes within the cold pool are important for cold pool dissipation time and convective initiation in tropical oceanic conditions. (The term "cold pool recovery" has been previously used in the literature, including in T01. However, we opt instead to use the term "dissipation" when referring to the weakening of the cold pool itself. The term "recovery" is more appropriate when referring to the evolution of the environment to pre-cold pool conditions.) To date, little to no data exists documenting surface fluxes within cold pools over land.

Surface energy fluxes may impact cold pool dissipation through two mechanisms: by (a) enhancing turbulence and entrainment of environmental air into the cold pool, and (b) directly modifying the cold pool buoyancy. Linden and Simpson (1986) studied mechanism (a) within laboratory experiments by producing bubbles that disrupted the gravity current front. Ross et al. (2004) investigated mechanism (b) utilizing both an integral model and a shallow water model that represented tropical oceanic conditions and neglected entrainment. These studies suggested that both effects could be important. However, an investigation of cold pool sensitivity to surface fluxes at a physical process level using more sophisticated numerical models is still lacking. Additionally, the specific role of SHFs separate from LHFs has not yet been considered, with the possible exception of Linden and Simpson (1986)'s laboratory study. Rooney (2015) recently highlighted the need to investigate the impact of SHFs on cold pool behavior.

The focus of this study is on the particular role of SHFs. We address the hypothesis that cold pool characteristics, including cold pool temperature, vertical velocity above the cold pool head, and propagation speed, are sensitive to SHFs. Classical density current arguments (e.g. Benjamin 1968) suggest that cold pools should dissipate more quickly, and hence have weaker vertical velocities associated with the head circulation and slower propagation speeds, when SHFs are included compared to when they are not. We investigate this hypothesis using an idealized two-dimensional (2-D) numerical modeling framework and an environment representative of daytime, arid, continental conditions (e.g. Figure 2.1); water vapor and hence LHFs are excluded to isolate the impacts of SHFs. Specifically, the role of SHFs in modifying cold pool characteristics is investigated under the following scenarios: (1) bulk fluxes that depend on the wind speed and air-surface temperature difference assuming a fixed surface temperature, and specified constant fluxes; and (2) a range of model resolutions. As will be

17

shown, the bulk fluxes only occur within the cold pool and therefore represent direct

modification of the cold pool buoyancy by SHFs (i.e. mechanism (b) above), while the constant

SHFs do not heat the cold pool *relative* to the environment (the flux is constant across the

domain) and therefore represent the indirect effects of SHFs on turbulent entrainment into the

cold pool (i.e. mechanism (a) above). These two sets of scenarios are also tested in order to

evaluate the extent to which the choices of SHF formulation and model resolution matter for

simulating SHF impacts on cold pools.

2.2. Methods

a. Model description

A 2-D, non-hydrostatic, quasi-compressible model was utilized for these experiments.

The 2-D simulation setup, which has been used in many previous idealized simulations of

density currents, was chosen in order to facilitate the large number of simulations necessary (128

total). A disadvantage of using 2-D is that the turbulent energy cascade is not properly

represented; the implications of this assumption will be discussed in the subsequent sections. As

discussed in section 2.1, water vapor is not included in any of the experiments presented here,

thus facilitating our focus on SHFs. Four prognostic equations for u (zonal wind, m s^{-1}), w

(vertical wind, m s^{-1}), θ' (potential temperature, K, where the prime denotes a perturbation from

the base state which is only a function of height), and π' (perturbation Exner function) are

discretized in flux form on the Arakawa-C grid (Wilhelmson and Chen 1982; DW87). The

equations and numerical methods utilized are the same as in SvdH12.

All simulations presented in this study were 800 km across and 15 km deep and were

integrated for 4000 s. Additionally, a neutrally-stratified, isentropic base state with a constant

potential temperature of 300 K was utilized, and no initial winds were included. This allows for the investigation of cold pool dissipation under varying SHF formulations in simple background environmental conditions without the complicating effects of wind shear and vertically propagating or ducted gravity waves that may interact with the cold pool. The horizontal domain was long enough such that the cold pool was not influenced by the periodic lateral boundary conditions throughout the duration of the simulation, and the high domain top of 15 km has been used in previous studies of density currents propagating in an isentropic atmosphere (LM00). The exclusion of moisture and the utilization of a neutrally stratified atmosphere is representative of a cold pool occurring in the afternoon over a relatively dry land surface when the boundary layer is deep and well-mixed, such as those shown over the Sahara shown in Figure 2.1. By excluding water vapor, we neglect its contribution to buoyancy, which is typically much smaller than that of temperature perturbations. We also neglect any feedbacks to the cold pool by microphysical processes and precipitation formation, thereby simplifying the analysis.

In the highest resolution experiments, the horizontal (Δx) and vertical grid spacings (Δz) were 50 m and 25 m, respectively, and the time step (Δt) was 0.05 s (Table 2.1). The diffusion coefficients for the momentum variables were set to 25 m^2 s^{-1} and 12.5 m^2 s^{-1} in the horizontal and vertical directions, respectively, and were 3$\times$ larger for the scalars (e.g. Deardorff 1972; Klemp and Wilhelmson 1978). These values were determined to be the minimum necessary in order to reduce numerical noise and were held constant in space and time. A cosine-shaped cold bubble, the configuration and amplitude of which was varied in a suite of sensitivity experiments (described in section 2.2b), was placed in the center of the domain at the initial time in order to initialize the density current, which will simply be called the cold pool from here on. The cold bubble was not maintained after the initial time. The grid setup and cold pool initialization were

19

chosen in order to be consistent with previous idealized modeling studies of density currents (e.g.

DW87; Straka et al. 1993; Liu and Moncrieff 1996, LM00; SvdH12).

b. Sensitivity experiments

As described in section 2.1, the influence of both bulk and constant SHF formulations

were tested to elucidate the different mechanisms by which SHFs can contribute to cold pool

dissipation. First, SHFs were excluded; these experiments are named "NoSHF." For the set of

bulk SHF experiments ("BulkSHF"), a bulk formula depending on the surface-air temperature

difference and wind speed was implemented (e.g. Johnson and Nicholls 1983):

$$SHF = c_p \rho C_D U \left(\theta_{sfc} - \theta_{air} \right) \tag{2.1}$$

where U is the magnitude of the horizontal wind speed, θ_{air} the air temperature, and ρ the air

density at the lowest model level above ground. θ_{sfc} is the initial surface temperature, which is set

to the value from the base state θ profile (300 K) and is held constant throughout the simulation

integration. These SHFs are one-way interactive because the land surface temperature does not

respond to the atmosphere; the implications of this assumption are discussed in section 2.3c. c_p is

the heat capacity of dry air at constant pressure. C_D is an aerodynamic bulk transfer coefficient.

In order to represent a fairly smooth land surface such as bare sand or soil, C_D was set to 1.5 x

10^{-3} (Hartmann 1994). Two sets of constant SHF experiments were then performed. For the first

set, named "ConsSHF-300," a single SHF value of 300 W m^{-2} was imposed throughout the

domain for the duration of the simulation. This value is representative of peak daytime SHFs

over a relatively dry land surface according to observations (Mallet et al. 2009; Marsham et al.

2013). In the second set, constant SHF simulations with total energy input comparable to that of

the BulkSHF experiments were performed. For these simulations ("ConsSHF-BulkAvg"), the

constant SHF value was determined by averaging the SHFs from the BulkSHF experiments

spatially over the cold pool and temporally between 600 and 4000 s. The SHF magnitudes

imposed for the various ConsSHF-BulkAvg simulations range from 12.7 to 51.4 W m^{-2} in the

highest resolution simulations (see Figure 2.4c). The four sets of SHF experiments are

summarized in Table 2.1. The SHFs were switched on after 600 s of model simulation time, a

suitable spin-up period as reported in other studies (LM00; SvdH12), so as to ensure that the

changes in cold pool characteristics due to the SHF formulation are not attributable to the

initialization time period before the cold pool is well formed.

The impact of SHFs on cold pool characteristics was also investigated for three different

model resolutions. Δx, Δz, and Δt were progressively doubled from the highest resolution

simulations while holding the domain size fixed. The finest and coarsest *horizontal* grid spacings

used were 50 m and 400 m. The diffusion coefficients were also scaled linearly as the grid

spacings were increased. The reason for this is twofold. First, the Smagorinsky (1963) turbulence

formulation dictates that the diffusion coefficient K is proportional to $(\Delta x \, \Delta z)^{0.5}$. Therefore, if

both Δx and Δz are doubled, K should also be doubled. Second, doubling the diffusion

coefficients along with the time step and grid spacings ensures that the non-dimensional

computational smoothing rates in the horizontal ($K_x \, \Delta t \, / \, \Delta x^2$) and in the vertical ($K_z \, \Delta t \, / \, \Delta z^2$)

remain the same across all of the model resolution experiments (DW87). The various resolution

experiments are referred to by their horizontal grid spacings (Table 2.1).

In order to obtain a large sample size and to ensure that the trends in cold pool

characteristics are robust as the SHF formulation is varied, a variety of different cold bubble

initialization configurations were also tested. Four different spatial bubble configurations were

used, two of which were centered at the surface and hence were dome-shaped (bubbles SfcTall

21

and SfcWide; Table 2.1), and two of which were centered above the surface such that the bottom edge of the cold bubble was at the surface (bubbles ElevTall and ElevWide; Table 2.1). The various cold bubble shapes result in a range of turbulent behavior and therefore a range of cold pool evolutions. Additionally, the initial amplitude of each cold bubble was set to -5 K, -10 K, and -15 K for the 50m and 100m resolution tests. Only the -15 K amplitude was used for the 200m and 400m resolution tests because the cold bubbles in the coarser resolution simulations are much less turbulent, as will be shown in section 2.4. In total, 128 different simulations were performed, which are summarized in Table 2.1.

c. Analysis methods

Since no background winds are included, the cold bubble initialization results in two identical cold pools propagating in opposite directions. Only the rightward-moving cold pool is analyzed. Several different cold pool characteristics of interest are examined in this study. In this section, the various quantities used to analyze these characteristics are defined and explained.

The cold pool leading edge is identified by the largest gradient in θ at the lowest model level above ground. The identified cold pool edge is then used to calculate perturbation quantities (e.g. θ and pressure) in the cold pool relative to the mean environmental quantities ahead of the cold pool, hereafter called "cold pool perturbations." The cold pool perturbations account for the changes that occur in the environment ahead of the cold pool in the ConsSHF simulations; such changes are not represented in perturbation quantities from the time-invariant base state. Therefore, the base state perturbations and cold pool perturbations are identical for the NoSHF and BulkSHF simulations, but they are not the same for the ConsSHF simulations.

22

For each grid column, the top of the cold pool is defined by the highest altitude of the -0.005 m s^{-2} thermal buoyancy contour, where the buoyancy threshold is the same as that used in T01 (different buoyancy thresholds were also tested and they did not change the results), and the thermal buoyancy (Doswell and Markowski 2004) is calculated from the cold pool θ perturbation. The cold pool intensity C, or theoretical cold pool speed, is calculated for each grid column using the following equation (e.g. Benjamin 1968; Rotunno et al. 1988):

$$C^2 = 2 \int_0^H -g \frac{\theta'}{\theta_{env}} dz \qquad (2.2)$$

where H is the height of the cold pool, g is the gravitational acceleration, and θ' is the cold pool perturbation relative to the mean θ ahead of the cold pool, θ_{env}. Non-cold pool air is simply all air located above the identified cold pool top. Maximum vertical velocity is found within non-cold pool air, and within 10 km of the cold pool's leading edge, in order to quantify the strength of the cold pool-driven ascent within environmental air that would be most favorable for convective initiation. An average cold pool propagation speed toward the end of the simulations is calculated from the distance traveled by the cold pool's leading edge over the last 1000 s. All other temporally averaged quantities exclude the first 1000 s to avoid the cold pool spin up period and the influence of the initial conditions.

2.3. Results from the 50m simulations

a. Characteristics of the NoSHF-50m experiments

Figure 2.2 demonstrates the main features of one of the cold pools in the highest resolution experiments. The cold pool has taken on a classic shape with a shallow tail region and a 2-km-deep head region. The strongest θ perturbations are located at the surface throughout ~5 km behind the leading edge of the cold pool (Figure 2.2c), and the strongest surface winds are

23

located behind the strongest θ perturbations (Figure 2.2a). A broad and deep region of ascent is located above the cold pool head (Figure 2.2b), the magnitude of which is in keeping with previously observed gust front vertical velocity measurements of nearly 10 m s^{-1} (Martner 1997). Kelvin-Helmholtz (KH) waves are clearly evident in the θ and wind fields and are a result of shearing instability associated with the circulation induced by the cold pool. The KH waves are associated with substantial fluctuations in the wind field within the cold pool itself and low-pressure perturbations at their center where the circulation is strongest (Figure 2.2d). Such KH waves have been noted in numerous other numerical simulations of density currents (DW87; Straka et al. 1993; Xu et al. 1996; Xue 2002), as well as in observations of gust fronts, sea breezes, and bow echoes (Mueller and Carbone 1987; Ralph et al. 1993; Lapworth 2000; Plant and Keith 2007; Wakimoto et al. 2006, their Figure 16).

The evolution of several averaged cold pool characteristics in the NoSHF-50m simulations are shown in Figure 2.3 for each of the three initial cold bubble amplitudes (-15 K, -10 K, and -5 K), and the average cold pool propagation speeds over the last 1000 s of the simulations are listed in the second column of Table 2.2. Three different measures of cold pool dissipation are shown for the following reasons. First, the cold pool intensity (Figure 2.3a), calculated from the formula given in Equation 2.2, is arguably the best measure of the overall strength of the cold pool, since it accounts for the integrated buoyancy over the entire depth of the cold pool. It is most closely related to the surface pressure perturbation in the cold pool head and therefore to the cold pool propagation speed. In fact, the actual cold pool speeds calculated over the last 1000 s (Table 2.2) match the theoretical cold pool speeds shown in Figure 2.3a quite well, being only ~15% smaller. The cold pool intensity can be calculated in observational studies if high spatial resolution rawinsonde data are available from field campaign measurements, as

24

was done for midlatitude squall line cold pools in Bryan et al. (2005) and Bryan and Parker (2010). However, in most observational studies, buoyancy calculations throughout the cold pool depth are not possible due to the limited availability of rawinsonde data. In these cases, the surface temperature perturbations in the cold pool, which are readily measureable by surface observation station networks, are sometimes used as a proxy for the strength of the cold pool, such as in Engerer et al. (2008). Therefore, the minimum θ perturbation is also shown here as another measure of the strength of the cold pool (Figure 2.3b). Third, maximum vertical velocity in non-cold pool air (Figure 2.3c) is a good indicator of the potential for the cold pool to initiate new convection through mechanical lifting.

Figure 2.3 demonstrates that, even in the absence of SHFs, the cold pools slowly weaken or dissipate with time by all three measures of cold pool strength. For instance, the average cold pool intensities decrease by 20-25% between 1000 and 4000 s (Figure 2.3a). The cold pools without SHFs dissipate for two reasons. First, the cold air source is not maintained. Second, the cold pools are turbulent (Figure 2.2), and the KH waves help to entrain the warmer environmental air into the cold pool. The cold pools dissipate at relatively steady rates from ~1500 s onward. As expected, the initially colder cold pools are stronger than the initially warmer cold pools throughout the simulation duration, and these colder cold pools also have 50% larger propagation speeds than the warmer cold pools (Table 2.2). Although the cold pools all dissipate at approximately the same rate in terms of their intensity (Figure 2.3a) and maximum vertical velocity (Figure 2.3c), the minimum θ perturbations warm faster in the initially colder cold pools than in the initially warmer cold pools (Figure 2.3b). The minimum θ perturbations, which are found at the surface, dissipate more quickly in the initially colder cold

25

pools because the cold pool's internal circulation – which is stronger in the initially colder cold pools – acts to homogenize the vertical temperature distribution more rapidly through mixing.

b. SHF modification of cold pool characteristics

Before examining how SHFs influence the cold pools, the spatial and temporal bulk SHF patterns are first illustrated for one of the 50m simulations (Figure 2.4a-b). In accordance with Equation 2.1, SHFs are largest where the cold pool is coldest, directly behind the cold pool's leading edge, and where the wind speed is highest, 5-10 km behind the cold pool's leading edge. The oscillations in wind speed and SHFs that occur 5-10 km behind the leading edge of the cold pool from 1500 s onward are associated with the KH waves that cascade into the tail region of the cold pool (Figure 2.2). The impact of KH waves on near-surface fields behind the cold pool head has also been noted in observations (Mueller and Carbone 1987; Ralph et al. 1993). Although the range in SHFs is large among the 12 BulkSHF-50m experiments during the first half of the simulations, the SHFs toward the end of the simulations are small in magnitude for all of the cold bubble experiments as the cold pool dissipates, as shown by the time series of BulkSHFs averaged over the cold pool head (Figure 2.4c). In other words, the SHFs in the initially stronger cold pools become similar to those in the initially weaker cold pools because the near-surface temperatures warm faster in the initially stronger cold pools, as shown in Figure 2.3b.

Potential temperature perturbations *relative to the time-invariant base state* for three of the SHF experiments at the end of one example set of cold pool simulations are shown in Figure 2.5. Several qualitative differences among the SHF experiments are evident that are also representative of the other simulation sets. Intuitively, the absolute cold pool temperatures are

warmer with bulk and constant surface fluxes than without any surface fluxes. The absolute temperatures have warmed significantly more in the ConstSHF-300 simulation than in the BulkSHF simulation because the specified 300 W m^{-2} SHF is greater in magnitude than the bulk SHFs throughout most of the simulation (Figure 2.4c). The cold pool and KH wave structure also appear different among the three simulations. Finally, the air ahead of the cold pool in the ConsSHF-300 simulation has become statically unstable as a result of the uniform surface heating and is evolving into individual convective plumes (Figure 2.5c). In other words, turbulent kinetic energy (TKE) is generated in the environment ahead of the cold pool. Some of this heated air is then lifted along the cold pool head, as is evident in Figure 2.5c.

The impacts of bulk and constant SHFs on the average cold pool intensity, minimum cold pool θ perturbation, and maximum vertical velocity in the 50m experiments are quantified in Figure 2.6 (blue, red, and green lines; the 100m results will be discussed in section 2.4). The shading indicates the variability in the percent differences of these quantities from the NoSHF-50m simulations. This variability arises due to the different initial cold bubble configurations (SfcTall, SfcWide, ElevTall, ElevWide) and amplitudes (-15 K, -10 K, and -5 K) and hence the range in turbulent behaviors among the simulations. The average percent differences in cold pool propagation speed from the NoSHF simulations are also listed in Table 2.2. It is clear from Figure 2.6 and Table 2.2 that the way SHFs are represented has a significant impact on the *manner* in which the SHFs modify the cold pool characteristics. Specifically, while both bulk and constant SHFs weaken the cold pool intensity and hasten its dissipation relative to the NoSHF cases, the cold pool intensity is reduced by the largest percentage in the ConsSHF-300 cases (up to 10-15% weaker), by up to 5% in the BulkSHF cases, and by only a few percent in the ConsSHF-BulkAvg cases at the end of the simulations (Figure 2.6a). The cold pool

27

propagation speeds are also reduced the most in the ConsSHF-300 simulations (Table 2.2) in keeping with the less negatively buoyant cold pools. However, if cold pool dissipation is measured in terms of the minimum cold pool θ perturbation (recall that the cold pool perturbations are calculated relative to the environment ahead of the cold pool), the ConsSHF-300 minimum θ perturbations are 10-20% *colder (i.e. stronger)*, while the BulkSHF minimum θ perturbations are 10-20% *warmer (i.e. weaker)*, relative to the NoSHF cases (Figure 2.6b), which is opposite to the cold pool intensity trends. Finally, while bulk SHFs and the smaller magnitude constant SHFs make very little difference in the maximum vertical velocities, the 300 W m^{-2} prescribed SHFs substantially increase the maximum vertical velocities by up to 50-100% (Figure 2.6c).

Exactly how then do SHFs modify the cold pool characteristics and influence cold pool dissipation, and why are the impacts of bulk versus constant SHFs on these characteristics so different? To answer these questions, temporally averaged cold pool properties for one set of SHF experiments are shown in Figure 2.7 and Figure 2.8. Only one simulation set is shown for clarity. This simulation set is representative of the other simulation sets. The trends in cold pool characteristics for the bulk SHFs are discussed first, and then the trends for the constant SHF cases are explained. In the following discussion, recall that "cold pool perturbation" quantities are calculated relative to the environment ahead of the cold pool, which are not necessarily the same as the perturbations relative to the time-invariant model base state shown in Figure 2.5 (see section 2.2c).

In the bulk SHF cases, the near-surface cold pool θ perturbations within 10 km behind the cold pool's leading edge are 10-20% warmer in BulkSHF than in NoSHF (Figure 2.7a) where the bulk SHFs are large (Figure 2.4b). However, in the tail region where the bulk SHFs are small,

the θ perturbations are nearly the same as NoSHF. The average cold pool θ perturbations are also warmer throughout the lowest 2 km of the cold pool head region and are warmest at the surface by nearly 15% in BulkSHF, as shown by the θ perturbation profiles in Figure 2.8. The high-pressure perturbations behind the leading edge of the cold pool and the integrated buoyancy are therefore also weaker (Figure 2.7b-c), and the propagation speed is slower in the BulkSHF cases (Table 2.2). (Note that the low-pressure perturbations from 5-10 km behind the cold pool edge are related to the KH wave circulations and hence are non-hydrostatic; see Figure 2.2.) However, the pressure and intensity changes are only 5% or less, and the vertical velocity in non-cold pool air is nearly the same (Figure 2.7d). Thus, while the impact of bulk SHFs is significant on the near-surface temperature field, their impacts on the broad cold pool characteristics are not as large.

In the ConsSHF-300 case, Figure 2.7a demonstrates that the near-surface cold pool θ perturbations are, counter-intuitively, colder than in NoSHF by up to 10% in the head region and up to 100% in the tail region, as first shown in Figure 2.6b. While the cold pool intensity in the tail region is also stronger by about 10% in ConsSHF-300 (Figure 2.7c), in agreement with the temperature perturbation trends there, the intensity is weaker in the head region of the cold pool, which is opposite to the near-surface temperature perturbation trends in the cold pool head. Bryan et al. (2005) have also shown that cold pool intensity is not always well correlated with the surface temperature perturbations due to variations in stratification within the environment and the cold pool, and that caution must be exercised when using surface temperature perturbations to characterize the strength of cold pools. As expected, the cold pool pressure perturbation trends correspond to the intensity trends (Figure 2.7b) because pressure perturbations are hydrostatically related to the integrated buoyancy. The weaker pressure

perturbations near the cold pool's leading edge result in slower propagation speeds (Table 2.2). The ConsSHF-BulkAvg simulations exhibit the same trends as the ConsSHF-300 cases but with much smaller magnitudes.

The reason for the opposite trend in the near-surface cold pool θ perturbation and the cold pool intensity in the ConsSHF cases is elucidated by the θ perturbation profiles (Figure 2.8) and the recollection that cold pool perturbations are calculated relative to the environment ahead of the advancing cold pool. Although *near-surface* cold pool θ perturbations in ConsSHF-300 are colder than those in NoSHF by nearly 15%, the θ perturbations above 0.3 km are warmer, by greater than 25% above 1.7 km (Figure 2.8b). (Again, the ConsSHF-BulkAvg results have the same trends as ConsSHF-300 but with smaller magnitudes.) This result can be understood by keeping in mind that both the cold pool and the environment ahead of the cold pool are heated at equal rates in the ConsSHF cases. The heating within the cold pool is vertically mixed and communicated throughout the cold pool due to the cold pool's internal circulations. Therefore, in the ConsSHF simulations, the *near-surface* temperatures increase more quickly in the environment than they do in the cold pool. This results in a stronger near-surface temperature difference between the cold pool and the environment in the two ConsSHF cases compared with NoSHF. Conversely, the temperature difference between the cold pool and the environment is weaker aloft where the environmental air is not directly heated by the surface. Also, as noted in the discussion of Figure 2.5, TKE is generated in the environment ahead of the cold pool in the ConsSHF simulations as the air becomes statically unstable near the surface, and this positively buoyant air is more easily lifted by the cold pool head. Aside from increasing the vertical velocities in non-cold pool air by several m s^{-1} (Figure 2.7d and Figure 2.6c), Figure 2.5 demonstrates that some of this heated environmental air is entrained into the cold pool head by

the turbulent KH waves. This process also contributes to the warmer θ perturbations aloft in the ConsSHF cold pools through sensible heat flux convergence. Such heating by breaking KH waves was also shown to contribute significantly to the turbulent erosion of valley-trapped cold-air pools within high-resolution 3-D simulations by Lareau and Horel (2015).

To summarize the ConsSHF results, when prescribed SHFs are included, the cold pool intensity is reduced, but near-surface cold pool temperature perturbations are enhanced, compared to when SHFs are excluded. These trends result from the heating of the environmental near-surface air ahead of the cold pool and subsequent entrainment of this heated air into the cold pool. Overall, SHFs can exert a significant influence on various cold pool characteristics, but the *manner* in which they do so strongly depends on the SHF formulation, the SHF magnitude, and the detailed flow structure within the cold pool.

c. Discussion

We ask two final questions based on these results: (1) what are the most important physical mechanisms for cold pool dissipation, and (2) are proper representations of SHFs important to accurately capture cold pool dissipation, lifetimes, and the potential ability of the cold pool to initiate convection in cloud-resolving models? It should be noted that, with respect to question (1), the 2-D nature of our simulations makes it inappropriate to quantify the cold pool dissipation rates directly (e.g. Tompkins 2000). Rather, our goal is to compare the relative importance of the mechanisms that contribute to cold pool dissipation.

The ConsSHF experiments allow us to specifically explore how SHFs impact turbulence and entrainment into the cold pool, such as was done in Linden and Simpson (1986), because the prescribed SHFs are the same everywhere and hence the cold pool is not heated *relative* to the

environment (i.e. any more or less than the environment). Conversely, the BulkSHF experiments represent how SHFs directly modify the cold pool buoyancy through surface heating, as was investigated by Ross et al. (2004), since these SHFs *only* occur within the cold pool (i.e. the environment ahead of the cold pool remains undisturbed and hence no bulk SHFs occur there). As discussed in section 2.3a, the cold pool intensity weakens by 20-25% over 3000 s irrespective of whether SHFs are included, but bulk SHFs decrease cold pool intensities by at most an additional 5% (Figure 2.6a). On the other hand, for realistic peak daytime SHFs of 300 W m^{-2}, the constant SHFs decrease cold pool intensities by an additional 10-15% relative to the NoSHF cases (Figure 2.6a). Therefore, comparing the dissipation rates in the NoSHF cases to the additional enhancements in the dissipation rates for the various SHF simulations, we conclude that *entrainment of environmental air into the cold pool is an important mechanism for cold pool dissipation.* Furthermore, for ambient SHFs representative of daytime continental values over a relatively dry land surface type, *the impact of SHFs on near-surface environmental static stability, and hence entrainment into the cold pool, plays a more significant role in cold pool evolution than does direct modification of the cold pool buoyancy by SHFs*. This statement is in keeping with the findings of Linden and Simpson (1986) that SHF impacts on turbulent entrainment into a laboratory density current were significant. It is contrary to the conjecture by T01, and the findings of Ross et al. (2004), that direct modification of cold pool buoyancy by surface fluxes is important, although those studies investigated weak tropical oceanic cold pools for which ambient SHF magnitudes are much smaller than the 300 W m^{-2} value tested here, and latent heat fluxes – which also modify the cold pool buoyancy – are substantial. In fact, in our simulations, the impact of bulk SHFs is greater than or equal to that of constant SHFs when the total energy input is comparable (Figure 2.6 and Table 2.2; compare BulkSHF to ConsSHF-

BulkAvg), even though neither has a large effect on these cold pools. The cold pools simulated in this study are deeper, colder, more intense, and likely more turbulent, than tropical oceanic cold pools. These considerations suggest that direct modification of the cold pool buoyancy by SHFs may play a larger relative role than demonstrated here over tropical oceanic regions, where cold pools are smaller, weaker, and less turbulent, and where ambient SHFs are weak.

Finally, it can be argued that both types of SHFs enhance the potential of the cold pool to initiate new convection. In the constant SHF cases, convective initiation is more likely given the increased vertical velocities. In the BulkSHF cases, the maximum vertical velocities are the same compared to the NoSHF cases (Figure 2.6c), but the cold pool θ perturbations are warmer by up to 20% (Figure 2.6b). Since some parcels entering a convective updraft are likely to originate from within the cold pool (e.g. Droegemeier and Wilhelmson 1985; Torri et al. 2015), it can be argued that the less-negatively-buoyant cold pools – i.e. those subjected to bulk surface fluxes – are more likely to initiate convection than the cold pools unmodified by SHFs, *all else being equal*. Therefore, the inclusion of SHFs and their impacts on both the near-surface stability and the cold pool buoyancy may impact the timing of cold-pool-induced convective initiation.

Several assumptions used in our experiments will influence how these results translate to less idealized scenarios. First, the BulkSHF simulations presented here used a fixed surface temperature approximation, meaning that the bulk SHFs are only one-way interactive. A fully interactive land surface model will include variable land surface temperatures. It is possible that the cooling of the land surface by the cold pool itself would be great enough to suppress SHFs behind the cold pool's leading edge, an effect that was suggested in simulations of convection near Darwin, Australia by Del Genio et al. (2012). If we were to account for the land surface cooling due to the presence of the cold pool, the magnitude of the SHF contribution to cold pool

33

dissipation by direct heating would be even smaller than suggested here, reinforcing our conclusion that SHFs primarily modify cold pool dissipation through their indirect influence on turbulent entrainment rates in continental scenarios. Moreover, effects such as cloud cover or soil moisture heterogeneity will alter the net surface energy balance and change the SHFs ahead of the cold pool. This, in turn, will modify the magnitude of the SHF impacts on turbulent entrainment rates and sensible heat flux convergence into the cold pool. These effects will not be captured if specified surface fluxes are utilized. Prescribed surface fluxes are still common choices in modeling studies for various reasons. For instance, they are less computationally expensive than fully interactive land surface models, and prescribed fluxes are easy to constrain to observations – such as measured surface fluxes from field campaign data – or to impose as idealized, diurnally varying fluxes (e.g. Khairoutdinov and Randall 2006; Böing et al. 2012; Schlemmer and Hohenegger 2014). However, our results demonstrating the importance of turbulent entrainment into the cold pool suggest that cloud-resolving model simulations utilizing surface fluxes determined by an interactive land surface model will be able to simulate cold pool characteristics and dissipation rates more accurately. This conclusion follows from the fact that the turbulent entrainment rates are dependent on the ambient SHF magnitudes, which can be highly variable.

Second, the 2-D diagnosis of entrainment rates will not be directly extendable to 3-D because the nature of the turbulent energy cascade is different in two- and three-dimensions (e.g. Cantero et al. 2008; Bryan and Rotunno 2014). However, since KH waves have been noted in numerous observations of cold pools (Mueller and Carbone 1987; Ralph et al. 1993; Wakimoto et al. 2006) and in three-dimensional simulations (Cantero et al. 2008), we suspect that the qualitative results presented in this study can be extended to three-dimensions. Additionally,

since the breakdown of KH vortices into small-scale turbulence is better represented in three-dimensional simulations, the impacts of SHFs on entrainment into the cold pool may be even greater than demonstrated here.

2.4. Impact of constant and bulk SHFs for coarser resolutions

In this section, results from the coarser resolution experiment sets (Table 2.1) are investigated in order to assess whether the processes by which bulk and constant SHFs influence cold pool characteristics are also captured with coarser model resolutions. It is worth noting that the coarsest horizontal grid spacing of 400 m used in these tests is still considered to be very high resolution by today's standards for typical regional cloud-resolving modeling simulations.

Cross sections of θ perturbations at 3000 s for four NoSHF simulations with varying resolutions but identical initial cold bubble configurations are shown in Figure 2.9. It is evident from this figure that the cold pool minimum θ perturbations dissipate more quickly as the model resolution is coarsened; this is true of their intensity dissipation as well. They also have weaker vertical velocities by up to 30% (not shown) and slower propagation speeds. For instance, the average propagation speed among the four -15 K cold bubble simulations decreases by nearly 20% between the 50m and 400m experiment sets. Additionally, the coarser resolution simulations are less able to capture the detailed flow structure within and around the cold pool. The positively-buoyant plumes of air that develop ahead of the cold pool in the ConsSHF-50m simulations (Figure 2.5c) are not represented in any of the coarser resolution experiments (not shown). The KH waves, and therefore the internal flow structure within the cold pool, are less well resolved in the 100m experiments than in the 50m experiments, although the KH waves are clearly still present (Figure 2.9b). However, the KH waves are only marginally resolved at times

in the 200m experiments being barely evident in Figure 2.9c, and they are completely absent in the 400m experiments (Figure 2.9d), in agreement with many previous studies (e.g. DW87; Straka et al. 1993; Bryan et al. 2003). The 400m experiments only capture the basic features of the cold pool structure, including the shallow tail region and the location of the coldest θ perturbations associated with the deeper head region.

Because even the 100m simulations do not resolve the buoyant plumes – and hence the generation of ambient TKE – in the ConsSHF-300 experiments and do not capture the fine-scale details of the turbulent KH waves as well as in the 50m simulations, there is less variability in the percent differences between the SHF and NoSHF cold pool characteristics in the 100m experiments compared to the 50m experiments, as indicated by the smaller spread in the 25th and 75th percentiles shown in Figure 2.6. Additionally, Figure 2.6 suggests that the magnitude of these percent differences generally decreases as the grid resolution is coarsened from the 50m to the 100m tests, which indicates that the cold pools are less sensitive to SHFs at coarser resolutions. Figure 2.10, which shows the trends in the same percent difference quantities that are shown in Figure 2.6 but which are now averaged over the four -15 K initial bubble simulations for the 100m, 200m, and 400m resolution tests, reinforces this conclusion. For instance, the magnitudes of the percent decreases in the cold pool intensity are up to twice as large in the 100m tests compared to the 400m tests (Figure 2.10a). Moreover, the ConsSHF-300-200m, ConsSHF-300-400m, and ConsSHF-BulkAvg-400m simulation sets actually have warmer, instead of colder, minimum θ perturbations relative to their respective NoSHF simulations (Figure 2.10b). This error is particularly severe in the ConsSHF-300-400m simulations.

The cold pools are less sensitive to both bulk and constant SHFs as the resolution is coarsened for several reasons. First, although the computational smoothing rate is the same across the resolution experiments (see section 2.2b), it is applied over a larger area as the grid spacing is increased. This means that the temperature perturbations and winds are ultimately smoothed out as the resolution is coarsened. As a result, the magnitude of the temperature perturbations and winds are weaker, and hence the bulk SHF magnitudes are smaller, implying that their impacts on the cold pools are reduced. In the constant SHF cases, because the generation of positively-buoyant plumes of air and TKE in the ambient environment are not captured and turbulent KH wave formation is not resolved, resulting sensible heat flux convergence into the cold pool is not adequately represented in the 200m and 400m results. Finally, due to the coarser vertical grid spacing, the heating ahead of the cold pool is distributed over a greater depth. Thus, the coarsest resolutions incorrectly simulate a decrease, rather than an increase, in the near-surface cold pool temperature perturbation for the constant SHF cases.

From these resolution tests, we make the following recommendations. First, caution should be exercised when interpreting quantitative cold pool statistics obtained from simulations using horizontal (vertical) grid spacings coarser than 100 m (50 m), since cold pool characteristics like minimum θ perturbations can vary by more than a factor of 2 from their higher resolution counterparts. Second, where feasible, cloud resolving modeling simulation results with 100 m or better grid spacings should be used to build cold pool parameterization schemes, particularly when incorporating the impacts of surface fluxes on cold pools. At coarser grid spacings, the cold pools are less sensitive to surface fluxes by up to a factor of 2 and some of the trends in cold pool characteristics *may even reverse*. Finally, future detailed process studies of cold pools and their interaction with deep convection should use horizontal and

vertical grid spacings of 100 m and 50 m, respectively (or finer if possible), in order to adequately capture details of the cold pool evolution and its interaction with the environment. Although these recommendations have been made based on 2-D simulations and could vary with different subgrid diffusion parameterizations, they are in keeping with prior grid spacing recommendations to adequately simulate the largest turbulent eddies and their impacts on deep convection, based on 3-D simulations (Bryan et al. 2003). In fact, Bryan et al. suggested that even 125 m grid spacings might not be fine enough to adequately simulate the turbulent properties of cold pools in 3-D (see their Figure 11).

2.5. Conclusions

The goals of this study have been to elucidate the mechanisms by which cold pools dissipate, the role of surface sensible heat fluxes (SHFs) on the dissipation rates, and the implications of this dissipation for convective initiation. These goals were accomplished with idealized, 2-D simulations of cold pools in which the effects of water vapor were excluded to isolate the SHFs from LHFs. The environment was representative of cold pools that occur during the daytime over relatively dry continental surfaces. 128 different simulations were performed. Three SHF formulations were tested: no SHFs, bulk SHFs that depend on the temperature and wind speed assuming a fixed surface temperature, and constant SHFs of (a) 300 W m^{-2} based on peak daytime SHFs from observations; and (b) average SHF values from the bulk SHF simulations. The constant SHF cases represented the impacts of SHFs on turbulent entrainment into the cold pool because the SHF was the same everywhere, and therefore the cold pool was not heated *relative* to the environment (i.e. the cold pool was not heated more or less than the environment outside of the cold pool). The bulk SHF experiments only included SHFs within the

cold pool and therefore investigated how SHFs directly modify cold pool buoyancy through surface heating. Additionally, the relationships between cold pool characteristics and SHF formulations were investigated for different model resolutions with horizontal (vertical) grid spacings from 50 m (25 m) through to 400 m (200 m).

In the highest resolution simulations, it was demonstrated that the inclusion of SHFs influence cold pool characteristics and cold pool dissipation rates, but the *manner* in which they do so strongly depends on the SHF formulation. Both bulk and constant SHFs hastened cold pool dissipation rates when assessed using the cold pool integrated buoyancy and propagation speed, but the most significant changes in cold pool dissipation rates occurred for the constant 300 W m^{-2} SHF value. The bulk SHFs and the smaller magnitude constant SHFs computed from the averaged bulk SHFs had only slight impacts on cold pool dissipation. Additionally, while bulk SHFs reduced the *near-surface* cold pool temperature perturbations, constant SHFs enhanced the near-surface temperature differences between the cold pool and the environment because the constant SHFs heated the near-surface environmental air ahead of the cold pool more quickly than the cold pool air. These results suggest that the indirect impact of SHFs on entrainment into the cold pool is more important for cold pool dissipation than the direct modification of the cold pool buoyancy by SHFs for the SHF magnitudes and types of cold pools studied here. It was concluded that including the effects of sensible heating on cold pool dissipation may have implications for the timing of convective initiation through the SHF impacts on the near-surface environmental stability and on the cold pool's buoyancy. Finally, given the demonstrated importance of SHF impacts on turbulent entrainment into the cold pool, it was suggested that cloud-resolving model simulations will more accurately represent cold pool characteristics and their dissipation rates when using an interactive land surface model, which can capture variations

in ambient SHFs and hence turbulent entrainment rates into the cold pool, compared with using prescribed surface fluxes.

The grid resolution experiments demonstrated that the detailed cold pool structure, flow, and turbulent development are not well captured as the grid spacings are systematically increased. As such, the simulated cold pools are less sensitive to SHFs under coarser resolutions. Moreover, the simulations with horizontal (vertical) grid spacings of 200 m (100 m) or greater not only poorly, but sometimes wrongly, represent the impacts of SHFs on the cold pool characteristics. It is recommended that future process studies of cold pools, especially those investigating the importance of surface fluxes, utilize horizontal (vertical) grid spacings of 100 m (50 m) or finer if we are to avoid such errors, and that cold pool parameterization schemes should be based on cloud-resolving model simulations with grid spacings of 100 m or better where feasible.

Future work should investigate the sensitivity of cold pool characteristics to surface fluxes under different stability regimes and wind shear profiles, which are known to have substantial influences on cold pool structure and propagation. The importance of environmental stability is highlighted in our constant SHF experiments, since the cold pool lifting of the near-surface statically unstable air produced substantially stronger vertical velocities near the cold pool head and enhanced warming of the cold pool air above the surface. The results presented here should be replicated in three-dimensional simulations as well. In addition to a more quantitative analysis of the cold pool dissipation rates themselves, lobe and cleft instabilities (e.g. Simpson 1972) are possible in 3-D simulations and may contribute significantly to entrainment rates. Finally, observational studies of cold pools and surface fluxes would also be useful to assess the conclusions presented here. The opposite trends in near-surface cold pool temperatures

and integrated cold pool buoyancy demonstrated in the constant SHF experiments highlight the

critical need for more detailed observations of the full cold pool vertical structure.

2.6. Tables and figures

Table 2.1: Experiment names and descriptions

SHF Experiments	
Name	Description
NoSHF	SHFs excluded
BulkSHF	SHFs calculated using a bulk formula, assuming fixed surface temperature
ConsSHF-300	SHF of 300 W m^{-2} imposed uniformly throughout the domain
ConsSHF-BulkAvg	SHF value, calculated by averaging the SHFs over the cold pool from the corresponding BulkSHF simulation, imposed uniformly throughout the domain

Resolution Experiments			
	Grid Setup		
Name	Δx, Δz	nx, nz	Δt
50m	50 m, 25 m	16000, 600	0.05 s
100m	100 m, 50 m	8000, 300	0.1 s
200m	200 m, 100 m	4000, 150	0.2 s
400m	400 m, 200 m	2000, 75	0.4 s

Cold Bubble Initialization Experiments			
	Bubble Characteristics		
Name	Amplitude[5]	radx, radz[6]	zcent[7]
SfcTall-15	-15 K	4 km, 6 km	0 km
SfcTall-10	-10 K		
SfcTall-5	-5 K		
SfcWide-15	-15 K	6 km, 4 km	0 km
SfcWide-10	-10 K		
SfcWide-5	-5 K		
ElevTall-15	-15 K	4 km, 3 km	3 km
ElevTall-10	-10 K		
ElevTall-5	-5 K		
ElevWide-15	-15 K	6 km, 2 km	2 km
ElevWide-10	-10 K		
ElevWide-5	-5 K		

---

[5] -10 K and -5 K bubble amplitude simulations were only performed for 50m and 100m resolution experiment sets

[6] Horizontal and vertical radii of initial cold bubble

[7] Altitude of the center of the initial cold bubble

Table 2.2: Average cold pool propagation speed[8] in the 50m experiments

Initial cold bubble amplitude (K)	NoSHF (m s^{-1})	BulkSHF difference (%)[9]	ConsSHF-300 difference (%)	ConsSHF-BulkAvg difference (%)
-15	12.23	-4.1	-7.2	-4.2
-10	10.53	-1.9	-5.6	-0.6
-5	8.13	-2.0	-8.8	-0.5

[8] Cold pool propagation speed over the last 1000 s for each individual simulation was determined by tracking the cold pool's leading edge as described in section 2.2c. The propagation speeds were then averaged over the four initial cold bubble configurations (SfcTall, SfcWide, ElevTall, and ElevWide) for each of the three initial cold bubble amplitudes.

[9] Percent differences in average cold pool propagation speed from NoSHF
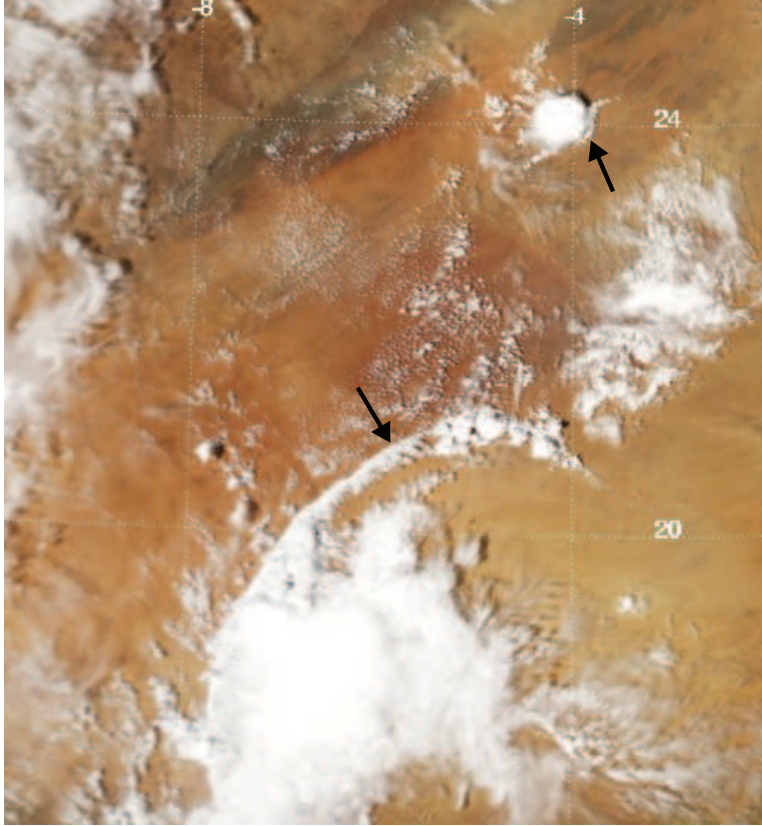
Figure 2.1: Aqua MODIS true-color scene over the northwestern Sahara desert at 1330 UTC 4 September 2010. Outflow boundaries are denoted by arrows.
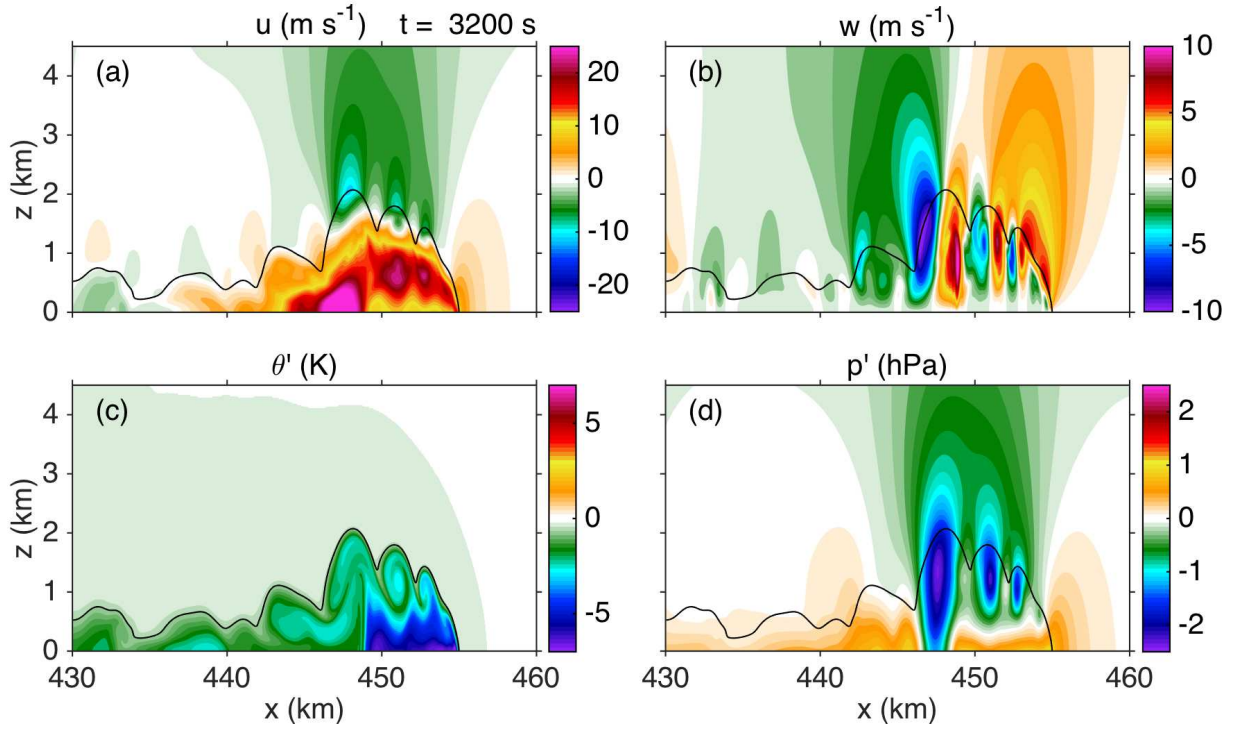
Figure 2.2: Cross sections of (a) zonal wind, (b) vertical velocity, (c) perturbation θ, and (d) perturbation pressure for simulation NoSHF-50m-SfcTall-15 at 3200 s. The -0.5 K perturbation θ is contoured in black for reference.
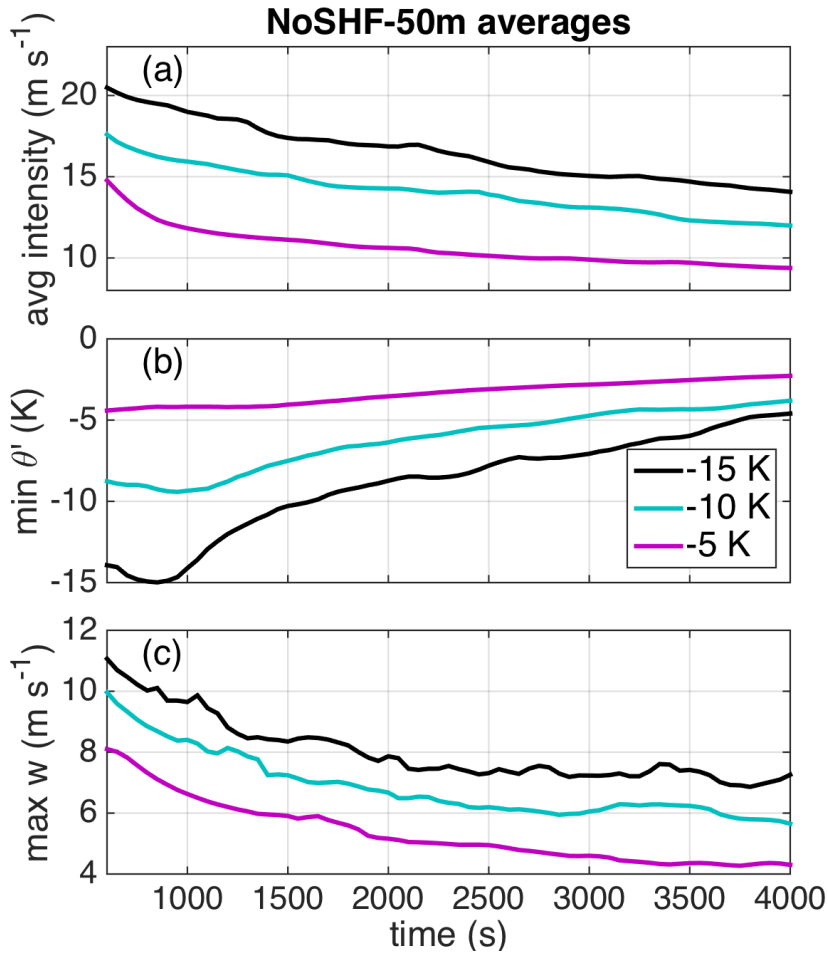
Figure 2.3: Time series of (a) cold pool intensity, (b) minimum cold pool θ perturbation, and (c) maximum vertical velocity in non-cold pool air for the NoSHF-50m simulations. Results are averaged over the four initial cold bubble configurations (SfcTall, SfcWide, ElevTall, and ElevWide) for each of the three initial cold bubble amplitudes as indicated in the legend. The cold pool leading edge, cold pool intensity, and non-cold pool air are determined as described in section 2.2c. The cold pool intensity is averaged over 10 km behind the cold pool's leading edge in order to average over a consistent distance in all simulations and to incorporate the entire head region in the average.
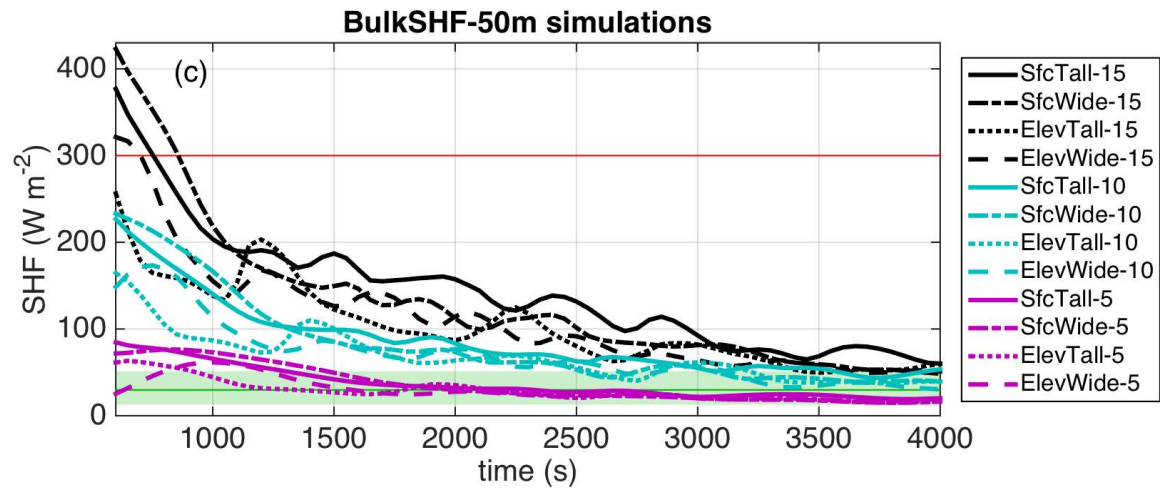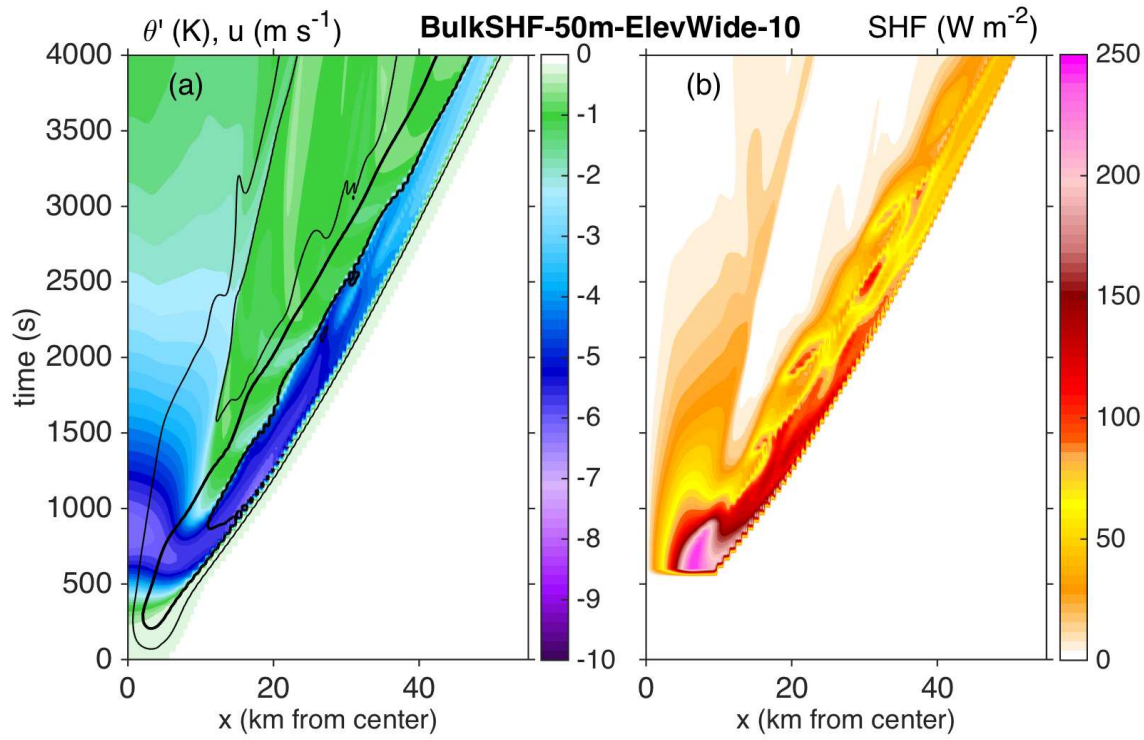
Figure 2.4: Hovmöller plot of (a) perturbation θ (shaded) and zonal wind (5 m s⁻¹ thin and 15 m s⁻¹ thick black contours) at the lowest model level above ground (12.5 m), and (b) surface sensible heat flux for simulation BulkSHF-50m-ElevWide-10. Note that the step-like patterns, such as near the cold pool's leading edge, are a result of the temporal output resolution of 50 s. (c) Time series of sensible heat flux averaged over 10 km behind the cold pool leading edge for each of the 12 BulkSHF-50m simulations as indicated in the legend. The red line represents the SHF value for the ConsSHF-300 simulations, while the green line (shading) represents the median (minimum and maximum) SHF values used in the 12 ConsSHF-BulkAvg-50m simulations.
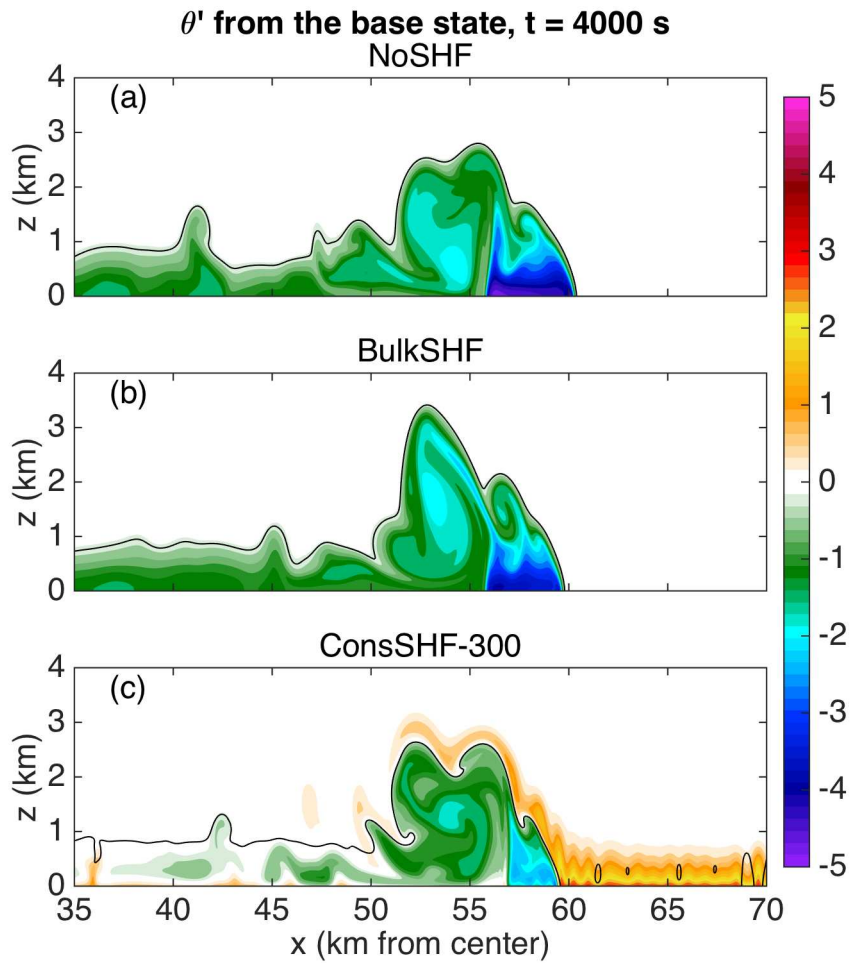
47

θ' **from the base state, t = 4000 s**

Figure 2.5: Cross sections of perturbation θ relative to the base state (K) at 4000 s for the (a) NoSHF, (b) BulkSHF, and (c) ConsSHF-300 experiments in the 50m-ElevWide-15 simulation set. The -0.005 m s^{-2} buoyancy value is contoured in black.
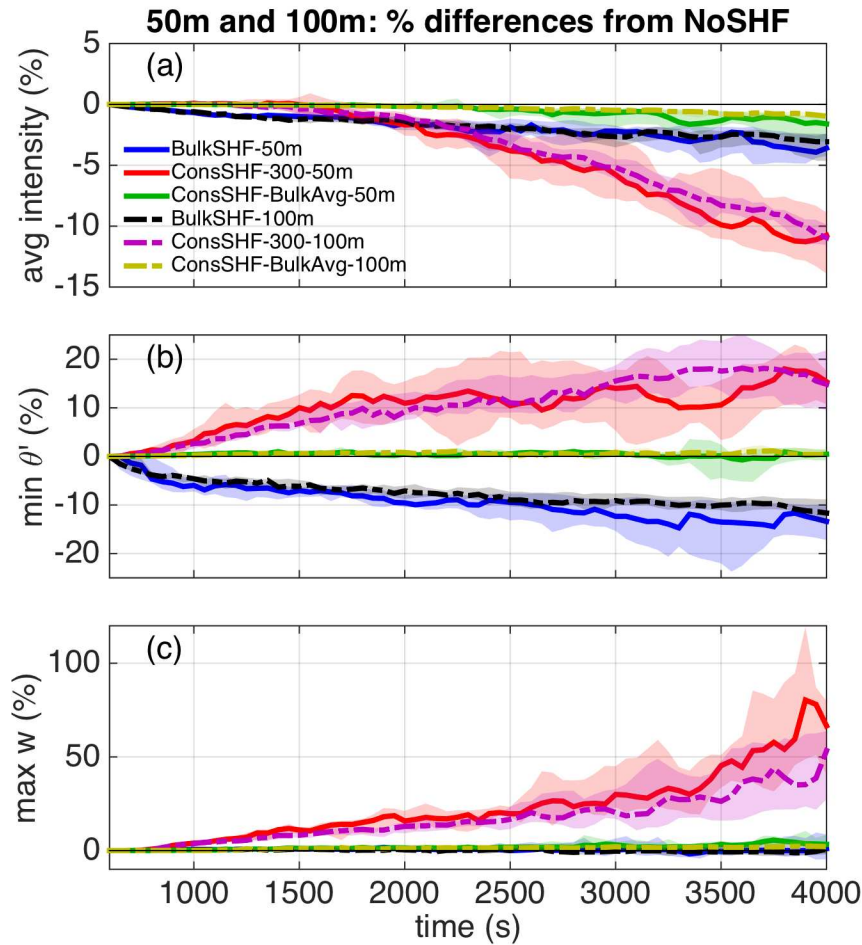
Figure 2.6: Time series of the same quantities shown in Figure 2.3; recall that panels a-b are calculated with cold pool perturbation quantities relative to the environment ahead of the cold pool (see section 2.2c). For each of the 12 initial cold bubble simulations in the 50m and 100m resolution experiment sets, percent differences from NoSHF were calculated for BulkSHF, ConsSHF-300, and ConsSHF-BulkAvg; results are shown as percentiles (solid line: 50th percentile; shading: 25th and 75th percentiles). Note that in panel (b), since minimum θ perturbations are negative, a positive percent difference indicates that the minimum θ perturbation is colder.
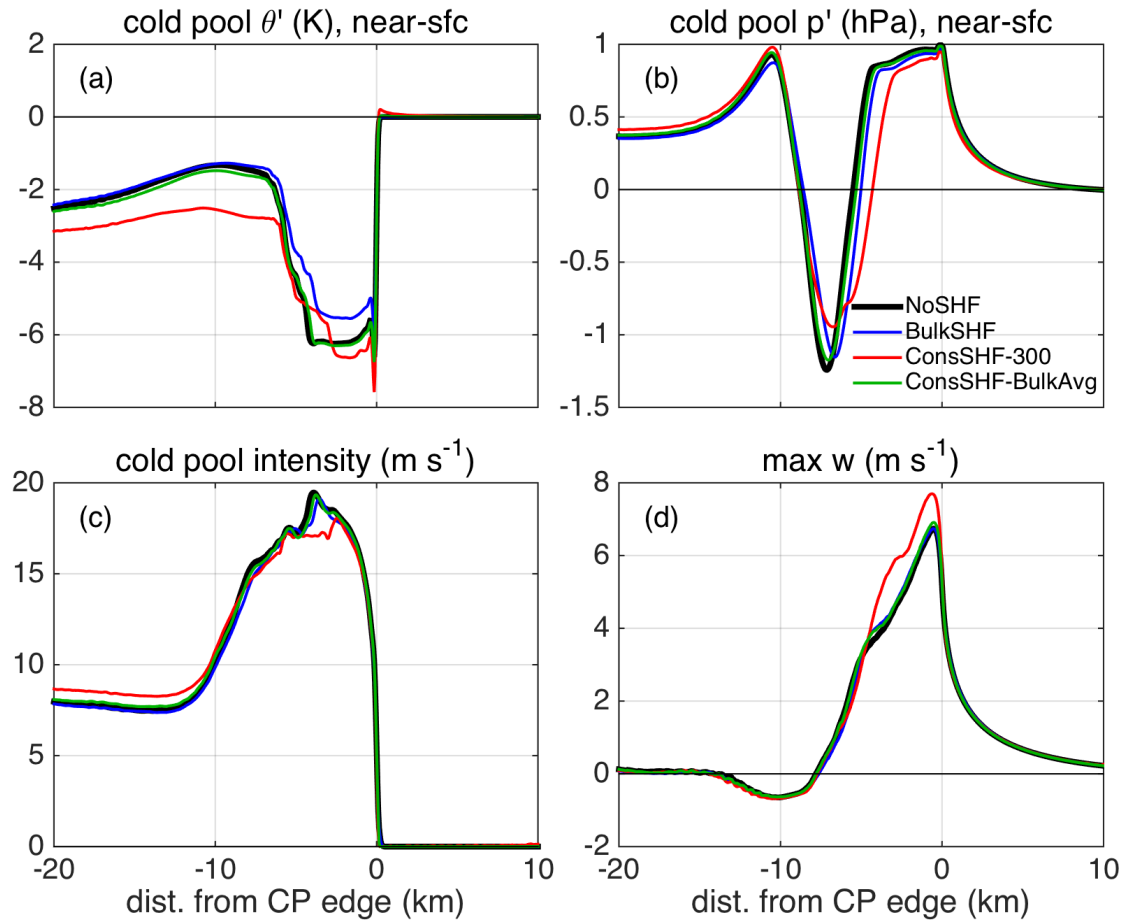
Figure 2.7: (a) Cold pool θ perturbation and (b) cold pool pressure perturbation at the lowest model level above ground (12.5 m); (c) cold pool intensity; and (d) maximum vertical velocity in non-cold pool air for the 50m-ElevWide-15 experiment set. All quantities are first subset relative to the cold pool leading edge and then temporally averaged between 1000 − 4000 s as described in section 2.2c. Cold pool perturbations are relative to the environment ahead of the cold pool.
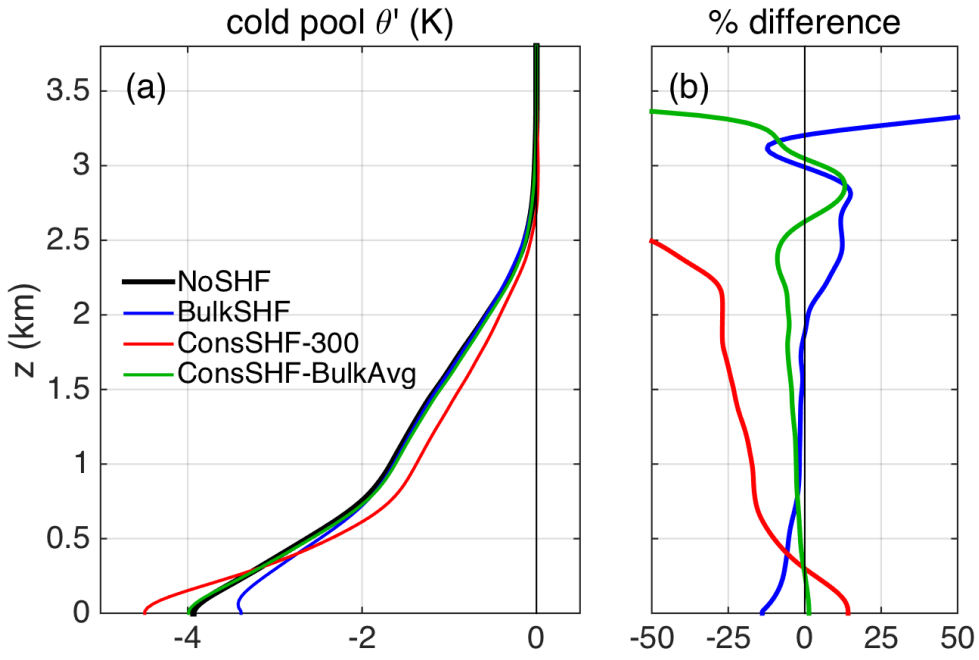
Figure 2.8: Profiles of (a) cold pool θ perturbation relative to the environment ahead of the cold pool, and (b) percent differences from NoSHF, averaged over 10 km behind the cold pool leading edge and temporally between 1000 − 4000 s, for the 50m-ElevWide-15 experiment set.
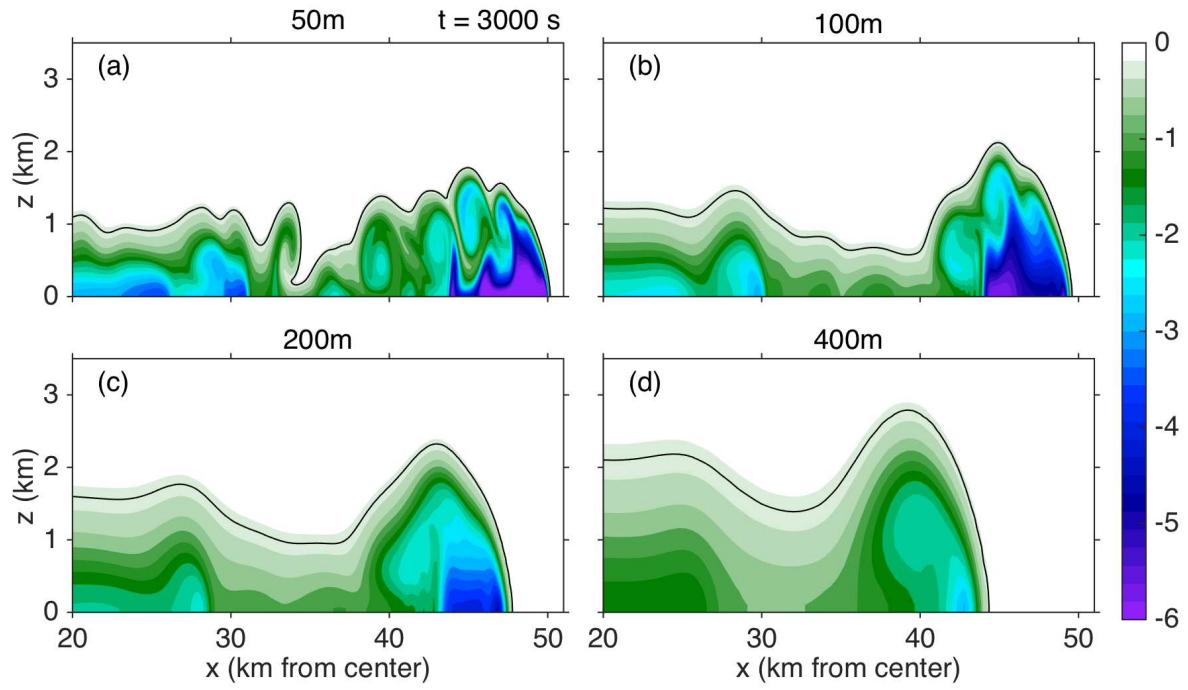
Figure 2.9: As in Figure 2.5, but for the NoSHF-SfcWide-15 simulations at 3000 s: (a) 50m resolution, (b) 100m resolution, (c) 200m resolution, and (d) 400m resolution.

Figure 2.10: Time series of the same quantities shown in Figure 2.3 and Figure 2.6. Percent differences from NoSHF were calculated for BulkSHF, ConsSHF-300, and ConsSHF-BulkAvg in each of the -15 K cold bubble amplitude experiments for the 100m, 200m, and 400m resolution simulations. Results shown are averaged over the four initial cold bubble configurations for each of the resolution tests as indicated in the legend.

CHAPTER 3: COLD POOL – LAND SURFACE INTERACTIONS IN A DRY CONTINENTAL ENVIRONMENT

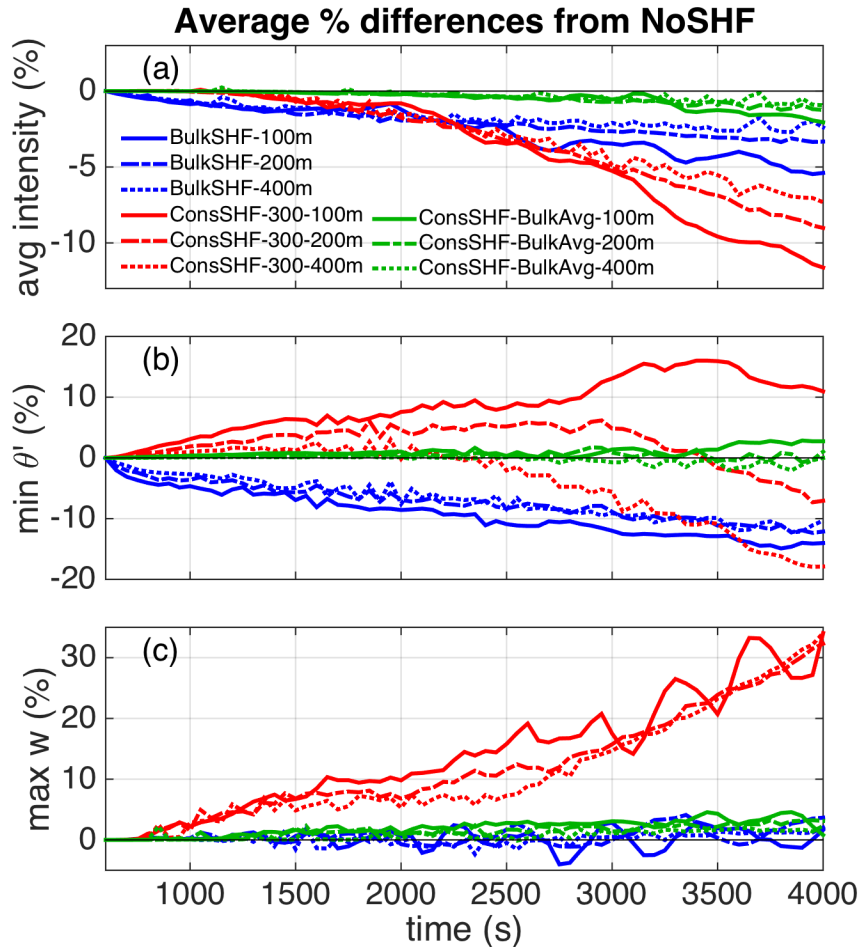## 3.1. Introduction

Any time a cloud produces rain, an evaporatively-cooled downdraft can form. If this chilled air reaches the surface, it spreads out as a cold pool. This means that cold pools can be found in all of Earth's environments, from moist, tropical oceanic regimes to dry continental regions. Cold pools behave like density currents (Benjamin 1968; Charba 1974). They can initiate new convection through lifting at their leading edge and by colliding with other cold pools (Purdom 1982; Rotunno et al. 1988), interact with boundary layer features (Achtemeier 1991; Grant and van den Heever 2016, hereafter GvdH16), and influence convective organization (Khairoutdinov and Randall 2006; Gentine et al. 2016).

Since cold pools occur at Earth's surface, it is important to consider how the surface interacts with cold pools. These interactions may vary considerably depending on the characteristics of the surface, including whether it is water or land, its temperature, and the land's soil and vegetation properties. Cold pool – ocean surface interactions are arguably the simplest case and can be approximated as one-way interactions since the ocean has a large thermal inertia and its surface is always saturated. Indeed, observational (Johnson and Nicholls 1983; Young et al. 1995; Saxen and Rutledge 1998; de Szoeke et al. 2017) and modeling studies (Trier et al. 1996; Tompkins 2001; Langhans and Romps 2015; Peters and Hohenegger 2017) have investigated enhancements in surface sensible heat fluxes (SHFs) and latent heat fluxes (LHFs) in oceanic cold pools. Such enhancements warm and moisten the cold pool with subsequent implications for cold pool dissipation and convective initiation. For example, Trier et al. (1996)

simulated a tropical oceanic squall line and concluded that the cold pool-induced surface fluxes notably reduced the cold pool area, ultimately decreasing convective initiation on its fringes later in the squall's lifecycle.

The more complex problem of cold pool – land interactions has received far less attention. Since SHFs can be much larger over land than over ocean, a few studies have investigated the one-way influence of SHFs on cold pools, including laboratory tank (Linden and Simpson 1986) and numerical experiments (Robinson et al. 2013; GvdH16). A consensus among these studies is that SHFs slow density current propagation and lead to dissipation. Both Linden and Simpson and GvdH16 attributed this to mixing with turbulent air ahead of the cold pool, which is intensified by surface heating.

Only a handful of studies have discussed cold pool properties in simulations with two-way land-atmosphere interactions (Del Genio et al. 2012; Gentine et al. 2016; Schlemmer and Hohenegger 2016; Drager and van den Heever 2017, hereafter DvdH17). Del Genio et al. showed that, contrary to oceanic cases, surface fluxes were suppressed within continental cold pools because the land surface under the cold pools rapidly cooled. DvdH17 demonstrated suppressed (enhanced) SHFs (LHFs) in the cold pool center because the ground was cooled and soaked by the rainy downdraft that generated the cold pool. Both of these studies were of moist tropical environments; the other two studies mentioned above did not discuss the land responses.

Evidently, a major knowledge gap exists regarding two-way cold pool – land interactions, especially in semi-arid environments – a particularly interesting scenario because of the low thermal inertia of drier land. Therefore, the goal of our study is to address the following two questions: (1) how does a cold pool influence the land surface in dry continental environments, in the absence of cloud effects such as precipitation and anvil shading; and (2) how does the land

surface's response alter the subsequent evolution of the cold pool and the boundary layer? We address these questions with idealized 3D large-eddy simulations (LES) of cold pools over a dry continental surface. An isolated cold pool is introduced into a convective boundary layer (CBL) with an interactive land surface, and the subsequent evolution of the land surface properties is analyzed to answer the first question. To address the second question, two simulations are compared, one with surface feedbacks and one without. We show that the cold pool – land surface interactions play a substantial role in the evolution of both the cold pool and the CBL, with implications for the representation and simulation both of cold pools and land surface processes in numerical models.

3.2. Model setup and initialization

We first examine the land surface's response to the cold pool in an LES simulation with an interactive land surface. The simulations were conducted with the Regional Atmospheric Modeling System (RAMS) version 6.1.18 (Cotton et al. 2003; Saleeby and van den Heever 2013), which is coupled to the Land Ecosystem-Atmosphere Feedback (LEAF) land surface model, version 3 (Walko et al. 2000a). LEAF prognoses soil and vegetation temperature and water content, including the effects of surface-atmosphere exchange following the parameterization by Louis (1979), radiative fluxes, and precipitation, although precipitation is not considered here.

We use 50 m horizontal grid spacing, a constant 20 m vertical grid spacing throughout the lowest 4 km and a stretched grid above this altitude to a maximum of 100 m vertical grid spacing, and a 0.5 s time step for the LES simulations. Such grid spacings permit adequate representation of the cold pool's turbulent characteristics and interactions with the surface

(Bryan et al. 2003; GvdH16). The 3D channel domain size of 200 km × 20 km × 10 km is comprised of 4001×401×294 points. Water vapor is not allowed to condense, i.e., microphysical processes are not activated, which eliminates the influence of cloud feedbacks on the analysis of cold pool – land surface interactions, thus allowing us to focus specifically on the questions we aim to answer. A semi-desert vegetation class with a normalized difference vegetation index of 0.1 is used to represent an idealized semi-arid climate like northern Africa, the southwestern United States, or Australia. Eight soil levels from 5 cm to 1.2 m in depth are used in LEAF. The soil temperature is initialized to be 10 K warmer than the lowest atmospheric level at the shallowest layer, and the soil temperature offset decreases exponentially with increasing depth at a scale depth of 15 cm. The soil moisture is initialized to 20% saturation fraction at all depths. Other physical parameterizations include the Harrington (1997) radiation scheme updated every 5 simulations minutes and a Smagorinsky (1963) turbulence scheme with stability modifications by Lilly (1962) and Hill (1974). A Rayleigh damping layer is included above 7 km AGL.

Before the cold pool is introduced, the simulation is integrated for two hours (from 12:00 to 14:00 LT) such that the CBL can fully develop. The initial conditions at 12:00 LT include a constant water vapor mixing ratio (r_v) of 10 g kg^{-1} and a constant potential temperature (θ) of 300 K over the lowest 1 km, and a surface pressure of 1000 hPa. Weakly stable conditions above 1 km are characterized by a constant Brunt-Väisälä frequency N_v, defined by $N_v^2 = \frac{g}{\theta_v}\frac{d\theta_v}{dz} = 5 \times 10^{-5}\ s^{-2}$ where θ_v is the virtual potential temperature (e.g. Emanuel 1994), and an exponentially decreasing r_v profile with a scale height of 2 km. The initial θ and r_v profiles at 12:00 LT are shown in Figure 3.1a,b. The initial wind profile is calm. For radiation calculation purposes, the date and latitude used in this simulation are 1 April and 20° N. Random θ perturbations are introduced over the lowest 500 m with a magnitude of 0.25 K that decreases

linearly with height in order to break the horizontal homogeneity. Periodic lateral boundary conditions are used in both the zonal and meridional directions. Model output is saved every 5 simulation minutes during this 2 hour time period. Over the course of the 2 hours, the CBL deepens to ~2 km (Figure 3.1a,b). By 13:30 LT, SHFs and LHFs have increased to average values of 300 W m^{-2} and 25 W m^{-2}, respectively (Figure 3.1c). The CBL profiles and surface flux magnitudes are representative of observations in semi-arid climates (e.g. Couvreux et al. 2012). The CBL gradually warms both from the SHFs and from entrainment of warmer free-tropospheric air, but it also dries because the entrainment of the drier free-tropospheric air outweighs the moistening by LHFs.

At 14:00 LT, a cold pool is introduced by adding a cold, dry, line-oriented bubble that is independent of the y-direction and therefore extends across the entire y-dimension. Hereafter, this simulation will be referred to as FB (surface FeedBacks included). The cold bubble is described by a cosine function with a vertical radius of 1 km, a horizontal (x-direction) radius of 8 km, and a perturbation θ (r_v) amplitude of -10 K (-10%) that is centered at 1 km AGL and at the domain center (Figure 3.2a). The cold bubble's line-type structure is representative of a cold pool created by linearly oriented convection or a large cold pool for which curvature along its edge can be neglected. The dry perturbation is representative of a cold pool that is created both by evaporative cooling and by transport of drier air from above the CBL by a downdraft. The zonal boundary conditions are changed to open-radiative (Klemp and Wilhelmson 1978) so that gravity waves excited by the cold pool can exit through the east and west boundaries, but the meridional boundary conditions are kept periodic. The linear cold bubble falls to the surface and spreads out in the x-direction over the course of the 2 hours, during which model output is saved

every minute. The simulations were performed on the Yellowstone supercomputing system (Computational and Information Systems Library 2012).

3.3. Land surface response to the cold pool

Key aspects of the FB simulation are illustrated by the instantaneous cross sections shown in Figure 3.2. The typical head structure and its associated circulation are obvious for the first 45 min (Figure 3.2b-d). After 45 min, the cold pool's structure is no longer well defined, though the remnant circulation remains evident throughout the simulation. A persistent circulation but lack of well-defined temperature structure was also seen in sea breeze simulations subject to gradual heating in Robinson et al. (2013). Turbulent features of the cold pool (such as Kelvin-Helmholtz waves) and of the CBL (such as convective plumes originating from the surface) are evident throughout the 2 hours. Mixing by these features leads to dissipation of the cold pool (GvdH16). The cold pool reaches 25 km from the domain center after 1 hour (13:00 LT), after which it no longer propagates outward (compare panels e and f in Figure 3.2). The coldest perturbations are found nearer the center of the cold pool. Finally, we see that the cold pool's influence on the mean CBL temperature and depth persists even after the cold pool has dissipated (Figure 3.2e-f).

Both the land surface and the near-surface atmospheric properties show signatures of the cold pool's presence that vary through time, as indicated in Figure 3.3. All quantities shown are perturbations relative to the environment, where the environmental quantities are defined as averages between 40 and 80 km away from the domain center in both the positive and negative x-direction; this environmental definition avoids both the center of the domain that is influenced by the cold pool and the 20 km near the lateral boundaries. We focus first on the SHF response to

the cold pool. SHFs are always enhanced relative to the environment near the leading edge of the cold pool (Figure 3.3d). The peak magnitude of this enhancement varies substantially with the cold pool's age. SHFs remain enhanced by 20 to 75 W m^{-2} between x = 20 and 25 km even at 15:30 and 16:00 LT, after the cold pool's structure is no longer distinguishable and it has stopped propagating (Figure 3.2). The SHF enhancement near the cold pool edge is strongly correlated with the near-surface wind speed (compare panels c and d in Figure 3.3), but its magnitude is modulated by the surface-air temperature difference as dictated by the near-surface air temperature (Figure 3.3a) and the soil temperature (Figure 3.3f).

SHFs are not always enhanced within the cold pool, however. After 45 min to 1 hour (14:45-15:00 LT), SHFs at the domain center are suppressed relative to the environment by up to 120 W m^{-2}. The suppressed SHF region extends to x = 9.5 km after 1 hour and to x = 17.5 km after 2 hours (16:00 LT) when its magnitude has decreased to around 50 W m^{-2} (Figure 3.3d). Notice that soil temperatures are most strongly suppressed from x = 2 – 15 km over the first hour, where the accumulated SHFs are greatest (compare panels d and f in Figure 3.3), and that the cool soil temperature anomaly persists for longer than the cool air temperature anomaly (compare panels a and f in Figure 3.3). The temporal lag in the soil temperature's response to the cold pool, in combination with slower wind speeds near the center as the peak winds expand outward in time, explain the persistent suppressed SHFs nearer the center of the aged cold pool.

LHFs are generally suppressed within the cold pool relative to the environment, except near the cold pool's leading edge for the first 30 min (Figure 3.3e). These early LHF peaks correspond to the leading edge of the wind speed perturbations (Figure 3.3c). The suppressed LHFs after 30 min are related to enhanced water vapor within the cold pool (Figure 3.3b). Given the anticorrelation between LHF and r_v perturbations, the LHFs do not appear to significantly

influence the moisture distribution within the cold pool. Rather, the enhanced moisture can be explained by the differential CBL growth (Figure 3.2). Within the stable cold pool, CBL growth is suppressed and r_v remains steady. On the other hand, in the environment, the CBL dries as its depth increases (Figure 3.1b) because the entrainment of drier free-tropospheric air outweighs moistening by LHFs. This leads to a positive r_v perturbation that grows in time.

3.4. Cold pool – land surface feedbacks

While we have shown that the cold pool does influence the surface fluxes (particularly the SHFs), it is unclear to what extent the interactive surface affects the cold pool's subsequent evolution. For instance, the enhanced SHFs near the edge and suppressed SHFs near the center should result in cold pool dissipation from the edge inward; however, the cold pool could dissipate from the edge inward regardless of the SHF pattern, simply through turbulent mixing between the cold pool air and the CBL plumes which is most vigorous at the edge. This brings us to our second question: How does the land surface's response to the cold pool influence the subsequent evolution both of the cold pool and the CBL? To address this question, an additional simulation called NOFB (No surface FeedBacks) is performed. NOFB is identical to FB in all respects except that the cold pool – surface flux interactions are removed by imposing spatially uniform but time-varying SHFs and LHFs. The imposed surface flux values are the environmental averages from the FB simulation (Figure 3.1c).

Figure 3.4, which details a comparison between the FB and NOFB simulations, reveals that the cold pool – land surface interactions do exert a significant influence on the cold pool's evolution. One of the most obvious differences between the two simulations is in how far the cold pool propagates. In FB, recall that the cold pool stops propagating after an hour, when it has

reached ~25 km from the center. However, in NOFB, the cold pool propagates faster and continues to propagate outward throughout most of the 2 hours (Figure 3.4b). The cold pool dissipation timescale is therefore about twice as long in the NOFB simulation compared to the FB simulation. The propagation differences translate to a 60% increase in final cold pool extent in NOFB (Figure 3.4d).

Cold pool propagation speed is related to cold pool intensity, or integrated negative buoyancy, which we calculate from the composite fields as $C^2 = 2 \int_0^D -B dz$ (Benjamin 1968), where C is the intensity, $B = g \frac{\theta_v'}{\theta_{vE}}$ is the buoyancy, θ_{vE} is the environmental-average profile of θ_v, and the cold pool top D is defined as the lowest altitude where $u = 0$ (the lingering effects of the cold pool on B after it has dissipated preclude us from using a buoyancy threshold to define D). C is calculated only for columns where $D < 2$ km and where $B < -0.005$ m^2 s^{-2} somewhere below D, otherwise, C is set to 0. Figure 3.4d indicates that the maximum intensity increases in NOFB by up to 30%, in keeping with its faster propagation. A similar story is told by the near-surface temperatures: minimum θ_v perturbations are 10-30% stronger throughout the first hour, and the entire cold pool is colder for the first 35 min, in NOFB compared to FB (Figure 3.4c). In the FB simulation, the cold pool's faster dissipation, smaller extent, and weaker intensity are all attributable to the enhanced SHFs near its leading edge, which warm the cold pool air and hasten its dissipation. Interestingly, the influence of enhanced SHFs within the cold pool is much larger here than in GvdH16, most likely because the cold pools did not propagate into an active boundary layer in that study.

Recall that in FB, SHFs are always enhanced near the edge but are eventually suppressed in the center of the remnant cold pool. Such a pattern should lead to dissipation of the cold pool from the edge inwards, and indeed this is the case, as can be inferred by the slope of the θ_v'

contours (Figure 3.4a). In NOFB, on the other hand, the θ_v' contours slope in the opposite

direction between x=0-20 km (Figure 3.4b), meaning the cold pool dissipates from the center

outwards. As a result, despite the colder temperatures throughout most of NOFB, temperatures

are actually warmer in the center of the NOFB cold pool starting at 35 min (Figure 3.4c).

The difference in evolution between the FB and NOFB cold pools that arises due to the

inclusion of an interactive surface ultimately affects the CBL structure (Figure 3.5). We show the

15:00-15:30 LT period because the CBL is beginning to recover and differences in CBL

structure between the two cases are most clear. The recovery of turbulent kinetic energy (TKE)

and CBL depth to ambient conditions is slowest near the center of the FB cold pool, since TKE

decreases in intensity toward the cold pool center (Figure 3.5a). The slowest recovery in the

center coincides with the region of suppressed SHFs throughout the 2nd hour (Figure 3.3d). But

in NOFB, the TKE and CBL depth are most suppressed from x=10-25 km, while TKE increases

in intensity from around x=15 km toward the center (Figure 3.5b). The faster TKE recovery in

the NOFB cold pool's center coincides with the warmer θ_v' values compared to the FB case

(Figure 3.4c), and results both from the lack of spatial variability in SHFs and from the advection

of cooler temperatures away from the center by the cold pool circulation.

Another clear difference between the two CBLs is the magnitude of peak TKE intensity.

In both cases, a local TKE maximum appears within and near the leading edge of the cold pool

in association with shear in the mean circulation (Figure 3.5). However, the magnitude of the

TKE maximum is noticeably greater in FB than in NOFB. Some of the apparent increase in

magnitude results from a slight smearing of the NOFB composite TKE because the NOFB cold

pool is still propagating outward during this time period. However, the peak composite TKE

intensity at individual times is more intense (by up to 35%) in the FB case than in the NOFB

case throughout the 2nd hour. The enhanced SHFs near the leading edge of the remnant cold pool in FB lead to greater near-surface available energy, locally more vigorous and turbulent convective plumes, and the resultant greater TKE intensity seen in Figure 3.5. The boundary layer is also locally deeper there. This means that the cold pool could initiate new convection even after its buoyancy anomaly has dissipated, an effect that is enhanced with an interactive surface.

3.5. Summary and implications

This study, to our knowledge, represents the first investigation of the land surface's response to cold pools in dry environments and is the first to explicitly demonstrate the significant impacts of the interactive land surface on the process-scale evolution of the cold pool and the boundary layer. Specifically, we aimed to answer two questions: (1) how does a cold pool influence the land surface in a dry continental environment in the absence of cloud influences like rain and anvil shading? and (2) how does the land surface's response to the cold pool influence the subsequent evolution of the cold pool and the convective boundary layer (CBL)? To investigate these questions, we performed idealized LES simulations of cold pools in a daytime, dry-continental CBL, both with and without an interactive land surface. In the simulation with an interactive surface, we found that SHFs were always enhanced near the cold pool edge, largely due to stronger wind speeds. However, SHFs were suppressed near the cold pool's center later in its lifetime due to cooler soil temperatures and lower wind speeds. LHFs were generally suppressed within the cold pool because r_v was higher in the cold pool than in the environment. The positive r_v perturbations resulted from suppressed CBL growth and therefore reduced boundary layer entrainment drying in the cold pool region.

We found by comparing the interactive and non-interactive land surface cases that the cold pool – land surface feedbacks exert a strong influence on the cold pool evolution. When an interactive land surface was used, the cold pool was weaker throughout its lifetime and therefore propagated more slowly, dissipated twice as quickly, and was nearly 40% smaller in extent compared to the prescribed fluxes case. These significant changes were attributed to the enhanced SHFs near the cold pool's leading edge in the interactive surface case, which also led both to dissipation of the cold pool from the edge inwards and to a locally more vigorous and energetic CBL near the remnant cold pool's edge. Finally, the suppressed SHFs in the center slowed the CBL recovery there.

Since surface fluxes within the cold pools can either be suppressed or enhanced relative to the environment, the spatiotemporal surface flux patterns are more complex for land than for ocean surfaces studied previously (see references in section 3.1). DvdH17 even documented negative SHFs in the cold pool center where the ground was soaked by rain, an effect not incorporated in this study. Including rain influences on soil moisture and temperature would amplify our SHF suppression and further delay the CBL recovery at the cold pool center.

While we have documented generally suppressed LHFs within the cold pool, LHF perturbations are likely to be highly sensitive to both the environment and surface conditions. For instance, both the r_v and LHF perturbations in the cold pool could reverse sign depending on whether the CBL is in a moistening or drying regime, which in turn depends on the ratio of the entrainment flux at the CBL top to the surface moisture flux (e.g. Mahrt 1991; Mellado et al. 2017). Additionally, a rain-soaked ground can complicate the spatiotemporal LHF pattern within the cold pool (DvdH17). LHF patterns and moisture structure within continental cold pools clearly merit further study.

Our results explicitly highlight the importance of utilizing an interactive land surface in process studies of cold pools, in agreement with recommendations by GvdH16, Gentine et al. (2016), and DvdH17. We speculate from these results that the reduced cold pool extent and faster dissipation in the interactive surface case could, to first order, decrease the spatiotemporal scales of convective initiation, the spatial scales of boundary layer heterogeneity, and the probability of cold pool collisions. These speculations are supported by the findings reported in Trier et al. (1996) and Gentine et al. (2016) that including cold pool – surface interactions alters convective initiation and organization. Such important effects of interactive surfaces should be considered in forecasting applications and in cold pool parameterizations (e.g. Del Genio et al. 2015). Finally, nearly all cold pool – land surface interaction studies to date have exclusively utilized numerical models. New measurement techniques, such as the use of thermal imagery to measure spatiotemporal variability in surface fluxes (e.g. Morrison et al. 2017; Lee et al. 2017), are promising avenues both to validate modeling results and to extend process studies of cold pool – surface interactions to other environments.
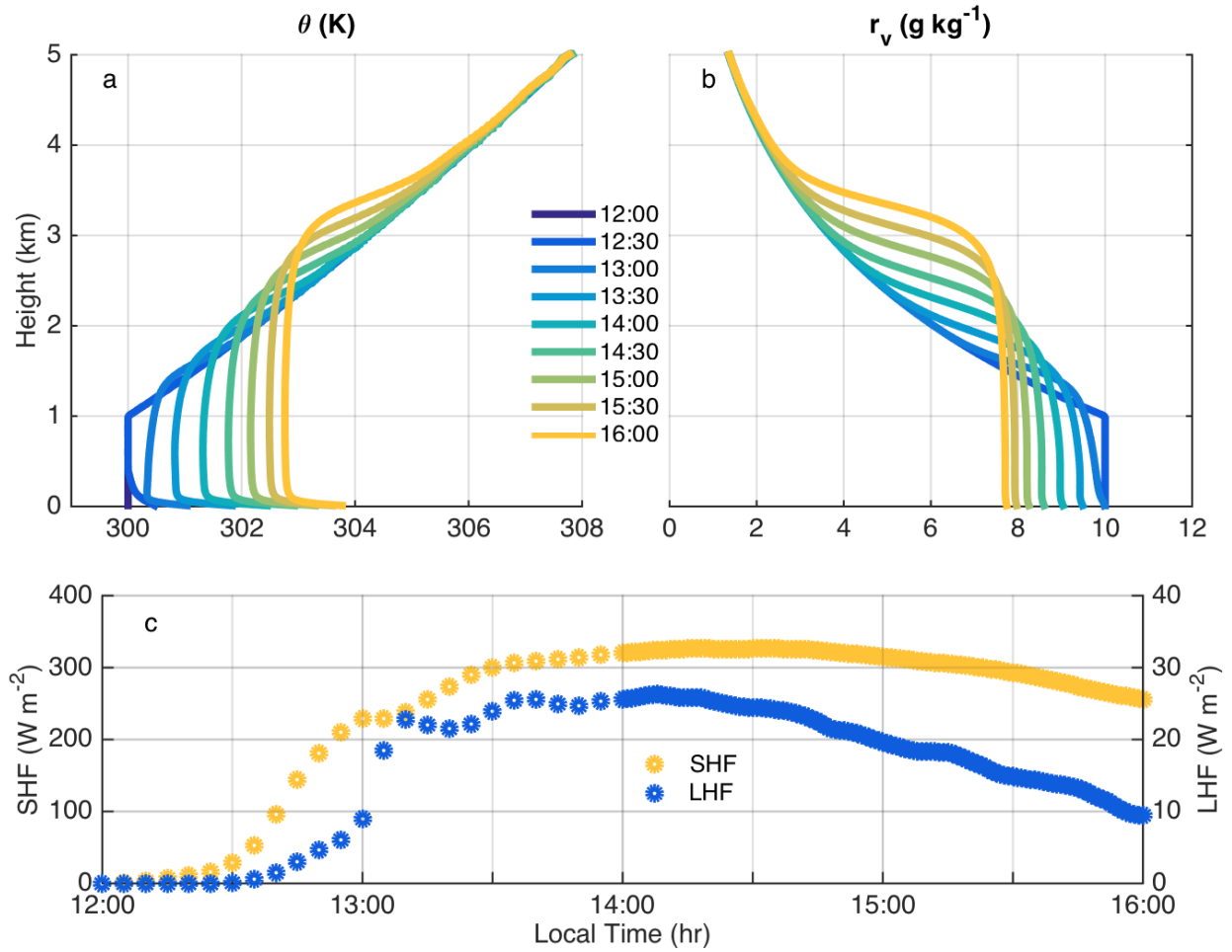
3.6. Figures

Figure 3.1. Environmental profiles of (a) θ and (b) r_v every 30 min from 12:00 to 16:00 LT for simulation FB. Environmental quantities are defined as averages between 40 and 80 km away from the domain center. (c) Time series of environmental SHF and LHF in FB.
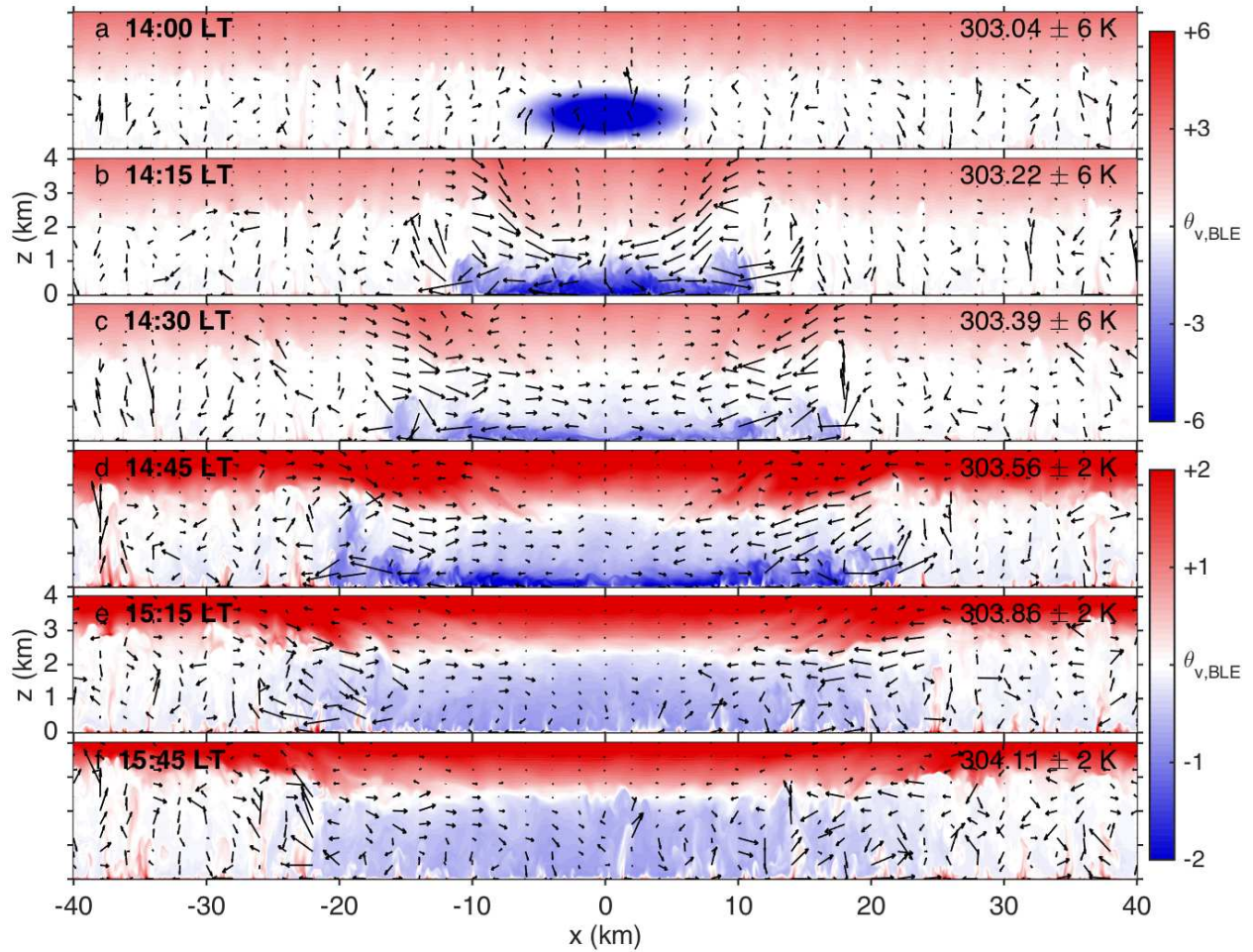
Figure 3.2. Instantaneous cross sections of θ_v (shaded) and $[u,w]$ wind vectors through the domain center at different times for simulation FB. The colorbar in each panel is centered on $\theta_{v,BLE}$ (the 0-2 km AGL and environmental average of θ_v), which is listed in the upper right of each panel along with the colorbar limits. Note the change in the colorbar limits from panels (a)-(c) to panels (d)-(f), and the change in time interval of 15 min for (a)-(d) to 30 min for (d)-(f).
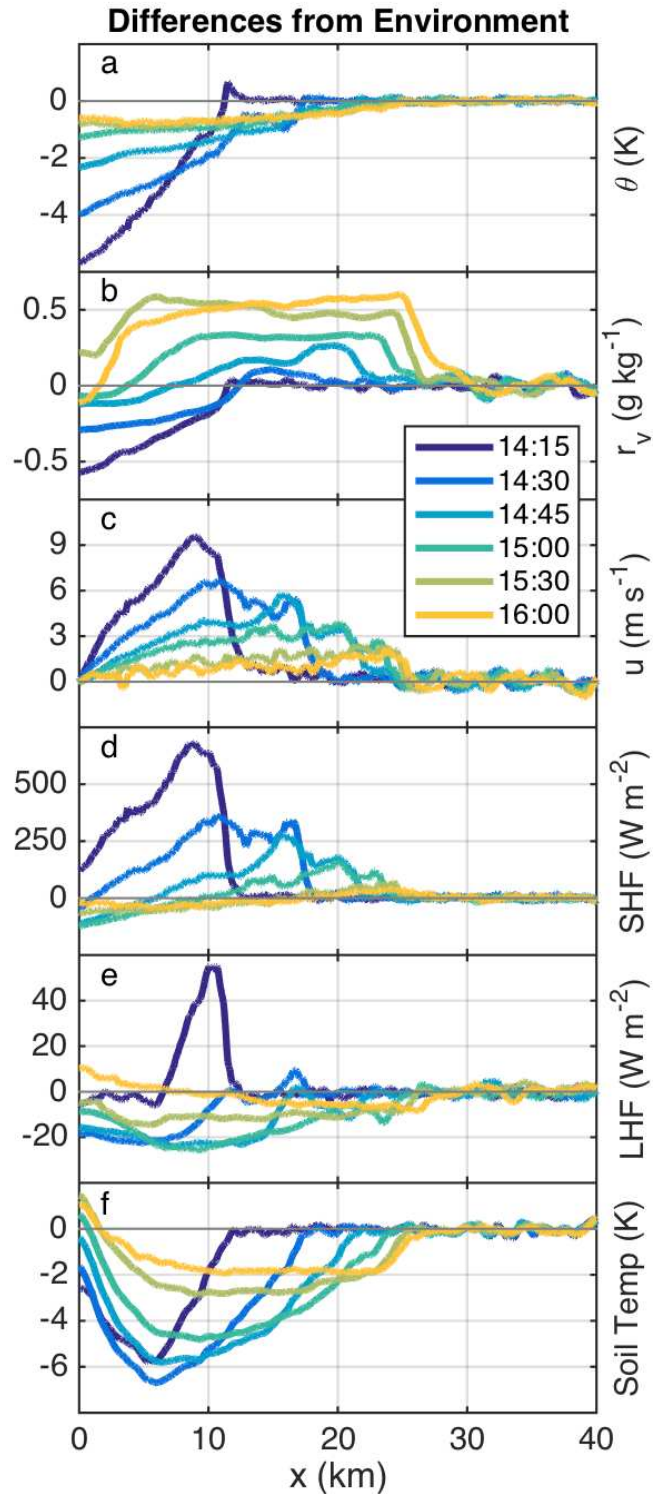
Figure 3.3. Composite line plots of perturbations relative to the environment every 15 min from 14:15 to 15:00 LT and every 30 min from 15:00 to 16:00 LT (see legend). Panels (a) – (c) show quantities at the lowest atmospheric level (10 m AGL), and panels (d) – (f) show land surface quantities (soil temperature is for the shallowest soil layer). Composites were created by averaging in the y-direction and then averaging the right half of the domain with a mirror image

of the left-half of the domain. Hence u in panel (c) is the wind component away from the domain center.
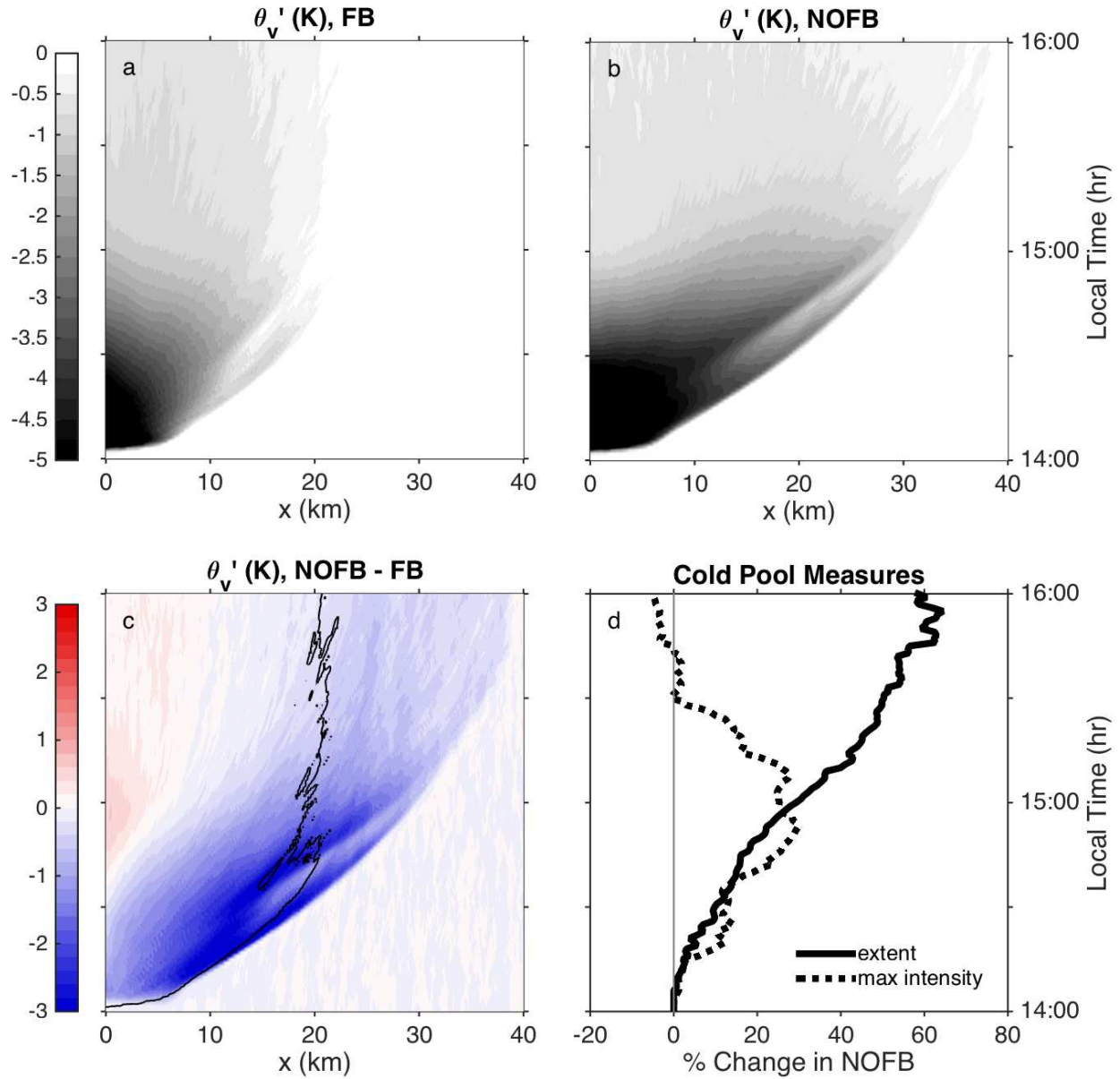
Figure 3.4. Composite Hovmöller of θ_v' relative to the environment at 10 m AGL for (a) FB, (b) NOFB, and (c) NOFB minus FB. In (c), the -0.25 K θ_v' contour for FB is included for comparison. (d) Percent increase in composite cold pool extent, and in maximum composite intensity (C) within 10 km of the leading edge, as a function of time in simulation NOFB relative to FB. Cold pool extent is defined as the farthest distance from the domain center where $C > 0$. See text for the definition of C.

70

Figure 3.5. Cross sections of composite TKE (shaded) and [u,w] wind vectors, averaged over 15:00-15:30 LT, for (a) FB and (b) NOFB. TKE $= 0.5(u'^2 + v'^2 + w'^2)$ and perturbation wind components are calculated at each time by subtracting the y-average.
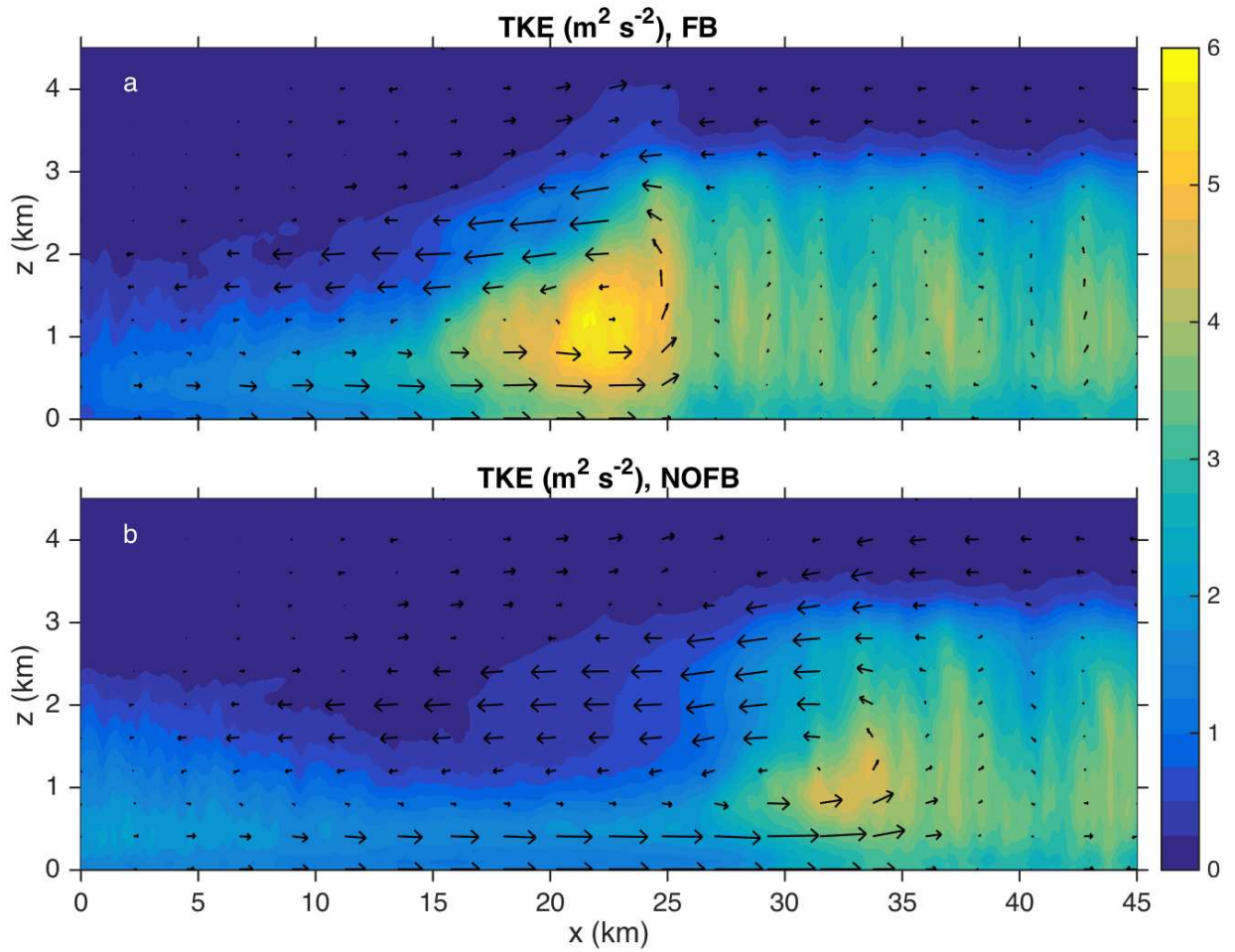
CHAPTER 4: A PRELIMINARY C³LOUD-EX CASE STUDY: "THE BEES DAY"

4.1. Cold pool observations

Thus far, the research in this dissertation has focused on idealized numerical experiments conducted to understand cold pool interactions with the land surface, with implications for impacts on convection. Idealized simulations are extremely useful for examining hypotheses at a process scale because the control experiment and sensitivity tests can be designed in such a way to understand and assess the importance of specific physical processes and their interactions. Observational studies are also critical, both to provide new insights into realistic situations and to evaluate hypotheses resulting from numerical (and theoretical) research. Important observational needs arising from the cold pool – land surface study results presented in Chapter 2 and Chapter 3 include (1) knowledge of surface flux responses to cold pools, and (2) the documentation of variability in cold pool internal structure.

Observational studies of cold pools have been previously conducted, many of which were focused on surface measurements of cold pools (e.g. Byers and Braham 1949; Engerer et al. 2008). Since surface measurements are not always correlated to the above-surface cold pool properties (Bryan et al. 2005; Trier et al. 2006; Engerer et al. 2008; Grant and van den Heever 2016), measurements through the depth of the cold pool are also needed. A few early cold pool studies documented cold pool properties above the surface using instrumented towers that reached above 400 feet (Charba 1974; Goff 1976), but this is insufficient to capture the full vertical structure of cold pools with depths greater than the tower height and also depends on the somewhat fortuitous circumstance that the cold pool passes over the tower. Radar measurements can provide detailed spatial and temporal information about cold pool reflectivity and velocity

through the depth of the cold pool (Wakimoto 1982; Mueller and Carbone 1987; Soderholm et al. 2016), but these data lack thermodynamic information. Soundings do provide the necessary thermodynamic information through the cold pool depth (e.g. Bryan et al. 2005; Bryan and Parker 2010) but are more limited in spatiotemporal coverage than radars and surface station networks. It therefore appears ideal to combine multiple measurement capabilities.

One of the main goals of the C^3LOUD-Ex (CSU Convective CLoud Outflows and UpDrafts Experiment; van den Heever et al. 2017, in prep.) field campaign was to obtain measurements of cold pools above the surface using multiple instrument platforms. Thirteen C^3LOUD-Ex cold pool cases were documented during July 2016 and May-June 2017 in northeastern Colorado and southeastern Wyoming. Cold pool data obtained include radar scans from the CSU CHILL research radar, soundings ahead of and within cold pools, and time series of thermodynamic information from portable surface weather stations and drones. Additionally, infrared cameras were attached to the drones in order to sense ground emissivity and therefore temperature before and after the cold pool's passage. One cold pool case in particular that occurred on 17 May 2017 is examined here because it was isolated from its parent convection and the environmental conditions it experienced were similar to the environments of the cold pools simulated and analyzed in Chapter 2 and Chapter 3, including sunny conditions, a turbulent boundary layer, and the semi-arid climate.

4.2. C^3LOUD-Ex case study: 17 May 2017, "The Bees Day"

17 May 2017 is fondly termed "The Bees Day" by the C^3LOUD-Ex field campaign team because the mobile soundings, drones, and surface stations were initially positioned right next to a bee farm (clearly, operations were moved down the road to avoid being in such close vicinity

to thousands of bees!). The cold pool was produced by a convective cluster that formed along the Cheyenne ridge just to the southeast of Cheyenne, WY (Figure 4.1). The cold pool propagated southward away from its parent convection, toward the CSU CHILL radar and the deployment location near Pierce, CO (4 km east of US Highway 85 along County Road 94). Three specific deployment positions were used to observe the cold pool: an ANCHR point, a 100M point which was located 100 m to the east of the ANCHR point, and a 1KM point which was located 1 km to the east of the ANCHR point.

The gust front passed the deployment locations between 20:00 and 20:30 UTC. The cold pool's leading edge is clearly outlined by a line of enhanced reflectivity in the CHILL PPI sector scans (Figure 4.2a,c), and inbound velocities are around 10 m s^{-1} within the cold pool to the north of the reflectivity line (Figure 4.2b,d). Weak cellular structures can be seen in the reflectivity field at 20:01 UTC (Figure 4.2a), suggesting that the boundary layer ahead of the cold pool was turbulent. The RHI scans through the cold pool at 20:25 UTC (Figure 4.2e,f) depict a classic density current structure: a locally deeper head region is visible at ~22 km from the radar with forward flow within the cold pool and return flow aloft. The cold pool head is about 1.5 km deep at the time shown (depth is estimated from the vertical extent of the forward flow). Additional RHI azimuth scans at different times suggest that the cold pool depth was generally between 1 and 1.5 km throughout the sampling time period, though it occasionally approached 2 km.

Two InterMet sounding systems were deployed, one at the ANCHR point and the other at the 1KM point. Pairs of soundings were launched simultaneously at four different times for a total of eight soundings describing this case (Figure 4.3). Paired launches were separated by about 20 min and are referred to as the PRE, CP1, CP2, and CP3 sounding sets. PRE soundings were launched before the cold pool passage (19:36 UTC; Figure 4.1), CP1 after a shift in surface

wind direction was evident in the surface station measurements (20:01 UTC; Figure 4.2a,b), CP2 after wind speeds had increased and it was clear that the leading edge of the cold pool had passed (20:23 UTC; Figure 4.2c,d), and CP3 well after the cold pool front had passed (20:42 UTC). Additionally, a Davis Vantage Pro2 portable surface station and a pair of stacked drones sampled conditions at each of the three deployment positions, although the drone data are currently undergoing quality control and further bias testing and hence are not discussed here. The data collected by the surface stations spans the duration of the four sets of sounding launch times (Figure 4.4).

The PRE soundings show characteristics of a typical daytime boundary layer, namely, a statically unstable layer in the lowest few hundred meters (Figure 4.3a) and relatively well-mixed water vapor profiles (Figure 4.3b)[10]. The PRE 1KM sounding is notably cooler than the PRE ANCHR sounding throughout the lowest 500 m, and the wind speed and direction also vary between the two soundings (Figure 4.3a,c,d). These differences are likely attributable to the boundary layer variability (e.g. the cellular structures noted in Figure 4.2a).

Between the PRE and CP1 launch times, all of the near-surface quantities were relatively steady with the exception of wind direction (Figure 4.4). Winds began to shift from easterly/southeasterly to northeasterly starting 5-10 min before the CP1 soundings were launched (in fact, the decision to launch the CP1 soundings was made because of this wind shift). Interestingly, Byers and Braham (1949) remarked that the Thunderstorm Project cold pool observations often showed a wind shift well before the temperature drop appeared. The CP1

---

[10] All soundings are substantially warmer (2 – 6 K) and moister (1-2 g kg^{-1}) in the lowest 50 m above ground than in the 50 m – 250 m layer. It is unclear at this time whether these vertical gradients represent a real surface effect, an artifact due to the difference in ventilation rate when the sonde is actively de-reeling compared to when it is fully de-reeled, or some combination of these two factors. As such, these near-surface features are not discussed further here.

profiles show clear changes from the PRE soundings taken 25 min earlier. Namely, the CP1 θ and water vapor mixing ratios are both well-mixed, and the air is warmer and drier through the lowest 1 km than in the PRE soundings. The CP2 launch time marked the beginning of the cold pool's signature in the surface fields, including a subtle temperature drop, an increase in humidity, a steady increase in wind speed, and backing of the winds (Figure 4.4). The CP2 and CP3 soundings both show cooling and moistening relative to the PRE and CP1 soundings and strong northeasterly winds through the lowest 1 to 1.5 km (Figure 4.3), suggesting a cold pool depth in line with the radar observations (Figure 4.2e,f).

4.3. Discussion

This case study displays many similarities to the idealized cold pool simulations analyzed in Chapter 3 and to the ConsSHF cases discussed in Chapter 2. First, the environments were similar, including the turbulent boundary layer, the sunny and clear conditions (emulated by the large SHFs in the 2D simulations), and a semi-arid climate. Second, the simulated cold pools were isolated and did not interact with convection, which is an idealization of scenarios such as this where the cold pool propagates away from its parent convection and remains isolated from other cold pools. Third, the characteristics of the observed and simulated cold pools are similar, including the cold pool depths, temperature perturbations, wind speed magnitudes, and in the case of the 3D cold pool simulation, the positive water vapor perturbations (although the water vapor result could be coincidental, since rain evaporation was not included in the simulations and the soil moisture and latent heat fluxes are unknown for the observed case).

The commonalities in the environments and the cold pool characteristics suggest that similar processes are at work in this case study and in the idealized simulations. The simulations

can therefore be used to guide physical interpretation of the observations and the observations can lend support to conclusions drawn from the idealized simulations. For instance, the well-mixed, warmer profiles seen in the CP1 soundings compared to the PRE soundings can be explained by considering what a virtual sounding would look like if it were released ahead of the ConsSHF cold pool shown in Figure 2.5c, beginning around x = 60 km. This virtual sounding would likely rise up and over the cold pool under the influence of its head circulation, thereby sampling the warm lofted air ahead of the cold pool and resulting in a similar profile to the CP1 soundings. Additionally, the surface observations (Figure 4.4) can be interpreted in the context of the interactive surface results shown in Chapter 3. All three surface stations indicate warming of 0.5 to 1 K in the 20:00 – 20:20 UTC time period relative to the pre cold pool conditions. In fact, the peak warming occurs after the wind speeds have started to increase. Subsequently, the temperatures dropped after 20:30 UTC to at most 1 K colder than the pre-cold pool values. The period of warming and the weak cold perturbations may be a result of enhanced sensible heat fluxes near the cold pool's leading edge as seen in the CP-FB simulation (Figure 3.3). This inference lends support to the important roles of both surface fluxes and mixing in contributing to the cold pool evolution (Chapter 2 and Chapter 3). Finally, the clear signal of persistent wind speed enhancements within the cold pool, despite the weak temperature perturbations, lends support to the statements in Chapter 3 regarding the cold pool's influence on the boundary layer circulations even after its buoyancy anomaly has dissipated (Figure 3.5), thereby highlighting its potential role in convective initiation.

A key question remains: how do sensible heat fluxes vary within observed cold pools? Such measurements are crucial to further our understanding of cold pool – land surface interactions. As mentioned in section 4.1, thermal cameras were mounted onto three of the

drones, and these cameras faced the ground in order to sense emitted thermal energy and therefore the ground temperature. At this time, sensible heat fluxes cannot easily be determined from the IR images obtained during C^{3}LOUD-Ex because extensive testing at a flux tower has not yet been performed. However, the ground temperature can be estimated, which would provide interesting insight into the land surface responses to the cold pool discussed in Chapter 3 (see Figure 3.3). Quality control regarding the IR camera's field of view and corrections due to the drone's altitude and to the atmospheric temperature and humidity are currently underway, which will permit a detailed investigation of the ground temperature response to the cold pools. Only one IR camera was available and operational on The Bees Day. Although not shown here, a preliminary look at the uncorrected IR data indicates that shadows from cumulus clouds developing along the cold pool's leading edge passed overhead just minutes before the gust front's arrival and then again minutes after its passage. The IR imagery suggests that the ground temperatures respond to the cloud shadows within 5-10 seconds of the shadow's passage, and these cloud shadow temperature responses are more obvious than any response to the cold pool's presence itself (or perhaps the strong effects of the cloud shadows on the ground temperature simply masked the cold pool – induced ground temperature changes).

4.4. Summary

It has been demonstrated that observations of "The Bees Day" cold pool case study collected during the C^{3}LOUD-Ex field campaign, and the isolated continental cold pool simulations examined in Chapter 2 and Chapter 3, exhibit similar characteristics. As such, similar physical processes are likely to be relevant in both the numerical experiments and the observations. Hence the observations lend support to the modeling study conclusions that

turbulent mixing is important for cold pool dissipation and that cold pool – land surface interactions regulate cold pool evolution in dry continental environments. Additionally, the simulation results lend insight into the physical reasoning for the signals and trends associated with the passage of the cold pool that are evident in the collected observations.

The fast response of the ground temperature to the cloud shadows discussed in section 4.3 raises the question, what is the role of clouds (both via precipitation and cloud shading) in regulating cold pool – surface flux interactions? Twelve other cold pool cases were documented during C^{3}LOUD-Ex for a range of cold pool strengths and storm types that produced them, and many of these cases include imagery from multiple IR cameras. It will be interesting to explore whether the ground temperature response to cold pools is more easily detectable for stronger cold pools and in scenarios where solar radiation was blocked by anvil shading before the cold pool passed, and to investigate the timescale of ground temperature response to cloud shadows in the other cold pool cases.

4.5. Figures
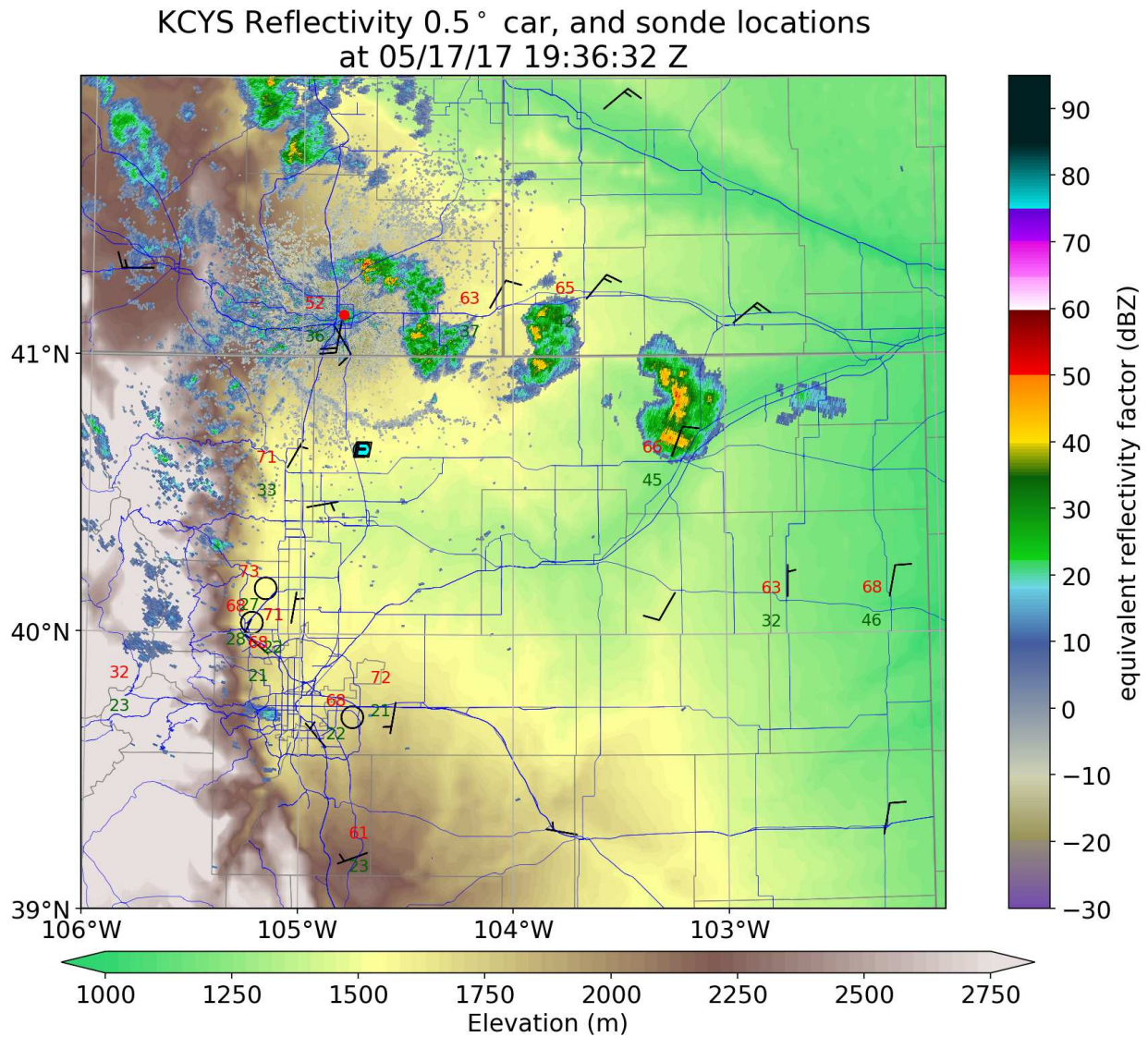
Figure 4.1. Plan view of the Cheyenne radar (KCYS) reflectivity at 0.5° tilt (shaded; see colorbar at right) at the time of the PRE sounding launches (see text). The underlying shading shows terrain (see bottom colorbar), and the car and sonde positions are indicated by black letters and cyan dots, respectively. Regional surface station observations display wind barbs, temperature (red text), and dewpoint temperature (green text). The location of KCYS is shown by the red dot. Figure provided by S. W. Freeman.
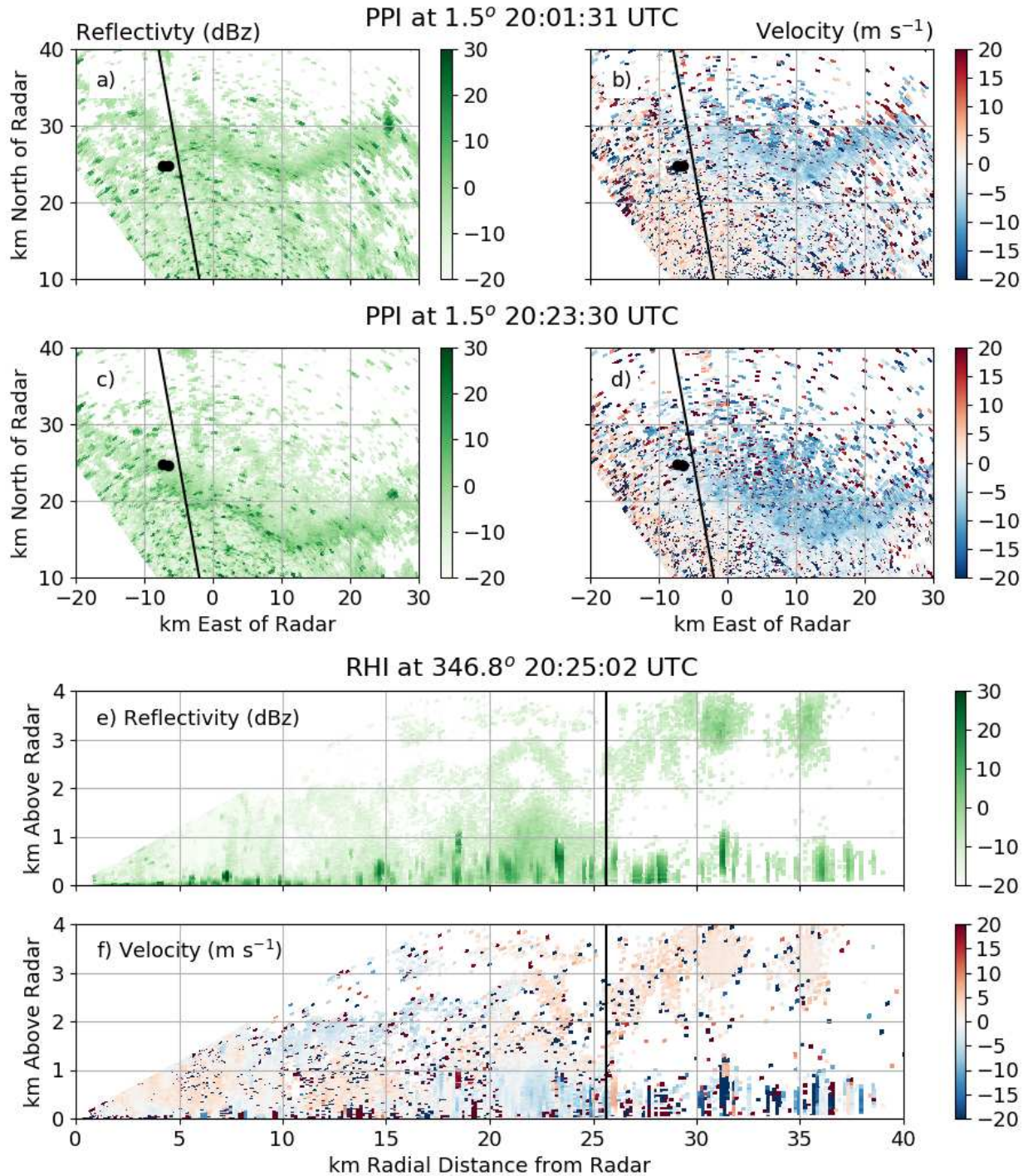
Figure 4.2. (a-d) CHILL PPI scans at 1.5° elevation angle at two different times corresponding to sounding sets CP1 and CP2, respectively (see text): (a,c) reflectivity and (b,d) velocity. The two black dots indicate the ANCHR and 1KM deployment locations. (e,f) RHI scan of reflectivity and velocity at 346.8° azimuth as indicated by the black line in panels (a-d); the RHI scan time is shortly after the CP2 sounding sets. The black vertical line indicates the sampling position. In all panels, data are plotted only where the normalized coherent power is greater than 0.2 in order to eliminate some of the signal noise. Figure provided by P. J. Marinescu.

81
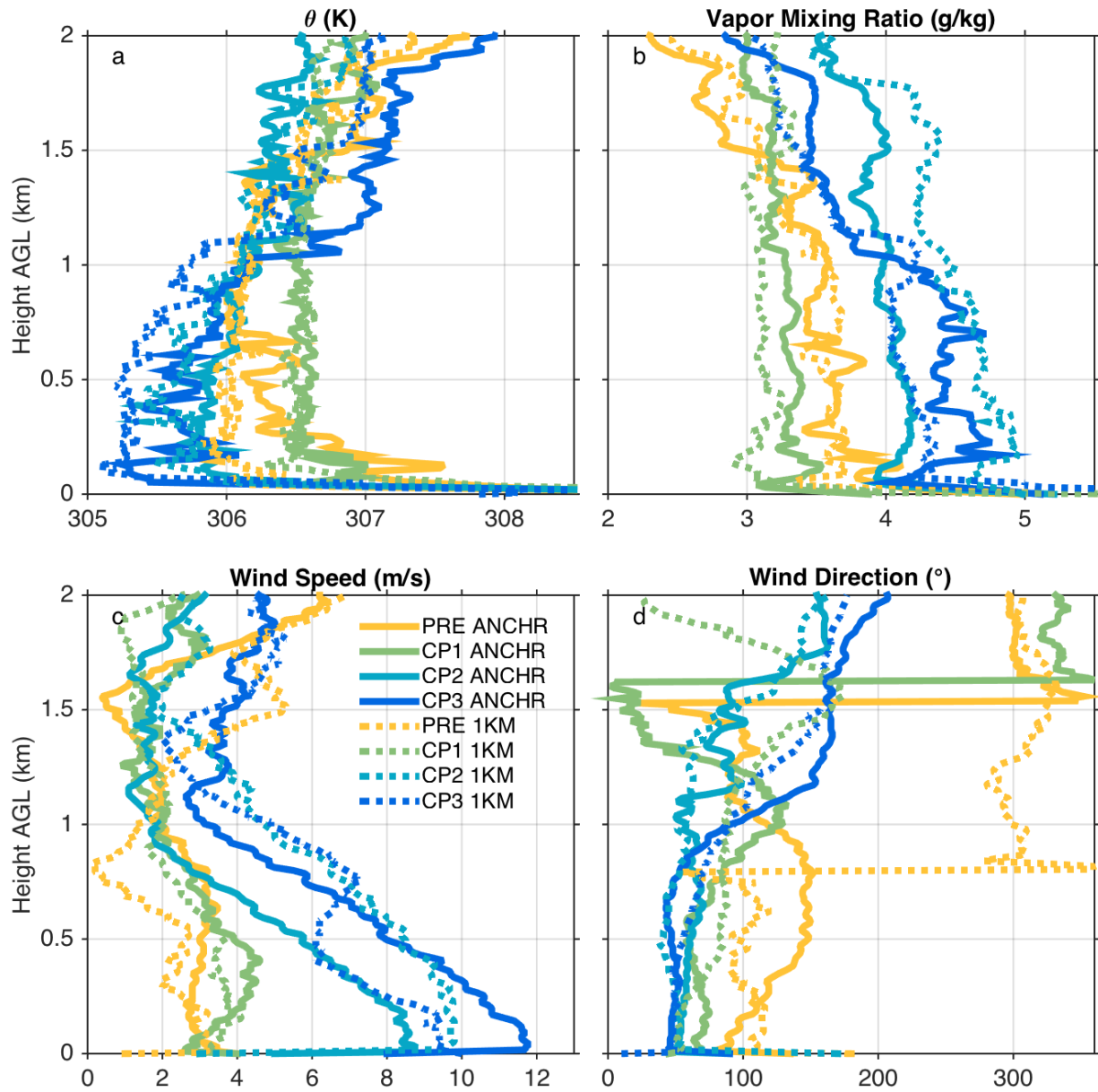
Figure 4.3. Sounding data from the 4 sets of soundings as indicated in the legend in panel c. Sounding data are processed by the InterMet software, which includes temporal smoothing and radiation corrections for temperature.
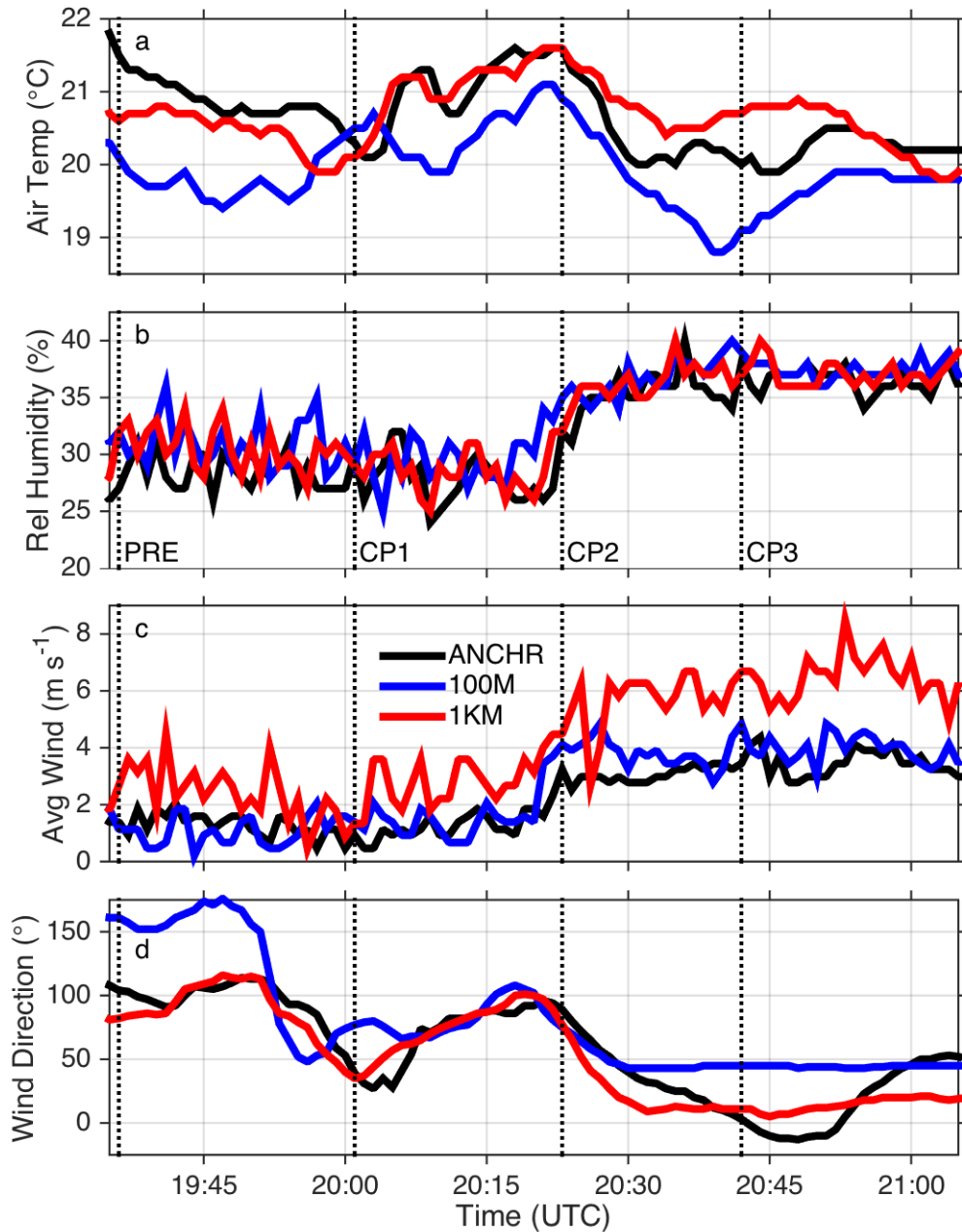
Figure 4.4. Time series of near-surface quantities from the three portable surface stations at the three different deployment locations as indicated in the legend in panel (c). All quantities are 1-minute running averages from 1-second data samples, which is the finest averaged output interval available. Dashed vertical lines indicate the times of the four pairs of sounding launches as labeled in panel (b).

CHAPTER 5: THE ROLE OF COLD POOLS IN TROPICAL OCEANIC CONVECTIVE SYSTEMS

5.1. Introduction

Despite the importance of organized tropical convective systems to the global circulation (Riehl and Malkus 1958) and to the state of the tropical atmosphere including the tropical rainfall budget (Nesbitt et al. 2000, 2006; Tan et al. 2013), the dynamics of organized tropical convective systems have received less attention compared with that of midlatitude systems. Numerous papers on midlatitude convection have highlighted the important role of cold pools in linearly organized systems via RKW theory (Rotunno et al. 1988; Weisman and Rotunno 2004). This theory postulates that the circulation on the downshear side of the cold pool, which behaves as a density current, and the wind shear in the inflow environment interact to influence the convective system structure (e.g. its tilt), intensity, and control its maintenance. Rotunno et al. (1988) state, "We argue that these results describe the physics of both midlatitude and tropical squall lines."

Studies of tropical convective systems have often utilized idealized simulations, typically over an ocean surface. Some studies have focused on feedbacks between radiative heating, surface fluxes, and cloud cover (e.g. Held et al. 1993; Bretherton et al. 2005; Stephens et al. 2008) and the importance of cold pools (Tompkins 2001; Jeevanjee and Romps 2013; Muller and Bony 2015) in organizing convection, while others have demonstrated the influence of gravity waves on convective initiation and clustering (e.g. Mapes 1993; Lac et al. 2002; Tulich and Mapes 2008; Lane and Zhang 2011). Several authors who evaluated tropical squall lines in the context of RKW theory found qualitative agreement (e.g. Nicholls et al. 1988; Keenan and Carbone 1992; Robe and Emanuel 2001). Recently, however, Lane and Moncrieff (2015;

hereafter LM15) and Moncrieff and Lane (2015; hereafter ML15) investigated the morphology of two types of convective systems in sheared tropical oceanic environments whose behavior did not conform to that expected from RKW theory. LM15 investigated an "upshear-propagating regime." In those systems, it appeared that the cold pool defined the system's propagation speed but that the cold pool was coupled to a ducted gravity wave, such that the region of preferred convective initiation was on the upshear side of the cold pool. In ML15, the vertical wind shear was marginally weaker than in LM15 and the convective systems propagated downshear. The weak cold pools in this "downshear-propagating regime" did not appear to control the propagation of the convective systems.

As the discussion above suggests, it is unclear exactly how important cold pools are to the organization of tropical convection and to tropical convective system behavior in different environments. The goal of our study is therefore to investigate the role of cold pools in tropical convective systems. We address the question, *how do cold pools influence tropical convective system evolution and characteristics such as intensity, mesoscale structure, and propagation mechanisms*? Based on our prior knowledge of cold pools and their demonstrated importance for convective initiation (e.g. Tompkins 2001) and maintenance (e.g. LM15) in the tropics, we hypothesized that if we were to weaken or remove the cold pools, the convective systems should be weaker and would propagate more slowly. We tested our hypothesis using idealized simulations (described in section 5.2) and, as demonstrated in section 5.3, we were wrong on both counts. Instead, we show that the weakening of the cold pools acts to intensify the organized systems (section 5.3a) and has little influence on the systems' propagation and longevity (section 5.3b); we then explore physical explanations for these results (sections 5.3c and 5.3d).

5.2. Description of simulations

a. RCE-BASE simulation

To address our hypothesis and investigate the role of cold pools in tropical convective systems, we ran idealized simulations using the Regional Atmospheric Modeling System (RAMS) version 6.1.18 (Cotton et al. 2003; Saleeby and van den Heever 2013). RAMS has been successfully used to investigate tropical convection in a number of prior studies (e.g. Stephens et al. 2004, 2008; Posselt et al. 2008; Storer and van den Heever 2013) and is therefore a useful tool for this work. We used the radiative convective equilibrium (RCE) framework, which is an idealized approximation to the state of the tropical maritime atmosphere (Manabe and Strickler 1964; Tompkins and Craig 1998). Linearly-oriented convective systems, which are commonly observed over tropical oceans (Liu and Zipser 2013), emerge spontaneously in large-domain channel RCE simulations (e.g. Held et al. 1993; Grabowski and Moncrieff 2001). Our approach was to examine two different convective systems embedded within the initial simulation's domain (hereafter called RCE-BASE); these systems occurred about 20 days into the simulation when the environment in RCE-BASE was approaching its equilibrium state.

The RCE-BASE simulation domain was a long channel with dimensions 3000 km × 200 km × 25 km, 1 km horizontal grid spacing, and 75 stretched vertical levels with vertical grid spacing that varied from 70 m near the surface to 500 m aloft. The main time step was 5 s. Lateral boundary conditions were periodic, a Rayleigh damping layer was included in the topmost 4 km, and the lower boundary was an ocean surface with 300 K sea surface temperature. Surface-atmosphere energy and momentum exchanges were calculated using bulk formulas following Louis (1979) with the minimum wind speed increased to 7 m s^{-1} so that the domain-averaged surface latent and sensible heat fluxes were comparable to observed tropical oceanic

values of order 100 W m^{-2} and 10 W m^{-2}, respectively. Other physical parameterizations used in RAMS include the Harrington (1997) two-stream radiation scheme updated every 5 simulation minutes; an anisotropic Smagorinsky (1963) turbulence scheme with stability modifications by Hill (1974) and diffusion coefficients calculated for perturbation fields; and a two-moment bulk microphysics scheme with 3 liquid (cloud, drizzle, rain) and 5 ice (pristine ice, snow, aggregates, graupel, hail) categories, and bin-emulating procedures for droplet nucleation, riming, and sedimentation (Meyers et al. 1997; Saleeby and Cotton 2004, 2008). The shape parameter in the gamma distribution was set to 4 for cloud and drizzle and 2 for all other species. Aerosols were initialized horizontally homogeneously with an exponentially decreasing profile that had a surface concentration of 100 mg^{-1} and a scale height of 7 km. Aerosols were given a solubility of 90% for droplet nucleation and could nucleate ice following DeMott et al. (2010). Sources and sinks of aerosol number were not included, and aerosols were not radiatively active.

The 00 UTC 5 December 1992 TOGA COARE sounding was used as the initial thermodynamic profile but with zero wind throughout the atmosphere, as in Stephens et al. (2004). Random temperature perturbations of maximum amplitude 0.1 K were introduced over the lowest 500 m AGL to initialize boundary layer inhomogeneity. Following prior RCE studies, the diurnal cycle was excluded by employing a constant solar zenith angle of 50° and the solar constant was changed to 695.41 W m^{-2}, which resulted in a top of atmosphere insolation of 447 W m^{-2}, the tropical atmosphere annual mean (Posselt et al. 2012). Deep convection developed after several days due to atmospheric destabilization by radiative cooling and surface fluxes.

By day 20, there are multiple moist and dry bands within the channel domain, a common characteristic of channel RCE simulations (e.g. Stephens et al. 2008). Envelopes of organized convection pulse within each moist band (Figure 5.1). We selected and simulated two convective

systems from RCE-BASE at higher resolution (section 5.2b) starting at day 20, following a one-way nesting approach similar to McGee and van den Heever (2014). At day 20 the simulation has not yet reached an equilibrium state, but the domain-averaged precipitation rate is 3.4 mm day^{-1}, domain-averaged precipitable water is 41 mm, and maximum updraft speeds are 15-25 m s^{-1}, all of which are realistic for tropical oceanic observations (Stephens 1990; Heymsfield et al. 2010; Adler et al. 2012).

b. Cluster and linear systems and sensitivity experiments

The two convective systems identified from RCE-BASE (Figure 5.1), a cluster system and a linear system, are simulated at higher resolution. These two systems differ in several respects, which are demonstrated later but summarized here. One system's convective cells are organized in a cluster-like manner while the other is linearly organized, as suggested by their respective names. Another difference is their propagation direction: the cluster system propagates in the negative x-direction as it intensifies (and then switches propagation direction as it decays), while the linear system propagates in the positive x-direction. Additionally, the linear system is shorter lived but more intense than the cluster system. By simulating two convective systems with different characteristics, we can assess whether the role of cold pools is robust across different organizational types.

Two nested control simulations were performed, hereafter called CTL-CLST (Control-Cluster) and CTL-LIN (Control-Linear). Both CTL simulations used 250 m horizontal grid spacing, 30 m (near-surface) vertical grid spacing stretched to 250 m aloft, and a 2.5 s time step. The finer grid spacings permit better representation of the turbulence and cold pool characteristics (Bryan et al. 2003; Grant and van den Heever 2016). Both CTL runs extended 500

km in the zonal (x-) direction to capture the entire moist band that each system lives within, and 200 km in the meridional (y-) direction to match that of the RCE-BASE simulation, giving a total of $2000 \times 797 \times 128$ grid points for each domain. The meridional lateral boundary conditions were kept periodic, but the zonal boundary conditions were changed to open radiative (Klemp and Wilhelmson 1978) and nudged with the RAMS output from the RCE-BASE simulation using a nudging time scale of 15 min. Each CTL simulation was initialized from the day 20 instantaneous RCE-BASE fields interpolated onto the higher resolution grid. The only difference between the two CTL simulations was their x-position in the RCE-BASE run and the length of integration time. CTL-CLST was initialized from x = 550 km to x = 1050 km in RCE-BASE and run for 36 hours, as shown by the left box in Figure 5.1, while CTL-LIN was initialized from x = 2350 km to x = 2850 km and run for 21 hours (right box in Figure 5.1). In each case, the total run time captures the intensifying through dissipating stage of the system. Model output was stored every 10 minutes. From here on, "hour 0" of the higher resolution simulations will refer to the initialization time, corresponding to day 20 of RCE-BASE.

To investigate the role of cold pools in the tropical convective systems, we altered the cold pool strengths by changing hydrometeor evaporation rates below cloud base[11] (~330 m AGL, where the second derivative of the domain- and time-mean cloud water mixing ratio profile is maximized in the CTL simulations, i.e., where there is the most curvature in the mean

---

[11]In the RAMS microphysics, condensation and evaporation are calculated by one routine that simultaneously updates water vapor mixing ratio, hydrometeor mixing ratios and internal energies, and air temperature following the analytical formulas of Walko et al. (2000b). Evaporation rates were therefore modified as follows: first, the condensation/evaporation code was allowed to run as normal, and grid points below cloud base that underwent evaporation were flagged. For these grid points, condensation/evaporation was re-calculated with a modified value of water vapor diffusivity. This method alters both the mass transfer of water between vapor and condensed phases and the associated latent heating, and it also allows hydrometeor mixing ratios and internal energies, water vapor mixing ratio, and air temperature to remain self-consistent.

cloud water profile). Similar cold pool modification methods have been used in several previous studies (e.g. Crook and Moncrieff 1988; Jeevanjee and Romps 2013), although most, if not all, prior studies modify evaporation over a greater depth than just the subcloud layer. We modified evaporation only below cloud base in order to avoid altering other aspects of the convection (such as entrainment rates and gravity waves), thereby complicating the interpretation of the cold pools' roles. Sensitivity experiments were conducted with the modified evaporation rates by restarting the CTL simulation at hour 5 for the cluster system and hour 3 for the linear system, both of which are 5 hours before the main analysis period (hours 10-20 for the cluster system and hours 8-16 for the linear system, when the propagation speed is well defined; see section 5.3b). Two of the sensitivity experiments were called EOFF-CLST and EOFF-LIN, where EOFF stands for "Evaporation off." In these tests, evaporation below cloud base was shut off completely by setting water vapor diffusivity to 0.[11] This is the most we can weaken the cold pools without also changing evaporation above cloud base.

Because the cluster system showed a larger response in the EOFF experiment than did the linear system (as shown in the next section), two additional sensitivity experiments were also performed for the cluster system: E1/2-CLST, in which water vapor diffusivity was reduced by a factor of 5, resulting in evaporation rates that are approximately halved; and E2X-CLST, in which water vapor diffusivity was increased by a factor of 5, resulting in an approximate doubling of evaporation rates and stronger cold pools. In summary, six high-resolution simulations were performed: CTL-CLST, EOFF-CLST, E1/2-CLST, E2X-CLST, CTL-LIN, and EOFF-LIN. E2X-CLST is the only sensitivity test in which cold pools were strengthened; in all other sensitivity tests, the cold pools were weakened.

5.3. Results

a. Convection intensity

Our method to weaken the cold pools by preventing evaporation only below cloud base is effective, especially in the cluster system, despite the shallow depth of the sub-cloud layer (Figure 5.2). The method is effective because the origin of most downdraft air in weakly sheared tropical maritime systems is close to cloud base (e.g. Moncrieff and Miller 1976; Torri and Kuang 2016a), which we confirmed via PDFs of moist static energy (not shown). The signature of many of the small, individual cold pools ahead of the main system have disappeared in the density potential temperature (θ_ρ, Emmanuel 1994) fields in the EOFF simulations (e.g. Figure 5.2a,c from x = 50 – 150 km, and Figure 5.2e,g from x = 280 – 350 km), suggesting those small cold pools in CTL are largely created by evaporation in the sub-cloud layer. The average near-surface θ_ρ' values (relative to the domain-mean θ_ρ of each high resolution grid) in the regions of strongest cold pools reach -0.55 K in CTL-CLST and -1.5 K in CTL-LIN but only reach -0.05 K in EOFF-CLST and -0.85 K in EOFF-LIN.

If cold pools are initiating and/or helping to maintain convection in the two systems, we would expect the convective systems to be weaker in the EOFF simulations than in the CTL simulations, as hypothesized. However, the OLR fields in Figure 5.2 suggest that the opposite may be true. In the cluster system, low OLR regions cover more area in EOFF than in CTL, indicating wider coverage of cold cloud tops (Figure 5.2b,d). In the linear system, differences between the OLR fields are subtle, though individual convective elements appear slightly wider with colder cloud tops in EOFF (Figure 5.2f,h).

The surprising result that convection is more intense in EOFF than in CTL suggested by the snapshots in Figure 5.2 is corroborated by analysis of multiple measures of convective

intensity. One such measure is mean precipitation rate, which is noticeably greater in EOFF compared to CTL, particularly when the precipitation rate is intensifying or decaying (Figure 5.3a). The corresponding domain- and time-mean precipitation rate (and therefore also to total accumulated precipitation) increases by 7-17% in the EOFF simulations (Table 5.1). The precipitation rate probability distributions in the four CTL and EOFF simulations (Figure 5.4) tell a similar story as the average precipitation rates. For instance, the frequency of occurrence of moderate, 40-80 mm hr^{-1} precipitation rates increases by about 25% in EOFF for the linear system and by 50-500% for the cluster system (Figure 5.4b).

Precipitation is not a perfect measure of convective intensity for these experiments because when sub-cloud evaporation is reduced, more water will reach the surface as precipitation, all else equal. However, the precipitation differences between CTL and EOFF are also associated with changes in OLR, and therefore in cloud top temperatures (Figure 5.3b). OLR is lower on average in the EOFF simulations than in the corresponding CTL simulations, indicating colder cloud tops associated with more intense and/or more widespread deep convection. Such OLR differences suggest that the precipitation increase in the EOFF simulations is due to increased convective vigor and not due solely to the reduced sub-cloud evaporation.

The two additional sensitivity tests for cluster system (E1/2 and E2X) follow the same trend as the EOFF simulations (Figure 5.3 and Table 5.1): precipitation increases in E1/2 when cold pools are weakened by the reduced evaporation rates, as in EOFF, while precipitation decreases in E2X when cold pools are strengthened by faster evaporation rates; OLR changes accordingly. However, the magnitude of the difference is much smaller in E1/2 (E2X) than in EOFF, despite the ½ (2) factor change in evaporation rate, all else being equal. However, not all

else is equal: when cold pools are weakened by slower evaporation rates in E1/2, the cold pools become warmer and drier and therefore have lower relative humidity, which acts to increase the evaporation rates again, thereby resulting in a negative feedback on the initial decrease in evaporation rate. The negative feedback similarly exists in E2X, and it acts to keep the E1/2 and E2X cold pool properties and system intensity similar to those of the CTL run. The feedback does not exist in the EOFF simulations since the evaporation cannot respond to changes in relative humidity in EOFF. This result may indicate that, in reality, cold pools in the tropics may be fairly insensitive to factors such as drop size distributions or surface fluxes that could otherwise perturb cold pool strengths. Given the small changes in E1/2 and E2X compared to CTL, the remaining analysis will focus only on the CTL and EOFF simulations.

The final measure of convective intensity we examine here is updraft strength. The fastest updraft speeds are between 15 and 25 m^{-1} for both systems (Figure 5.5a,c), which is in the range of observations for tropical oceanic convection (Heymsfield et al. 2010; Varble et al. 2014; Schumacher et al. 2015). In the cluster system, EOFF has up to 1 m s^{-1} stronger vertical velocities above 4 km AGL (Figure 5.5b), and between 6 and 8 km AGL, the relative increase in updraft speed in EOFF compared to CTL exceeds 20% for the 90-99 percentiles. EOFF-LIN also has stronger mid- and upper-troposphere updraft speeds than CTL-LIN, although the magnitude of the differences is slightly smaller (Figure 5.5d). The increases in updraft speed for both EOFF cases are consistent with the increase in precipitation and reduction in OLR, and suggest an overall increase in the mesoscale upward circulation. However, interesting trends appear for the strongest updraft speeds over the lowest 4 km, which are presumably associated with the initiation of a small number of intense, convective-scale updrafts by cold pools. For the cluster system, the strongest updrafts are weaker in the EOFF case below 2 km AGL (for the 97.5

percentile) and below 4 km AGL (for the 99.9 percentile). However, for the linear system, the updrafts are stronger at all depths in the EOFF case, except between 3 and 6 km AGL where they are weaker for the 99.9th percentile. These differences between the two systems are presumably related to the differences in low-level inflow to the two systems and their convective-scale initiation, which is discussed further in section 5.3b.

In summary, we have analyzed various metrics for convective intensity and have shown that when cold pools are weakened, the convection becomes more intense. We theorize that cold pool air becomes incorporated into the updrafts, and its initial negative buoyancy reduces the convective intensity. This idea is explored further in section 5.3c. These results suggest that the cold pools are not playing critical roles in convective initiation, and that mechanisms other than cold pools are more important for initiating and maintaining convection, such as gravity waves (e.g. Balaji and Clark 1988; Lane and Reeder 2001; Lac et al. 2002).

b. *Propagation and mesoscale structure*

Given the large differences seen in the cold pools themselves and in the convective intensity, it is natural to next ask, are the propagation speeds different and/or is the mesoscale structure altered in the EOFF simulations? If the cold pools define the propagation speed of the systems (e.g., as in LM15), then we would expect to find slower propagation in the EOFF simulations than in the CTL simulations, as we originally hypothesized. Additionally, if RKW theory is applicable to these tropical systems, then differences in the mesoscale structure (e.g. system tilt) and maintenance should arise due to the weakened cold pools.

We can answer whether the cold pools are playing a role in the propagation speeds by examining Hovmöller diagrams of condensed water path (Figure 5.6). The cluster system slowly

propagates in the negative x-direction at about 1 m s^{-1} between hours 10-20, when the propagation speed is clearly defined (Figure 5.6a), while the linear system propagates more quickly in the positive x-direction at about 6 m s^{-1} (Figure 5.6c). Despite the fact that the EOFF simulations have weaker cold pools, we see by comparing the slopes of the black and red contour overlays in Figure 5.6 that the propagation speeds are not distinguishably different between CTL and EOFF for either system. The lifetimes of both systems and the time at which the cluster system switches propagation direction are also not affected by the changes to the cold pools. *We therefore conclude that the cold pools do not play the dominant role in determining propagation speeds, nor do they significantly impact the lifetimes and evolution of the systems.*

To determine whether the cold pools influence the mesoscale flow patterns and structure of the systems, we compare composite cross sections for CTL and EOFF, beginning first with the cluster system[12]. We define the system-relative streamlines in the same way as LM15. Several notable features of the CTL-CLST structure are apparent in Figure 5.7a,c. The full-troposphere view of the streamlines shows several flow branches: front-to-rear jump updrafts originating primarily at three different levels (near the surface, 4 km, and 7.5 km AGL); an overturning circulation above 9 km AGL (between x = -150 km and -50 km); and a low-level ascending and overturning circulation at the back of the system (between x = -25 km and 150 km). A mesoscale downdraft does not exist, similar to the system studied in ML15. The low-level shear ahead of (to the left of) the cluster system is negative (Figure 5.9a), so it propagates downshear but tilts upshear.

---

[12] Despite the cluster-like appearance of this system in the θ_ρ and OLR fields, the predominant flow is zonal and fairly meridionally symmetric (see Figure 5.2) due to the channel configuration and cyclic boundary conditions of the RCE-BASE run, which justifies a simple meridional averaging method.

The composite cold pool in CTL-CLST has a minimum θ'_ρ of -0.55 K and a theoretical propagation speed[13] of 3 m s^{-1}. In EOFF, the minimum θ'_ρ is only -0.05 K and the theoretical speed is reduced to 1 m s^{-1}. Despite these substantial cold pool changes, the general mesoscale structure is unchanged in EOFF compared to CTL. There are only small differences in the streamlines, such as a stronger upper level overturning circulation in EOFF and slightly steeper streamlines in CTL at low levels above the leading edge of the composite cold pool. The steeper low-level streamlines result in a sharper horizontal gradient of condensate mixing ratios (Figure 5.7c). These structures are consistent with some convective-scale initiation by the cold pool near the surface and the larger values of the most intense low-level updrafts in CTL-CLST compared to EOFF-CLST (Figure 5.5b). In CTL, low-level ascending streamlines originating within the sub-cloud layer pass through the composite cold pool and falling precipitation (Figure 5.7c). This indicates that, from the viewpoint of the mesoscale flow, the low-level inflow to the CTL-CLST system acquires negative buoyancy through evaporative cooling in the sub-cloud layer, which lends support to the hypothesis that the evaporation that forms cold pools is actually having a detrimental effect on the intensity of convection by reducing the buoyancy of the inflow air.

The linear system exhibits many similar mesoscale features to the cluster system (Figure 5.8). For instance, the system has ascending front-to-rear flow and a jump updraft since the streamlines end up at a higher altitude than they originated, and the system lacks a mesoscale downdraft. The low-level shear ahead of (to the right of) the system is positive (Figure 5.9b), so it also propagates downshear and tilts upshear, as in the cluster system. The composite cold pool

---

[13] Theoretical cold pool propagation speed, C, is calculated as $C^2 = 2 \int_0^H -Bdz$ (Benjamin 1968) where H is the top of the cold pool taken to be 500 m AGL (see Figure 5.7 and Figure 5.8), and $B = g\frac{\theta'_\rho}{\theta_\rho}$ is the buoyancy.

in CTL-LIN is stronger than in CTL-CLST: its minimum θ_ρ' is -1.5 K and theoretical speed is 5.7

m s^{-1}. In EOFF-LIN, the minimum θ_ρ' has been reduced by nearly half and the theoretical speed

is 12% lower. Thus, despite the changes in the cold pool structure from CTL-LIN to EOFF-LIN,

both cold pools' theoretical speeds are similar. Both CTL-LIN and EOFF-LIN do show small

regions of stagnation within the composite cold pool (indicated by the circular streamline), and

the horizontal maps (Figure 5.2) show a well-defined leading edge and system-relative flow

toward the front of the cold pool, as might be expected in association with the presence of a

density current. However, there are nearly indistinguishable changes in mesoscale structure

between CTL and EOFF, which indicates that the mesoscale behavior of these systems is not

overly sensitive to the details of the cold pool. Yet, as shown earlier, the EOFF case has stronger

updrafts throughout the depth of the convection and more intense precipitation.

The increase in intensity of the linear system with weaker cold pools can be explained by

two important changes in the composite structure of the system. First, the weakening of the cold

pool in EOFF-LIN places the system in a more optimal state, according to RKW theory, since Δu

over the lowest 2 km is less than 2 m s^{-1} (Figure 5.9b) and hence $\frac{c}{\Delta u}$ is closer to 1. Indeed, as

expected, the streamlines in Figure 5.8d are slightly steeper than in Figure 5.8c. Second, the

leading precipitation and evaporation in CTL-LIN produces a cold pool that protrudes about 25

km ahead of EOFF-LIN's cold pool. As in the cluster system, the low-level inflow passes

through this protruding cold pool in CTL-LIN. This flow pattern bears some resemblance to the

midlatitude, front-fed, leading stratiform convective systems simulated by Parker and Johnson

(2004a), except that here, the leading precipitation is not stratiform in nature nor advected from

the convective region, but rather is formed by congestus clouds ahead of the main convective

line (e.g. see Figure 5.2). The inflow through the composite cold pool, along with the

evaporation of the leading precipitation, reduces the buoyancy of the inflow. Hence the low-level inflow in EOFF-LIN does not experience the detrimental effects of the protruding cold pool and evaporation as in CTL-LIN, and the system is more intense as a result.

With the exception of the small region of stagnation in the cold pool, the linear system is strictly propagating, i.e., streamlines pass through the system from right to left at all levels, and there is no evidence of a mesoscale downdraft. The system appears to propagate in a wave-like manner, which is also consistent with the cold pools' weak influence on the mesoscale features. Perhaps most importantly, both CTL-LIN and EOFF-LIN have nearly identical propagation speeds, regardless of cold pool strength. Thus, despite some features of the linear system being consistent with RKW theory, the overall behavior of the linear system and its structure suggests that some other mechanism is responsible for the system propagation and longevity.

c. The role of cold pools in convective intensity

We theorize based on the results of section 5.3a that the presence of the cold pools weakens convective intensity through the impacts of negative buoyancy in the sub-cloud layer, implying that some the rising updraft air originates from within the cold pools. While at first this feels counter-intuitive, prior studies have suggested that updrafts do transport some air from the cold pools (e.g. Tompkins 2001; Torri et al. 2015). We investigated how much cold pool air is transported aloft by the updrafts in these two convective systems through additional experiments in which passive tracers were initialized within the CTL and EOFF cold pools. Eighteen different tracers were initialized at the middle of the analysis periods when precipitation differences are large (hour 15 for the cluster systems and at hour 12 for the linear systems) and were integrated for two hours. The tracer initialization regions, which are visually summarized for the two CTL

systems in Figure 5.10(a-d), were determined as follows. Tracers 1-9 were initialized in regions where $\theta_\rho' \leq -0.5\ K$ and tracers 10-18 were initialized where $\theta_\rho' \leq -1\ K$, thereby allowing us to evaluate whether the amount of air that is transported by updrafts depends on the initial negative buoyancy. The tracers were given an initial mixing ratio of 1 kg kg^{-1} and were initialized at one of the nine lowest vertical model levels, all of which are below cloud base. Tracers 1 ($\theta_\rho' \leq -0.5\ K$) and 10 ($\theta_\rho' \leq -1\ K$) were placed closest to the surface (15m AGL), followed by tracers 2 and 11 in the next vertical model level and so on. Tracers 9 and 18 are the highest tracers (308m AGL) and are hence initialized closest to cloud base.

The percent of each tracer's total mass that has been transported above 3 km AGL after 2 hours is shown in Figure 5.10(e,f). The 3 km level resides above the tops of boundary layer cumuli, and so tracers transported above this altitude must have been carried there by congestus or deep convective updrafts. Over 21% of the near-surface cold pool air in the cluster system and up to 17% in the linear system ends up above 3 km (tracers 1 and 2). Additionally, it is evident from Figure 5.10(e,f) that more of the upward-transported cold pool air originates near the surface (tracers 1-3 and 10-12) than higher in the sub-cloud layer (tracers 7-9 and 16-18), although this altitude dependency is weaker in the EOFF simulations. One exception to this is tracers 17 and 18 in CTL-CLST, but those tracers cover a very small area of the domain. It is worth noting that none of the system-relative streamlines that pass through the composite cold pool ascend above 3 km in either system (Figure 5.7c and Figure 5.8c), which highlights the importance of considering the 3D structure of the cold pools and their behavior on convective scales. In the cluster system, the relative amount of upward-transported cold pool tracers is smaller in EOFF than in CTL (Figure 5.10e). The EOFF-CLST tracers' initial distributions are shifted farther back in the system compared to CTL, and they are therefore less likely to ascend

99

in convective updrafts given the mesoscale flow structure (Figure 5.7). On the other hand, in the linear system, the relative amount of upward-transported cold pool air is greater in EOFF than in CTL except for the near-surface tracers (Figure 5.10f). There are fewer tracers initialized toward the back of the system in EOFF-LIN (e.g. between x=200-240 km; see Figure 5.10b,d and Figure 5.2e,g), which may explain this result.

The tracer results lend support to our hypothesis that cold pools suppress convection intensity through their negative buoyancy, since a significant fraction of cold pool air is transported aloft. Several other studies have suggested similar findings [that the convection becomes more intense when cold pools are suppressed or weakened] both for tropical and for midlatitude systems. Liu and Moncrieff (2017; hereafter LM17) studied an idealized, shear-parallel, Meiyu front tropical system and demonstrated substantial intensification of the system when evaporation of rain was switched off. In simulations of a midlatitude mesoscale convective system, Trier et al. (2011) found that the MCS became more intense during its postsunrise reorganization when latent cooling from evaporation was removed. Our results also bear some resemblance to Schumacher (2015)'s study of an idealized nocturnal MCS. He showed that slight increases in low-level moisture led to large precipitation increases, suggesting the system processed and transported near-surface air through the convective region despite the stable boundary layer. Finally, these results are broadly consistent with boundary-layer quasi-equilibrium theory (Raymond 1994, 1995), which postulates that downdrafts are responsible for reducing CAPE in the tropical boundary layer and extinguishing convection.

d. The role of gravity waves in system evolution

As we have shown that the mesoscale structure and propagation of the convective

systems are mostly unaffected by changes to the cold pools, what then does govern the

mesoscale features? We turn to gravity waves for the answer, which have been shown to be

important regulators of tropical convective system behavior in several prior studies (Mapes 1993;

Shige and Satomura 2001; Liu and Moncrieff 2004; Tulich and Mapes 2008; Lane and Zhang

2011). Figure 5.11a shows a Hovmöller diagram of θ' at 3 km AGL in the RCE-BASE

simulation. Various phase speeds are evident, but the most prominent signal propagates in the

positive x-direction at 15 m s^{-1}. We use linear theory for a fluid at rest which defines the gravity

wave propagation speed as $c_x = \frac{N}{m} = \frac{Z_{trop}N}{\pi n}$, where Z_{trop} is the troposphere depth (16 km), N is

the Brunt-Väisälä frequency (0.0096 s^{-1}, averaged temporally and spatially in the troposphere),

$\frac{2 \cdot Z_{trop}}{n}$ is the vertical wavelength, and n is an integer number of antinodes within the troposphere.

The phase speed of an $n=3$ wave is 16.2 m s^{-1}, which closely corresponds to the main wave

signal seen in Figure 5.11a. Evidence of the $n=3$ wave in the zonal wind field can also be seen

behind the convective systems in Figure 5.7a,b and Figure 5.8a,b and in the inflow θ' profile for

CTL-LIN (Figure 5.9b). The $n=3$ wave's half-vertical wavelength is 5.3 km, which is similar to

the altitude of the freezing level (4.76 km). As this wave travels around the model domain, its

horizontal wavelength is widened and its amplitude is reinforced by convective systems via

latent cooling from melting and evaporation below the freezing level, similarly to mechanisms

described in Tulich and Mapes (2008).

The negative low-level temperature anomalies associated with the $n=3$ wave pass by near

the time at which both the linear and the cluster systems are raining most intensely (indicated by

the black dots in Figure 5.11a) and when the cluster system begins to propagate in the positive

rather than negative x-direction. Several prior studies have highlighted the importance of the *n=3* wave in tropical convection initiation, organization, and behavior (e.g. Lane and Reeder 2001; Lane and Moncrieff 2008; Tulich and Mapes 2008; Lane and Zhang 2011). Specifically, the phase of the *n=3* wave that is characterized by low-level ascent and its associated cooling signal destabilizes the lower atmosphere and promotes convective development.

Since the high-resolution simulations utilize lateral boundary nudging from the RCE-BASE simulation, two-way interactions between the convective systems and the larger scale waves are not permitted. In order to ensure that boundary nudging did not unduly constrain the evolution of the two systems, we ran the same EOFF experiment for the RCE-BASE simulation, executed as a restart from RCE-BASE at day 20 and integrated for 36 hours (called EOFF-BASE hereafter). The domain- and time-averaged precipitation rate in the RCE-BASE simulation (called CTL-BASE hereafter) is 0.144 mm hr^{-1}. In the EOFF-BASE simulation, the mean precipitation rate increases by 8.5% over CTL-BASE, confirming our precipitation rate results shown in section 5.3a. Additionally, the convective systems' propagation speeds do not change between CTL-BASE and EOFF-BASE (compare panels a and b in Figure 5.12), which indicates that the systems were indeed not overly constrained in the high-resolution simulations.

In a final experiment, we ran the RCE-BASE simulation with evaporation shut off everywhere below the freezing level (named EOFF-FL-BASE), which alters the forcing for the *n=3* wave and weakens its amplitude (Figure 5.11b-d). In EOFF-FL-BASE, the domain- and time-mean precipitation rate increases by 32.6% over CTL-BASE, a remarkable change and one that is consistent with that seen by LM17 in which evaporation of rain was shut off everywhere. The impact of preventing evaporation below the freezing level on the propagation of the systems is shown in Figure 5.12c. Dramatic changes in the propagation speeds are clearly evident. The

cluster system (around x=750 km) has stopped propagating entirely, and the linear system

(around x=2600 km) has slowed by about a factor of 3. The substantial propagation change in

EOFF-FL-BASE, particularly for the linear system, appears to be related to the *n=3* wave itself.

Specifically, a slower-moving, -1 K amplitude cold signal embedded within the main *n=3* wave

begins to appear at around 10 h and x=2600 km in CTL-BASE and EOFF-BASE (Figure

5.11b,c), but this signal is absent in EOFF-FL-BASE (Figure 5.11d). Note that this signal is not

due to cold pools, since *θ'* is shown at 3 km and the cold pools are only 500 m deep. The absence

of this signal in EOFF-FL-BASE coincides with the beginning of the significant changes in

propagation speed (Figure 5.12c) and suggests that the *n=3* wave may be convectively coupled

to the linear system and modulates its propagation speed in CTL-BASE and EOFF-BASE. The

weakening of the n=3 wave in the EOFF-FL-BASE simulation may bring its amplitude below a

critical threshold for the coupling to persist via destabilization.

5.4. Summary

RKW theory highlights the critical role of cold pools in linearly oriented convective

systems. This theory is widely accepted in midlatitude environments, and yet the authors

originally postulated that it should also be applicable to tropical convective systems. A few

studies have applied RKW thinking to tropical systems; some have found general agreement

with the theory, while others have not. In this study, we have investigated the role of cold pools

in influencing the intensity, mesoscale structure, propagation, and lifetime of two organized

tropical oceanic convective systems. We simulated two different systems in a low wind shear

environment, one being linearly oriented and the other organized in a cluster, and then changed

the cold pools by altering evaporation in the sub-cloud layer. If RKW theory were applicable to

these tropical systems, we would expect to find changes in their intensity, mesoscale structure, and propagation speed with changes in the cold pools.

We first investigated the convective intensity response to the cold pools and found that the systems became more intense when the cold pools were weakened, in opposition to our original hypothesis. We attribute this result to the fact that the cold pool air became incorporated into the updrafts, which we verified by introducing passive tracers into the cold pools. The cold pools' negative buoyancy reduced the convective intensity on two different spatiotemporal scales: (a) on the scales of individual convective elements, the cold pool air was entrained into the updrafts; and (b) on the mesoscale, the low-level inflow air was evaporatively cooled from precipitating congestus clouds ahead of the primary convection. The detrimental influence of the cold pools on convective intensity via their negative buoyancy is in contrast to the prevailing thinking that cold pools enhance convection by playing critical roles in initiating new convection via cold pool collisions or their interaction with wind shear (RKW theory).

We also investigated whether our evaporation-induced changes to the cold pools influenced the mesoscale structure, propagation, or lifetimes of the convective systems. Although we saw changes in streamline tilt at low levels near the composite cold pools, neither the cluster nor the linear system exhibited differences in propagation speed, lifetime, or the broad mesoscale structure when the cold pools were altered. This suggests that their behavior cannot be explained by RKW theory. The lack of response in the linear system is particularly interesting because its tilt and structure was in keeping with RKW thinking and the system propagation speed closely matched that of the theoretical cold pool speed. We wonder whether prior studies that have successfully applied RKW theory to tropical convective systems would also find a similar lack of response in the mesoscale structure and propagation to changes in the cold pool strengths.

Since the cold pools did not impact the convective systems' mesoscale structure or propagation, the role of gravity waves in the convective system morphology was explored. We showed the importance of the *n=3* wave in influencing the intensity and system evolution, in accordance with prior studies. Additionally, it appeared that this wave may be coupled to the convective systems and therefore controlled their propagation speeds. The coupling appeared to cease once the wave amplitude was artificially suppressed by removing all cooling below the freezing level. The influence of the amplitude of the n=3 (and other) wave modes on their ability to couple to convection should be a topic of future research.

Our cluster and linear system results, the upshear-propagating regime (UPR) in LM15, the downshear-propagating regime (DPR) in ML15, and the shear-parallel, Meiyu front tropical system in LM17 have interesting similarities. Commonalities in structure and flow include the wave-like propagation with through-flow at all levels (linear, UPR, and Meiyu system); the tilt back over the cold pool (cluster, linear, UPR, and Meiyu system); and the lack of a mesoscale downdraft (cluster, linear, and DPR). RKW arguments do not appear to fully explain the behavior of any of these five systems, and in fact, the cold pools' inferred or demonstrated lack of importance to the propagation and structure is true for all but the UPR. However, a ducted gravity wave was also shown to be important in the UPR, and we speculate as to whether the UPR's propagation would be altered if the cold pool were eliminated. The common lack of influence of cold pools on the mesoscale features, despite the different shear strengths and orientations, suggests an important underlying cause for these similarities and their departure from midlatitude system behavior other than shear. That cause may simply be the moist boundary layer and resulting weak and shallow cold pools, which was the underlying hypothesis in LM15 and ML15.

It would be interesting to explore whether our results hold in other environments, such as tropical continental regimes. We also suggest further mechanistic studies of the role of waves in the behavior and organization of tropical convection, both from modeling and observational perspectives.

5.5. Tables and figures

Table 5.1. Domain- and time-averaged precipitation rate in the CTL simulations and percent differences from CTL for the sensitivity simulations, averaged over the duration of the sensitivity simulations (hours 5-36 for the cluster system and hours 3-21 for the linear system).

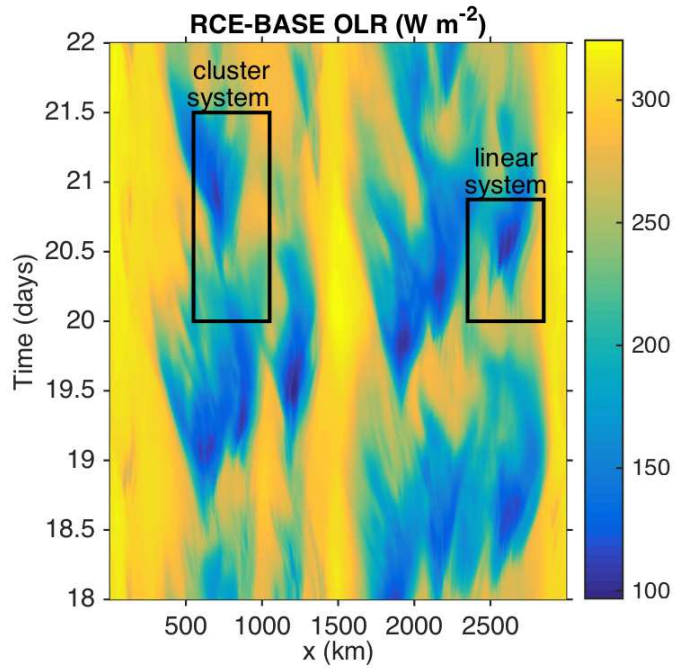| Simulation	Precipitation Rate
CTL-CLST	0.26 mm hr^{-1}
EOFF-CLST	+ 16.96 %
E1/2-CLST	+ 1.51 %
E2X-CLST	- 4.01 %
CTL-LIN	0.54 mm hr^{-1}
EOFF-LIN	+ 6.93 %

Figure 5.1. Hövmoller diagram of zonally averaged outgoing longwave radiation at model top (OLR) in simulation RCE-BASE. The black boxes show the zonal extents and durations of the cluster and linear system high-resolution simulations.
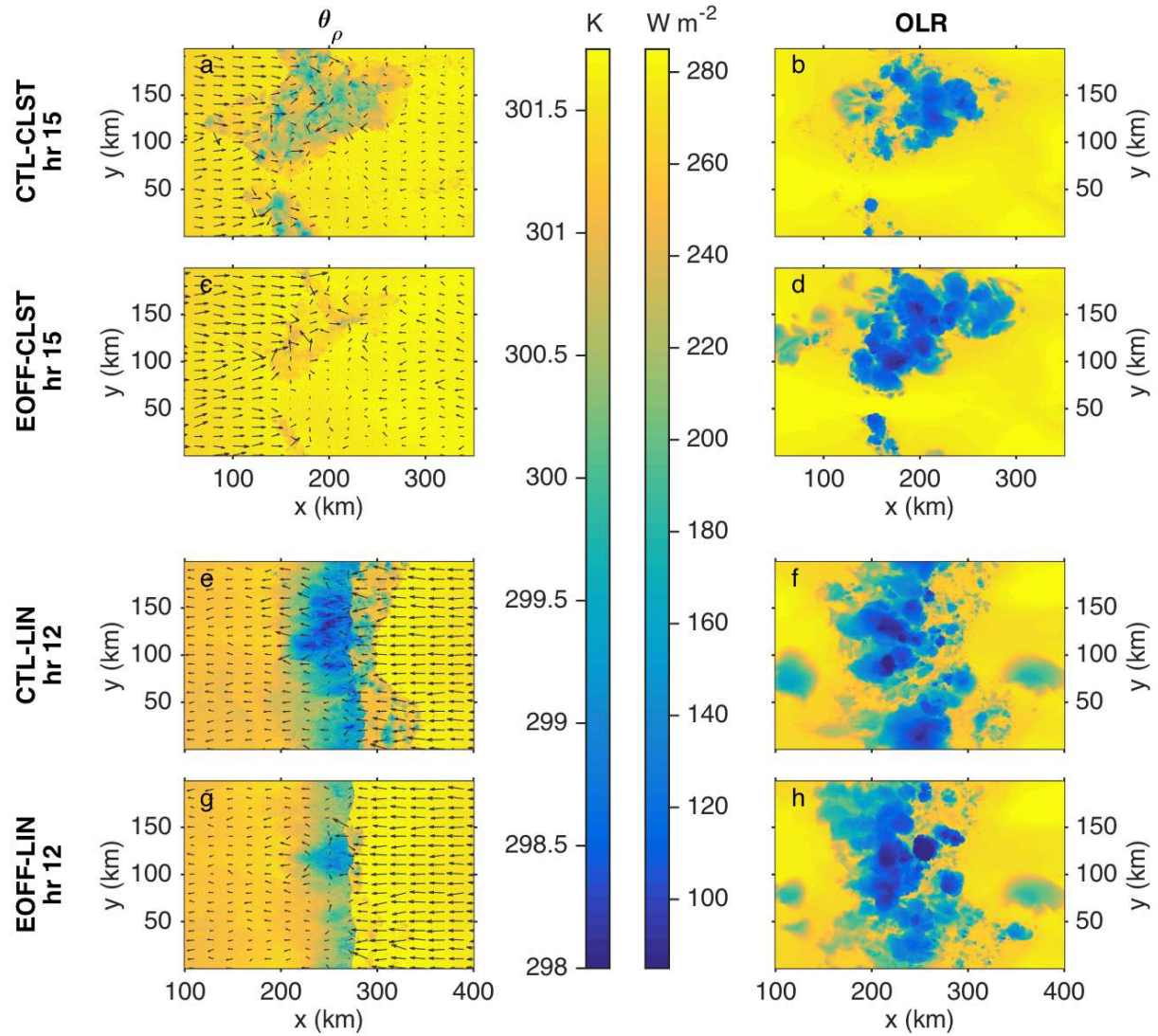
Figure 5.2. Instantaneous plan views of (a,c,e,g) density potential temperature (θ_ρ) and system-relative wind vectors (see section 5.3b for propagation speeds) at the lowest model level (15 m AGL); and (b,d,f,h) OLR. Simulations (a,b) CTL-CLST and (c,d) EOFF-CLST are shown at hour 15 of the high resolution simulations, and simulations (e,f) CTL-LIN and (g,h) EOFF-LIN are shown at hour 12.
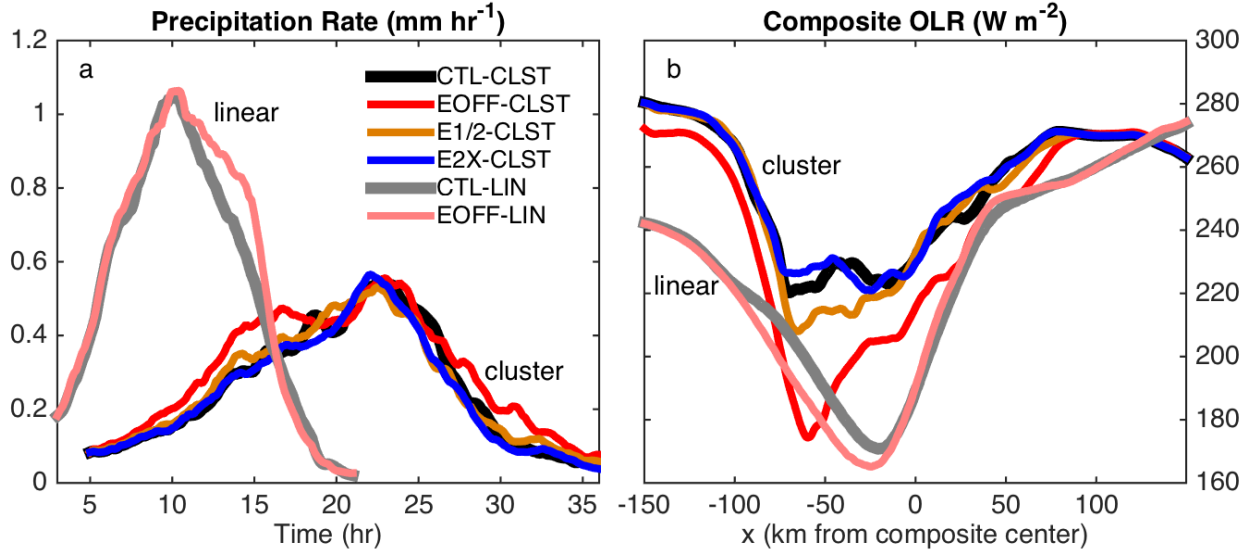
Figure 5.3. (a) Time series of domain-averaged precipitation rate for all six high-resolution simulations as shown in the legend. (b) Composite OLR for the same six simulations. Composites were created by following the system at its propagation speed (see section 5.3b) and averaging meridionally and temporally over hours 10-20 for the cluster system and hours 8-16 for the linear system.
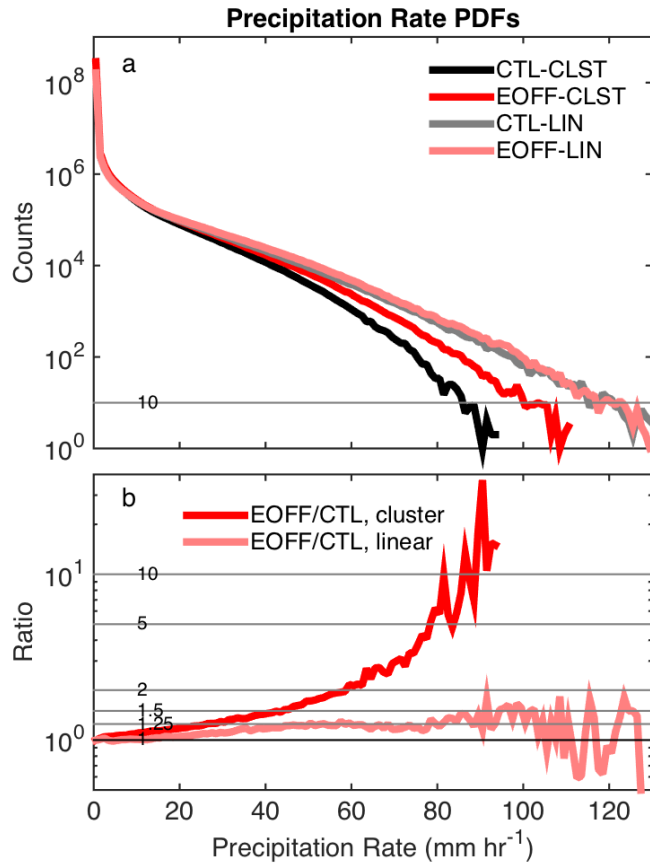
Figure 5.4. (a) Probability density functions (PDFs) of precipitation rate for both CTL and EOFF simulation sets as indicated in the legend. The precipitation rate bin width is 1 mm hr^{-1}. Counts are accumulated over hours 10-20 for the cluster system and hours 8-16 for the linear system. (b) Ratio of precipitation rate bin counts in EOFF to CTL.
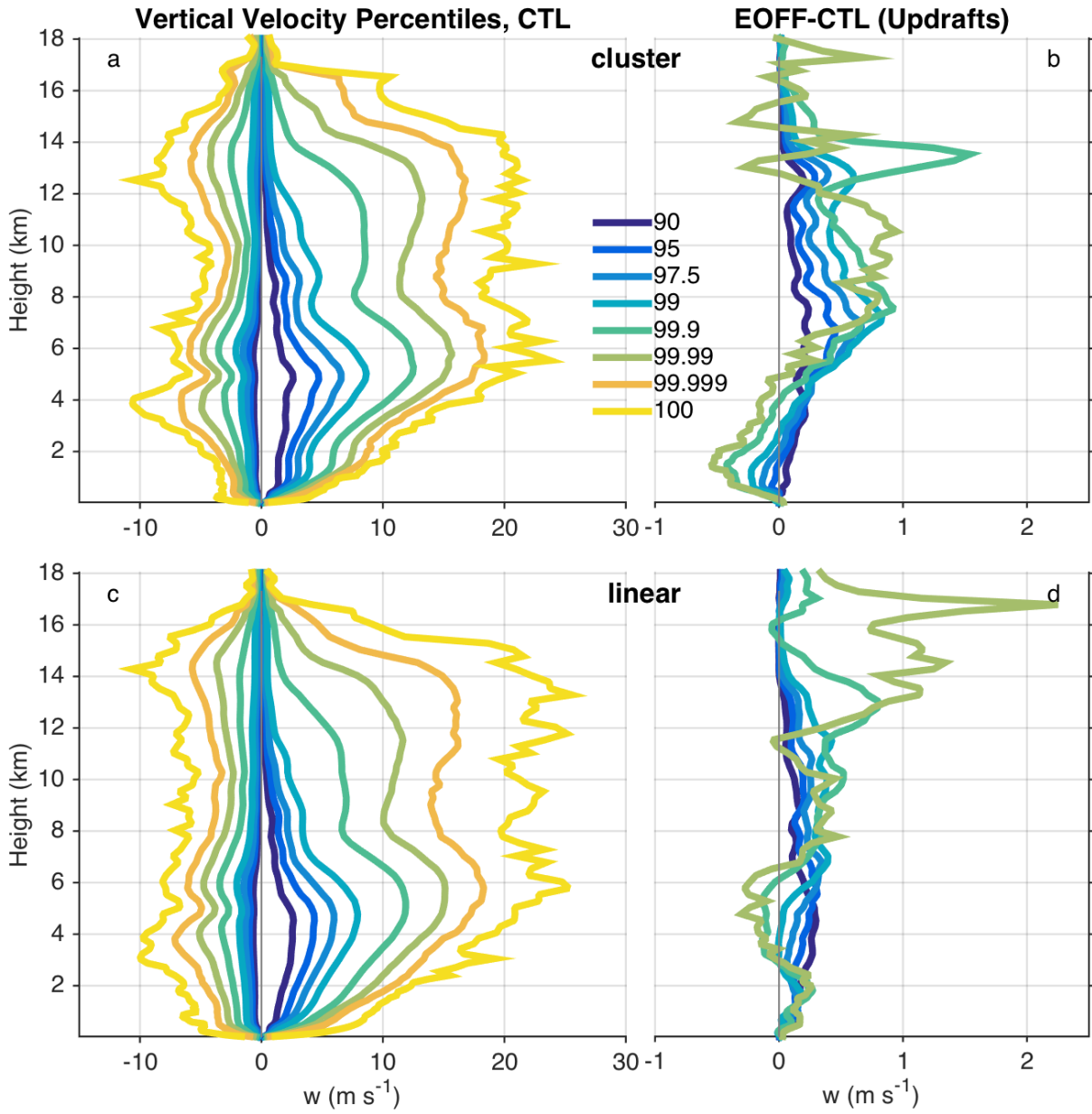
Figure 5.5. (a,c) Percentiles of vertical velocity for |w| ≥ 0.1 m s^{-1} as a function of height in (a) CTL-CLST over hours 10-20, and (c) CTL-LIN over hours 8-16. (b,d) Differences between EOFF and CTL for upward vertical velocity percentiles (w ≥ 0.1 m s^{-1}) in (b) the cluster system and (d) the linear system. The 99.999 and 100 percentile differences are not shown due to noise.
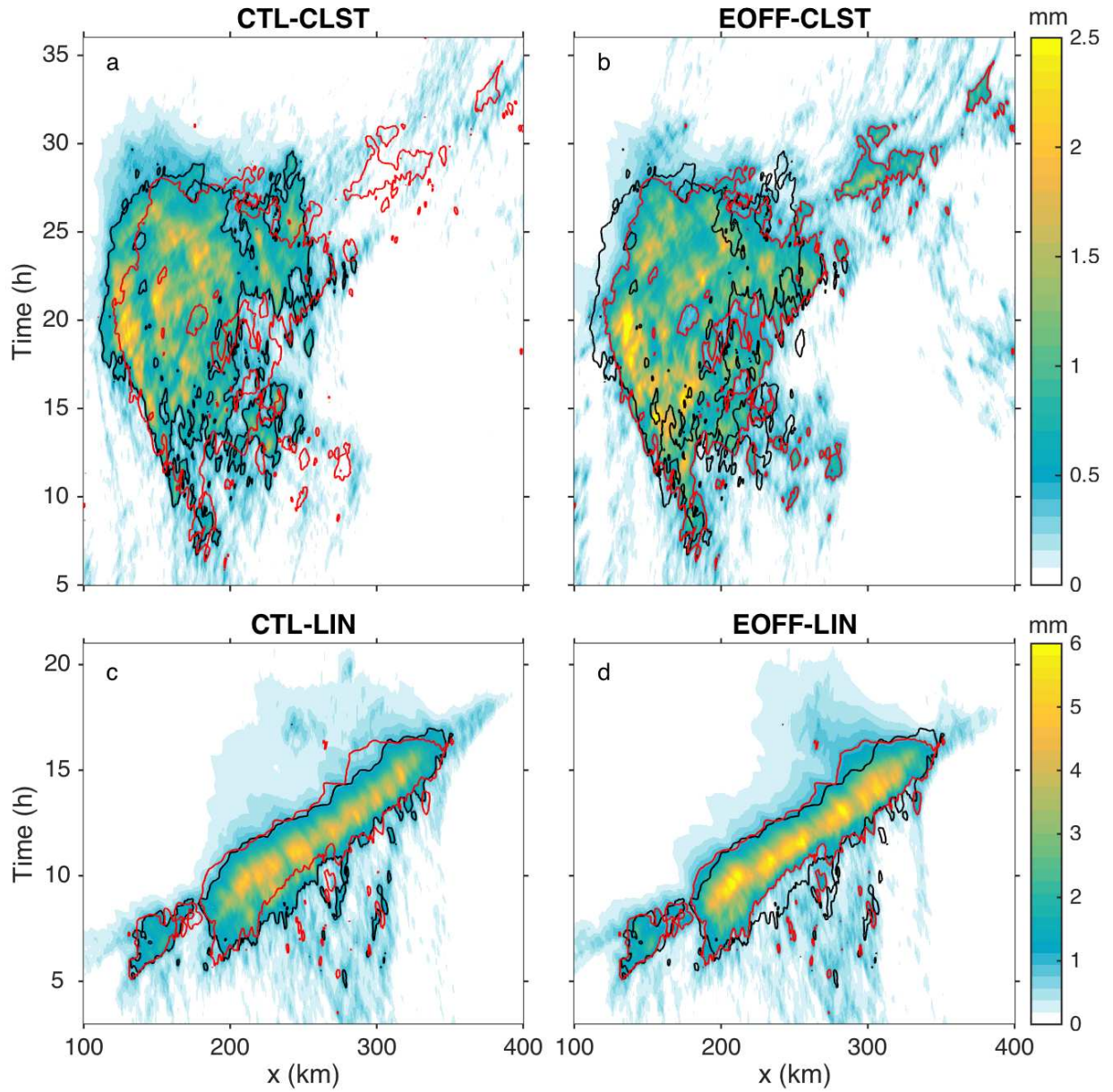
Figure 5.6. Hövmoller diagrams of meridionally averaged condensed water path (mm) in (a) CTL-CLST, (b), EOFF-CLST, (c) CTL-LIN, and (d) EOFF-LIN. To aid comparison, the 0.5 mm contour is shown in black for CTL-CLST and in red for EOFF-CLST in both panels (a) and (b), while the 1 mm contour is shown in black for CTL-LIN and in red for EOFF-LIN in both panels (c) and (d).
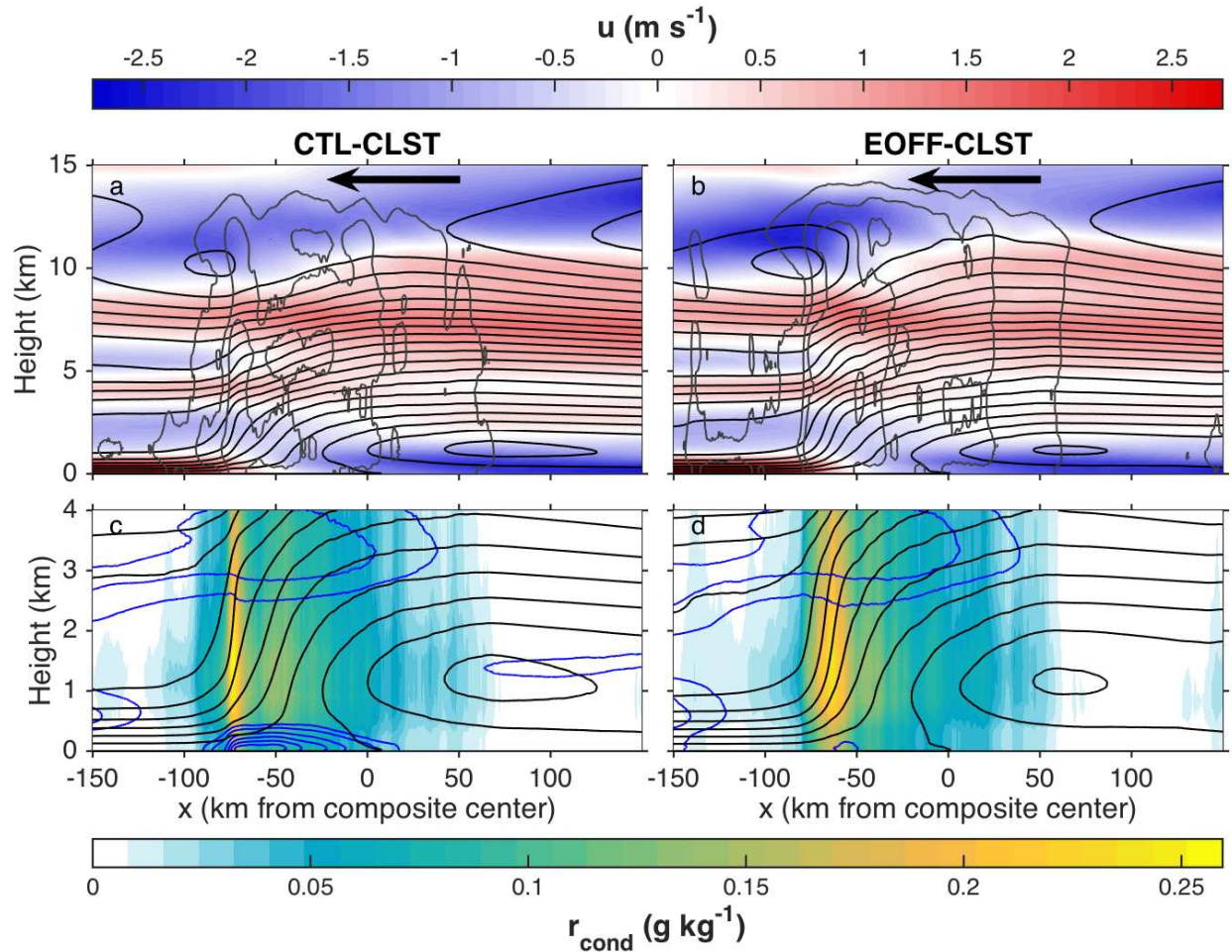
Figure 5.7. (a,b) Composite cross sections of zonal wind (shaded), total condensate mixing ratio (0.01, 0.05, 0.1, and 0.5 g kg^{-1} gray contours), and system-relative streamlines (black contours) calculated from the composite system-relative zonal wind. (c,d) Composite cross sections of total condensate mixing ratio (shaded), negative values of θ'_ρ, (blue contours every -0.1 K, plus -0.05 K), and system-relative streamlines (black contours), zoomed in on the lowest 4 km AGL. Composites were created by following each system at its propagation speed (-1 m s^{-1} for the cluster system) between hours 10-20 and then averaging meridionally and temporally. Note that streamlines flow from left to right at all levels, except between x = -25 km and x=150 km over the lowest 1 km AGL and above approximately 12 km AGL, where they flow right to left. The bold arrows indicate the propagation direction.
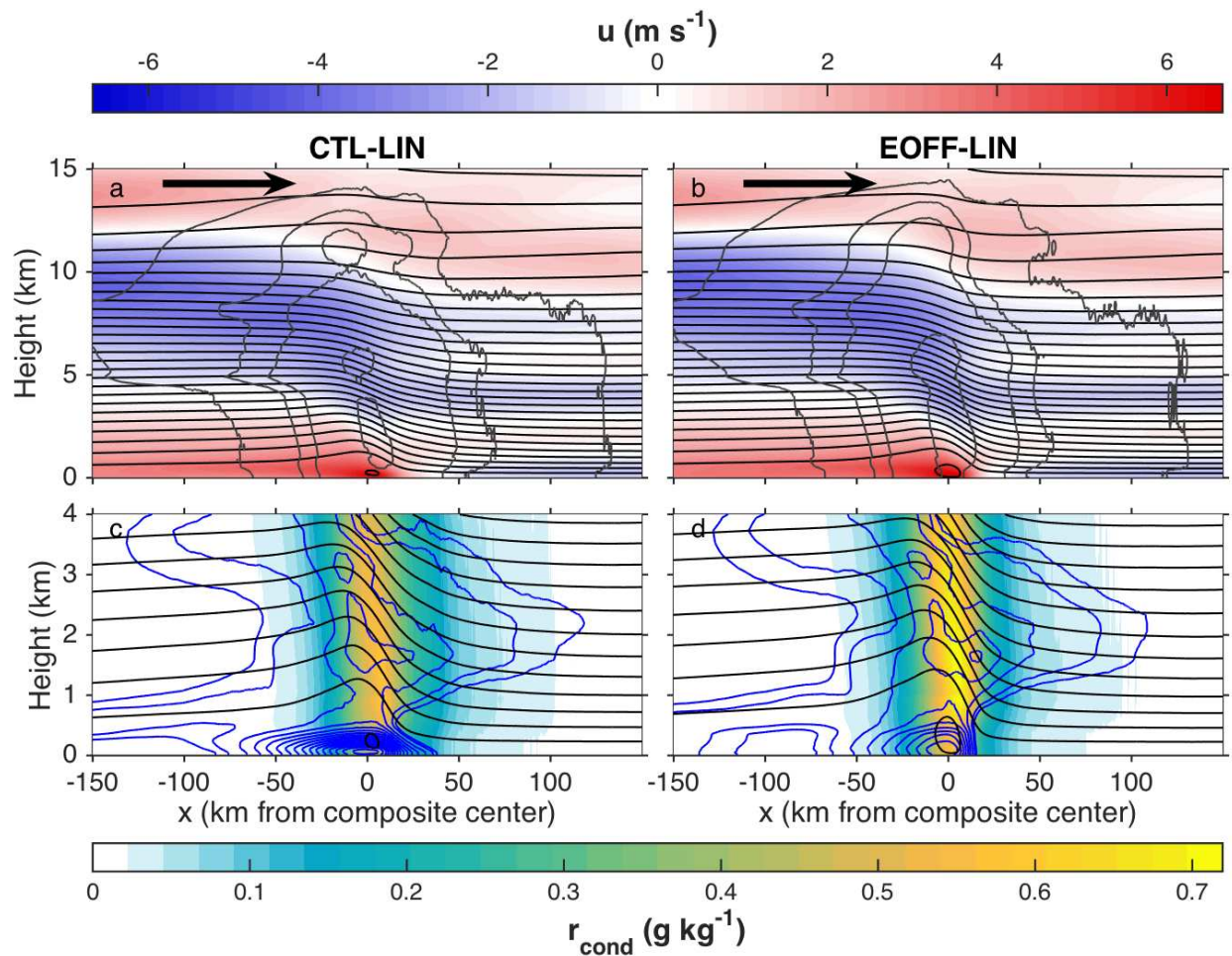
Figure 5.8. As in Figure 5.7, but for the linear system: for construction of the composites, each system was followed at its propagation speed of +6 m s^{-1} between hours 8-16. Note that streamlines flow from right to left at all levels. The bold arrows indicate the propagation direction.
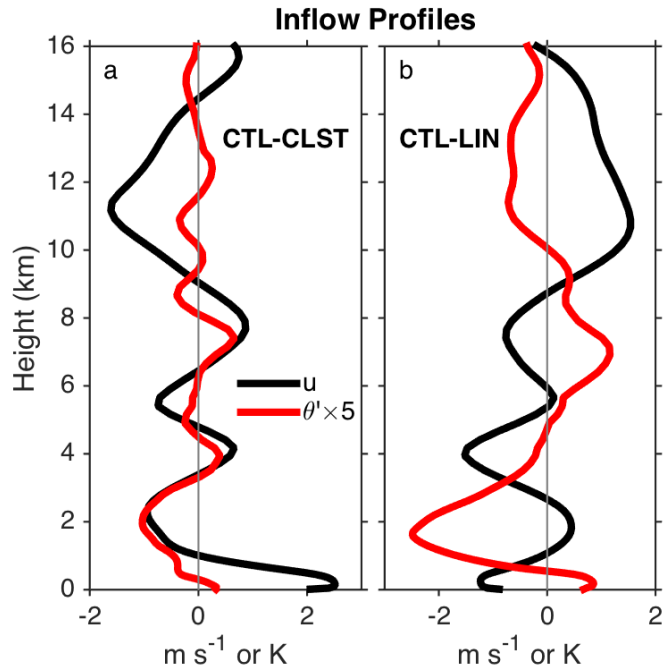
Figure 5.9. (a) Profiles of u and θ' (defined relative to the mean θ at each altitude) ahead of the CTL-CLST system, from x = -150 to x = -100 km in the composite framework. (b) As in (a), but for the CTL-LIN system, and averaged over a similar distance ahead of the composite cold pool as in the CTL-CLST system, from x = 50 to x = 100 km.
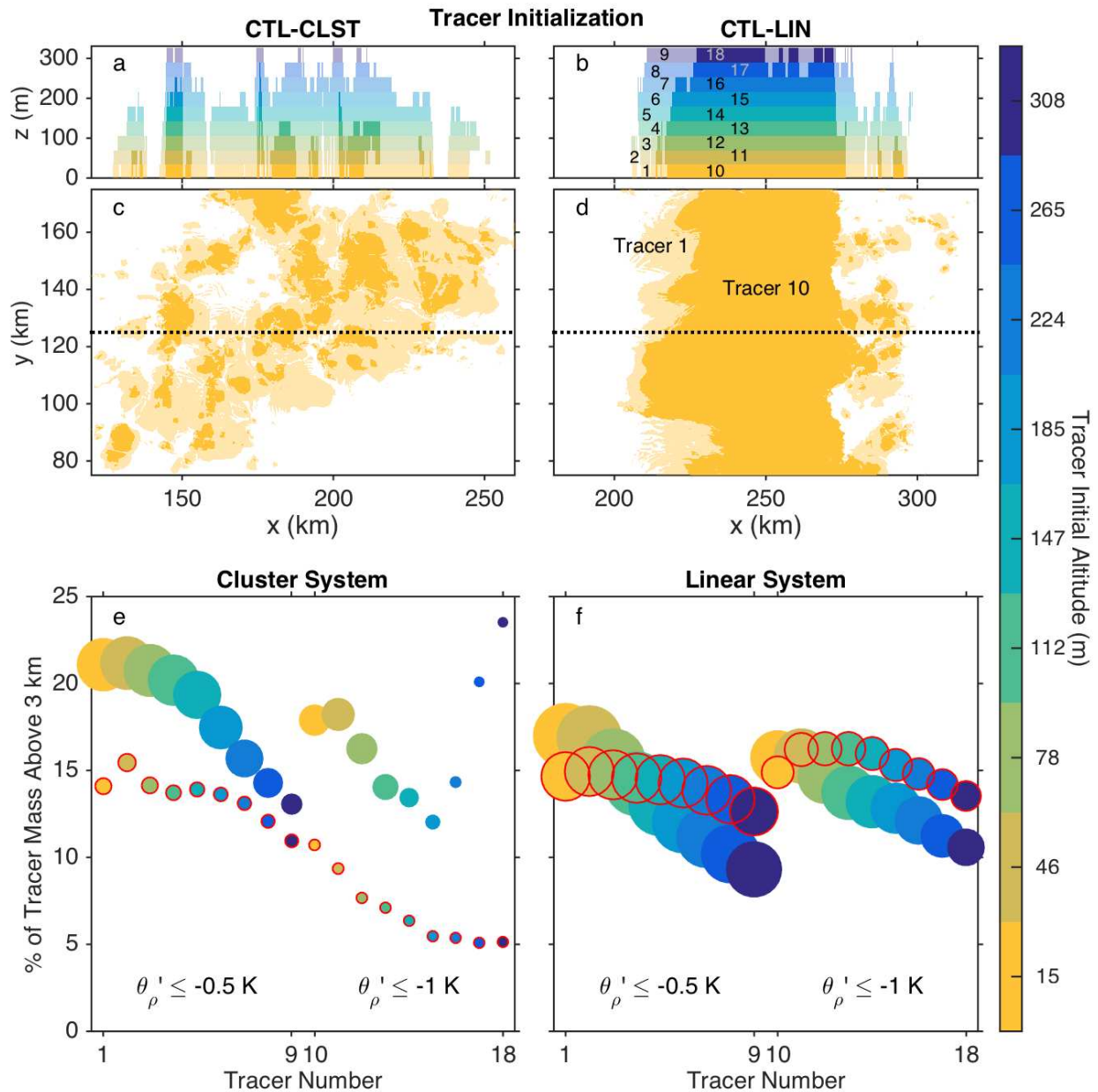
Figure 5.10. (a,b) Cross sections through y = 125 km and (c,d) zoomed-in plan views at 15 m, depicting tracer initialization regions in (left panels) the CTL-CLST system at hour 15 and (right panels) the CTL-LIN system at hour 12. Translucent (opaque) shading represents tracers 1-9 (10-18) initialized in regions where $\theta_\rho' < -0.5$ K ($\theta_\rho' < -1$ K), and the color indicates the tracer's initial altitude. Tracer numbers are labeled in (b) and (d). The dotted lines in the plan views indicate the cross section locations. (e,f) Fraction of each cold pool tracer's initial mass that is found above 3 km AGL after 2 simulation hours for (e) the cluster systems and (f) the linear systems. The CTL cases are shown by filled dots without an outline, and the EOFF cases are shown by red-outlined dots. The dot color indicates the tracer's initial altitude. The dot's size is proportional to the initial area percentage covered by each tracer. The largest dot represents 18.07% area coverage (CTL-LIN tracer 2) and the smallest 0.003% area coverage (CTL-CLST tracer 18).

117
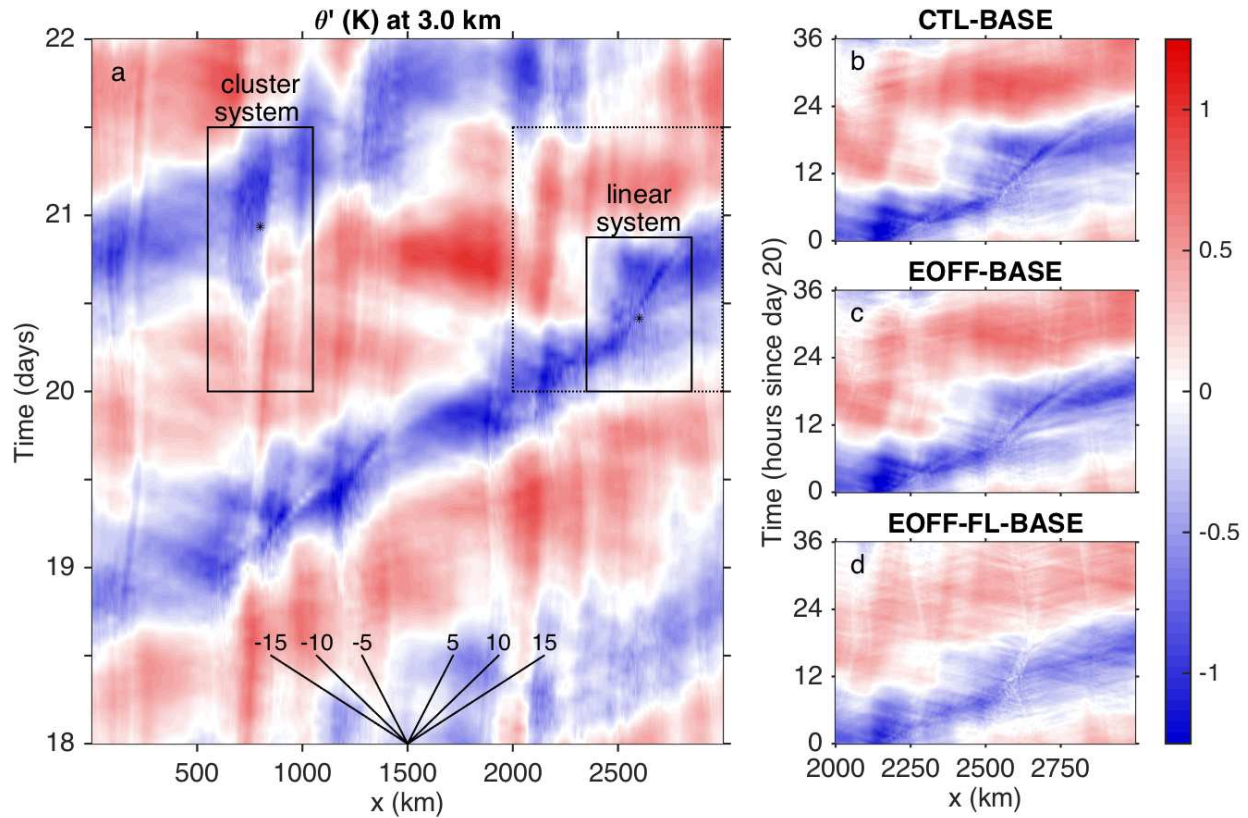
Figure 5.11. Hovmöller diagrams of θ' (relative to the domain mean) at 3 km AGL for (a) the RCE-BASE simulation and (b-d) the BASE simulation sensitivity tests, zoomed into the region of the linear system as outlined by the dotted box in (a). θ' is first meridionally averaged, and then the temporal average of each x column is removed. In (a), the cluster and linear systems are outlined as in Figure 5.1, and the dots represent the time of maximum intensity from Figure 5.3a. Black lines represent various phase speeds as labeled in the plot.
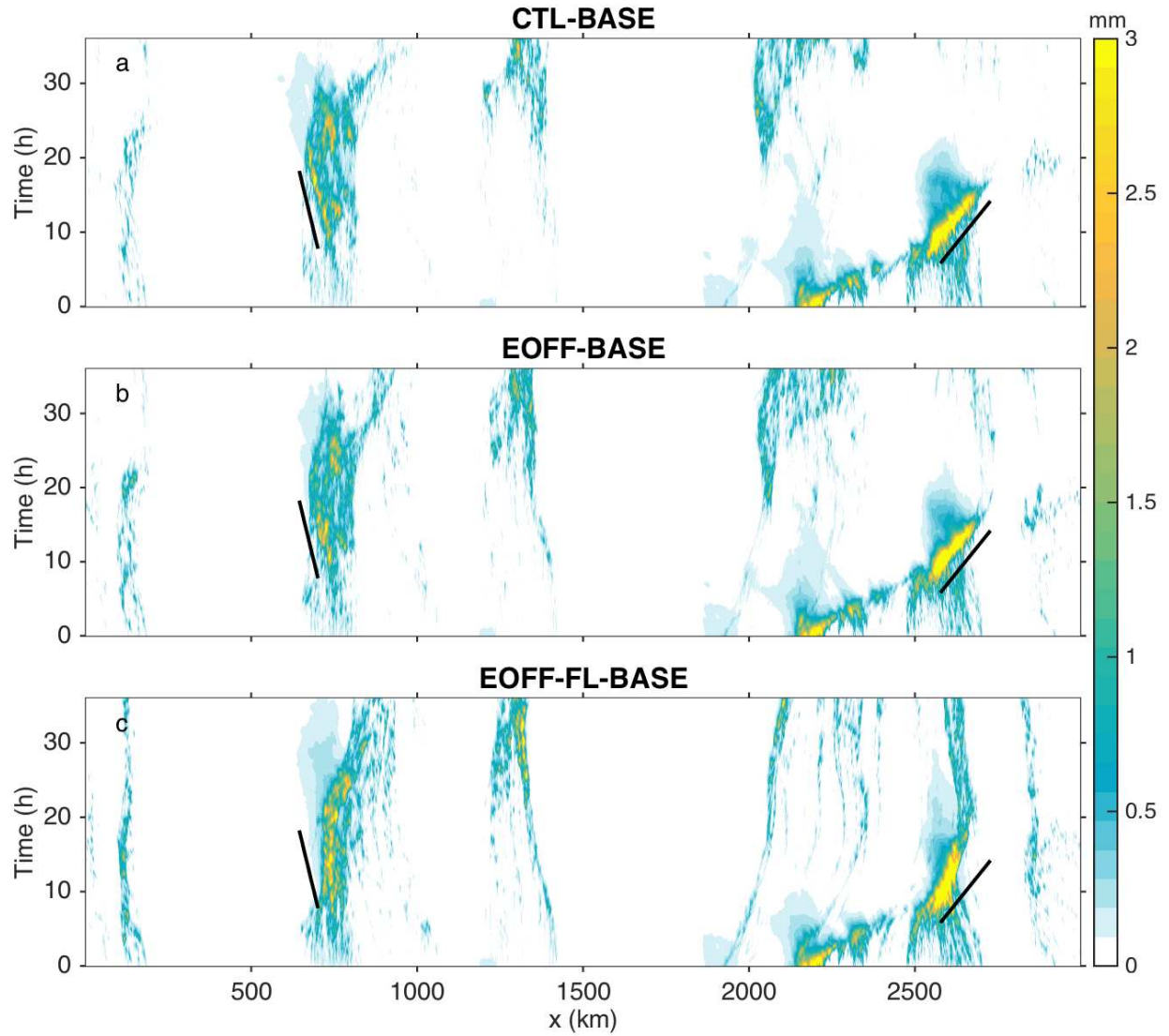
Figure 5.12. Hövmoller diagrams of meridionally averaged condensed water path (mm) in (a) CTL-BASE, (b) EOFF-BASE, and (c) EOFF-FL-BASE. The black lines are in the same location in each panel in order to distinguish differences in propagation speed among the simulations.

CHAPTER 6: CONCLUSIONS

6.1. Summary of studies

Although the basic dynamics of cold pools have been understood for decades, knowledge gaps still exist regarding the process-scale behavior of cold pool interactions with different components of the Earth system, including interactions with Earth's surface and with the individual convective storms or organized storm systems that produce the cold pools. It is important to narrow these knowledge gaps because cold pools exert significant influences on processes impacting weather and climate such as convective initiation, convective organization and propagation, lofting of constituents from the surface, the surface energy budget, and regional climatology. The overarching goal of the research presented in this dissertation has been to improve our process-level understanding of cold pools in different environments. Two specific knowledge gaps were addressed: (1) the interaction of cold pools with the land surface in semi-arid environments; and (2) the interaction of cold pools with organized convective systems in tropical oceanic environments. These knowledge gaps were addressed using both idealized simulations and observations.

The goal of the first study (Chapter 2) was to understand the main mechanism by which sensible heat fluxes (SHFs) impact cold pool dissipation in environments representative of dry continental regions. Two mechanisms were investigated: (1) SHF-induced enhancements in turbulent mixing between cold pool and environmental air, and (2) direct surface heating. This goal was addressed using a suite of idealized, two-dimensional simulations of isolated cold pools. The environment was neutral and calm with no water vapor, and therefore no interactions with convection, in order to isolate the most relevant physical processes to the specific goal.

Different SHF formulations were utilized in order to test the relative importance of mixing and surface heating. The simulation results demonstrated that the SHF effects on turbulent mixing between the cold pool air and the environmental air were larger than the direct heating effects, at least when the SHFs were representative of peak daytime values over a dry land surface. Prior work has discussed the direct surface heating and turbulent mixing aspects separately, but this study was the first effort to address their relative importance, particularly in dry environments in which cold pool – land surface interactions have thus far received little, if any, attention.

The second study (Chapter 3) focused on a different aspect of cold pool – land surface interactions in dry continental environments. The goal of this study was to understand how the land surface responds to the cold pool and to what extent this response influences the cold pool's subsequent evolution. Idealized 3D simulations of a cold pool both with an interactive land surface and with imposed homogeneous surface fluxes were conducted to address this goal. As in the first study, a simplified scenario was utilized including no representation of effects like cloud shading and precipitation influences on ground water and temperature, such that the basic interactions between the land surface and the cold, gusty air could be isolated. However, a turbulent boundary layer was included given the results from the first study regarding the importance of mixing to the cold pool's evolution. The simulation with the interactive land surface demonstrated that the sensible heat fluxes were always enhanced near the cold pool edge but suppressed near its center. This result was explained by the spatial pattern of land surface cooling, air temperature, and enhanced near-surface winds. By comparing the simulation with an interactive surface to the simulation with imposed fluxes, it was demonstrated that the surface – cold pool feedbacks exerted a strong control on the cold pool evolution. Specifically, the cold pool – land feedbacks significantly reduced the cold pool's spatial extent, propagation speed, and

lifetime. Finally, the surface feedbacks that led to enhanced SHFs near the cold pool edge also resulted in a locally more energetic boundary layer in comparison to the homogeneous fluxes case, with implications for convective initiation even after the cold pool's buoyancy anomaly had dissipated. To our knowledge, this study is the first to document surface flux responses to cold pools at high resolution over land and to explicitly demonstrate the substantial influence that cold pool – land surface interactions play in the evolution of both the cold pools and of the boundary layer.

In the third study (Chapter 4), a preliminary analysis of the 17 May 2017 ("The Bees Day") cold pool case observed during the C^3LOUD-Ex field campaign was discussed. The radar, sounding, and surface station data all demonstrated similarities between the observed cold pool case and the simulated continental cold pools, both in terms of the environment and the cold pool properties. The simulation results could therefore be utilized to assist in the interpretation of the case study data. The observational analysis indicated that the wind shift associated with the gust front's arrival occurred before the temperature drop was measured. Soundings taken after the wind shift was observed but before the temperature drop arrived demonstrated the presence of warmer and well-mixed air relative to the pre-cold pool soundings, such as seen in the simulations analyzed in Chapter 2. Additionally, persistent enhanced winds were seen within the cold pool despite a very weak cooling signal, similarly to the results of Chapter 3. The observations lent support to the conclusions drawn from the simulations, including the importance of mixing and land surface interactions in governing cold pool evolution.

Whereas the first three studies both aimed to address knowledge gaps in cold pool – land surface interactions, the goal of the fourth study (Chapter 5) was to assess the interaction between cold pools and organized convective systems in a tropical oceanic environment. This

goal was addressed using idealized simulations of organized systems that emerged in a simulation of tropical oceanic convection approaching a state of radiative-convective equilibrium. The role of the cold pools in the convective system intensity, mesoscale features, and propagation speed was investigated by altering sub-cloud evaporation rates and therefore the cold pool strengths. The results of the sensitivity tests demonstrated that in these tropical convective systems, the cold pools suppress convective intensity through their negative buoyancy due to the fact that cold pool air is incorporated into updrafts; in other words, the cold pools reduce the energy available to the convection through their negative buoyancy. It was also demonstrated that the cold pools play little to no role in the convective systems' propagation speeds, lifetime, and mesoscale structure. Large-scale gravity waves appear to be the important controls on the system propagation and lifetime. Although RKW theory highlights the important role of cold pools in convective system intensity and structure, its applicability to tropical convective systems was challenged based on these simulation results.

6.2. Implications of this research and future work

The research in this dissertation has advanced our understanding of cold pool – surface interactions and cold pool – convective system interactions, but it has also raised numerous new questions regarding process-scale behavior of cold pools that merit consideration for future research topics. Such questions include the following:

- How important is turbulent mixing to cold pool evolution in environments other than semi-arid continental regions?

- How do cold pool – land surface interactions vary for different surface types and in different environmental regimes?

- What role does land surface heterogeneity play in cold pool – land interactions?

- What is the importance of interactive sea surface temperatures in cold pool – ocean surface interactions?

- What processes govern cold pool moisture perturbations in different environments?

- What is the role of clouds and precipitation in regulating continental cold pool – surface interactions?

- Do cold pools play important roles in convective organization under tropical oceanic regimes with moderate to strong wind shear, or in tropical continental environments?

- What is the sensitivity of cold pool – surface – convection interactions to microphysical processes?

- How exactly do cold pools initiate convection?

Arguably one of the most important considerations arising from these studies is how our understanding of cold pool interactions with other components of the earth system may change as model resolutions and observations are conducted at continually finer resolutions. Future efforts should be devoted to advancing high-resolution modeling and observations because the influence of these smaller scales on the larger scales – even up through climate scales – is becoming increasingly widely recognized. This point was highlighted at a 2016 meeting in Berlin called "Understanding Clouds and Precipitation," part of the HD(CP)^2 (High Definition Clouds and Precipitation for advancing Climate Prediction) initiative (http://hdcp2.eu/). The cold pool – land surface numerical studies conducted for this research were both at LES scales, and these scales are becoming more feasible on large domains as computational power is continually increased. The influence of explicitly resolved large eddies and fine scale land surface

interactions on the properties and lifetimes of cold pools demonstrated here is also likely to be important to other aspects of cold pool behavior and its interactions with convection.

Can the results presented in this dissertation regarding cold pool – surface interactions in dry continental environments and cold pool – convective system interactions in tropical oceanic environments be combined with the knowledge from prior work on these two topics into a unified theory for cold pool – surface – convection interactions in different environments? If a unified theory does exist, it would significantly simplify and improve the parameterizations of cold pools and thereby the representation of their effects on convection and the climate in regional through climate scale models. Unfortunately, the results of these studies do not appear to help simplify the problem of parameterizing cold pools without switches to account for different factors in different environments. For instance, the apparent lack of importance of cold pools to the mesoscale structure and propagation in tropical convective systems demonstrated here differs from RKW theory at a physical process level. Moreover, these findings demonstrate the importance of including a land surface that can respond to and interact with the cold pool, but prior work suggests that only one-way influences of the ocean on the cold pools are necessary to consider given the ocean's large thermal inertia. Perhaps additional process-scale understanding of cold pool interactions will help to illuminate and inform the cold pool parameterization problem. For instance, how exactly cold pools initiate convection at a physical process level in both oceanic and continental environments is still not well understood, and the influence of ocean surface features like heated, fresh-water lenses from rainfall could potentially play a role in cold pool – ocean surface interactions.

While the C[3]LOUD-Ex observations will provide some insight into ground temperature responses to continental cold pools of varying strengths, observations of surface fluxes within

continental cold pools have yet to be documented and are critical in order to further our understanding of cold pool – surface interactions. Additionally, observations of cold pools in tropical oceanic and continental environments, and of cold pools associated with weak isolated convection as well as organized systems, are necessary to evaluate the ideas and hypotheses put forth in Chapter 5 regarding the role of cold pools in tropical convective systems. In particular, observational documentation of convective systems, their associated cold pools, and their environments are needed, particularly within a range of environmental wind shears and under the modulating influence of large-scale convectively coupled waves. Furthermore, since cold pools are intimately tied to cloud microphysical characteristics (particularly rain and ice species) of the parent convection, aerosol and microphysical measurements are also necessary to understand and evaluate cold pool – convection interactions.

An opportunity to acquire such measurements will take place in summer 2018 in the Maritime Continent region and the South China Sea during two cooperative field projects, the NASA-funded CAMP^{2}Ex (Cloud, Aerosol and Monsoon Processes Philippines Experiment; https://espo.nasa.gov/camp2ex) and the Office of Naval Research-funded PISTON (Propagation of Intra-Seasonal Tropical Oscillations; http://onrpiston.colostate.edu) campaigns. CAMP^{2}Ex will utilize the NASA P3 aircraft to characterize shallow through to deep convective clouds, collect in-situ observations of microphysical properties and aerosols, and conduct dropsonde launches to document thermodynamic and wind information in tropical convective environments, including within and outside of cold pools. PISTON will utilize a ship-borne polarimetric radar, SEA-POL, on board the *R/V Tommy Thompson* that can provide identification and documentation of cold pool boundaries along with radar-derived observations of rain rates and microphysical classifications. Sounding launches and surface flux measurements will also be

conducted from the research ship. These cooperative efforts will provide a rich and multi-faceted dataset containing information about isolated and organized tropical convection and their associated cold pools, cloud microphysical data, and the environmental meteorology including large-scale propagating features. Case study and idealized simulations in conjunction with analyses of the observational data are promising avenues in which new exciting insights into cold pool – surface – convection interactions in tropical continental and oceanic environments may be gained.

REFERENCES

Achtemeier, G. L., 1991: Observations of turbulent boundary-layer interaction with a thunderstorm outflow - A possible wake region energy source. *Boundary Layer Meteor.*, **55**, 309–324, doi:10.1007/BF00119807.

Adler, R. F., G. Gu, and G. J. Huffman, 2012: Estimating climatological bias errors for the Global Precipitation Climatology Project (GPCP). *J. Appl. Meteor. Climatol.*, **51**, 84–99, doi:10.1175/JAMC-D-11-052.1.

Aves, S., and R. H. Johnson, 2008: The diurnal cycle of convection over the northern South China Sea. *J. Meteor. Soc. Japan*, **86**, 919–934, doi:10.2151/jmsj.86.919.

Balaji, V., and T. L. Clark, 1988: Scale selection in locally forced convective fields and the initiation of deep cumulus. *J. Atmos. Sci.*, **45**, 3188–3211, doi:10.1175/1520-0469(1988)045<3188:SSILFC>2.0.CO;2.

Benjamin, T. B., 1968: Gravity currents and related phenomena. *J. Fluid Mech.*, **31**, 209–248, doi:10.1017/S0022112068000133.

Billings, J. M., and M. D. Parker, 2012: Evolution and maintenance of the 22–23 June 2003 nocturnal convection during BAMEX. *Wea. Forecasting*, **27**, 279–300, doi:10.1175/WAF-D-11-00056.1.

Bluestein, H. B., and M. H. Jain, 1985: Formation of mesoscale lines of precipitation: Severe squall lines in Oklahoma during the spring. *J. Atmos. Sci.*, **42**, 1711–1732, doi:10.1175/1520-0469(1985)042<1711:FOMLOP>2.0.CO;2.

Böing, S. J., H. J. J. Jonker, A. P. Siebesma, and W. W. Grabowski, 2012: Influence of the subcloud layer on the development of a deep convective ensemble. *J. Atmos. Sci.*, **69**, 2682–2698, doi:10.1175/JAS-D-11-0317.1.

Bretherton, C. S., P. N. Blossey, and M. Khairoutdinov, 2005: An energy-balance analysis of deep convective self-aggregation above uniform SST. *J. Atmos. Sci.*, **62**, 4273–4292, doi:10.1175/JAS3614.1.

Britter, R. E., and J. E. Simpson, 1978: Experiments on the dynamics of a gravity current head. *J. Fluid Mech.*, **88**, 223–240, doi:10.1017/S0022112078002074.

Bryan, G., D. Ahijevych, C. Davis, S. Trier, and M. Weisman, 2005: Observations of cold pool properties in mesoscale convective systems during BAMEX. Preprints, *11th Conf. on Mesoscale Processes*, Albuquerque, NM, Amer. Meteor. Soc., JP5J.12.

.

Bryan, G. H., J. C. Knievel, and M. D. Parker, 2006: A multimodel assessment of RKW theory's relevance to squall-line characteristics. *Mon. Wea. Rev.*, **134**, 2772–2792, doi:10.1175/MWR3226.1.

Bryan, G. H., and M. D. Parker, 2010: Observations of a squall line and its near environment using high-frequency rawinsonde launches during VORTEX2. *Mon. Wea. Rev.*, **138**, 4076–4097, doi:10.1175/2010MWR3359.1.

Bryan, G. H., and R. Rotunno, 2014: Gravity currents in confined channels with environmental shear. *J. Atmos. Sci.*, **71**, 1121–1142, doi:10.1175/JAS-D-13-0157.1.

Bryan, G. H., J. C. Wyngaard, and J. M. Fritsch, 2003: Resolution requirements for the simulation of deep moist convection. *Mon. Wea. Rev.*, **131**, 2394–2416, doi:10.1175/1520-0493(2003)131<2394:RRFTSO>2.0.CO;2.

Byers, H. R., and R. R. Braham Jr., 1949: The Thunderstorm. U.S. Govt. Printing Office, 287 pp.

Cantero, M. I., S. Balachandar, M. H. García, and D. Bock, 2008: Turbulent structures in planar gravity currents and their influence on the flow dynamics. *J. Geophys. Res.*, **113**, C08018, doi:10.1029/2007JC004645.

Carbone, R. E., J. W. Wilson, T. D. Keenan, and J. M. Hacker, 2000: Tropical island convection in the absence of significant topography. Part I: Life cycle of diurnally forced convection. *Mon. Wea. Rev.*, **128**, 3459–3480, doi:10.1175/1520-0493(2000)128<3459:TICITA>2.0.CO;2.

Charba, J., 1974: Application of gravity current model to analysis of squall-line gust front. *Mon. Wea. Rev.*, **102**, 140–156, doi:10.1175/1520-0493(1974)102<0140:AOGCMT>2.0.CO;2.

Chuda, T., H. Niino, K. Yoneyama, M. Katsumata, T. Ushiyama, and O. Tsukamoto, 2008: A statistical analysis of surface turbulent heat flux enhancements due to precipitating clouds observed in the tropical western Pacific. *J. Meteor. Soc. Japan*, **86**, 439–457, doi:10.2151/jmsj.86.439.

Computational and Information Systems Library, 2012: Yellowstone: IBM iDataPlex System (University Community Computing). Boulder, CO: National Center for Atmospheric Research, http://n2t.net/ark:/85065/d7wd3xhc.

Cotton, W. R., and Coauthors, 2003: RAMS 2001: Current status and future directions. *Meteor. Atmos. Phys.*, **82**, 5–29, doi:10.1007/s00703-001-0584-9.

Couvreux, F., C. Rio, F. Guichard, M. Lothon, G. Canut, D. Bouniol, and A. Gounou, 2012: Initiation of daytime local convection in a semi-arid region analysed with high-resolution simulations and AMMA observations. *Quart. J. Roy. Meteor. Soc.*, **138**, 56–71, doi:10.1002/qj.903.

Crook, N. A., and M. W. Moncrieff, 1988: The effect of large-scale convergence on the generation and maintenance of deep moist convection. *J. Atmos. Sci.*, **45**, 3606–3624, doi:10.1175/1520-0469(1988)045<3606:TEOLSC>2.0.CO;2.

Dawson, D. T., M. Xue, J. A. Milbrandt, and M. K. Yau, 2010: Comparison of evaporation and cold pool development between single-moment and multimoment bulk microphysics schemes in idealized simulations of tornadic thunderstorms. *Mon. Wea. Rev.*, **138**, 1152–1171, doi:10.1175/2009MWR2956.1.

de Szoeke, S. P., E. D. Skyllingstad, P. Zuidema, and A. S. Chandra, 2017: Cold pools and their influence on the tropical marine boundary layer. *J. Atmos. Sci.*, **74**, 1149–1168, doi:10.1175/JAS-D-16-0264.1.

Deardorff, J. W., 1972: Numerical investigation of neutral and unstable planetary boundary layers. *J. Atmos. Sci.*, **29**, 91–115, doi:10.1175/1520-0469(1972)029<0091:NIONAU>2.0.CO;2.

Del Genio, A. D., J. Wu, and Y. Chen, 2012: Characteristics of mesoscale organization in WRF simulations of convection during TWP-ICE. *J. Climate*, **25**, 5666–5688, doi:10.1175/JCLI-D-11-00422.1.

Del Genio, A. D., J. Wu, A. B. Wolf, Y. Chen, M.-S. Yao, and D. Kim, 2015: Constraints on cumulus parameterization from simulations of observed MJO events. *J. Climate*, **28**, 6419–6442, doi:10.1175/JCLI-D-14-00832.1.

DeMott, P. J., and Coauthors, 2010: Predicting global atmospheric ice nuclei distributions and their impacts on climate. *Proc. Natl. Acad. Sci. U.S.A.*, **107**, 11217–11222, doi:10.1073/pnas.0910818107.

Doswell, C. A., 1987: The distinction between large-scale and mesoscale contribution to severe convection: A case study example. *Wea. Forecasting*, **2**, 3–16, doi:10.1175/1520-0434(1987)002<0003:TDBLSA>2.0.CO;2.

Doswell, C. A., and P. M. Markowski, 2004: Is buoyancy a relative quantity? *Mon. Wea. Rev.*, **132**, 853–863, doi:10.1175/1520-0493(2004)132<0853:IBARQ>2.0.CO;2.

Drager, A. J., and S. C. van den Heever, 2017: Characterizing convective cold pools. *J. Adv. Model. Earth Syst.*, **9**, 1091–1115, doi:10.1002/2016MS000788.

Droegemeier, K. K., and R. B. Wilhelmson, 1985: Three-dimensional numerical modeling of convection produced by interacting thunderstorm outflows. Part I: Control simulation and low-level moisture variations. *J. Atmos. Sci.*, **42**, 2381–2403, doi:10.1175/1520-0469(1985)042<2381:TDNMOC>2.0.CO;2.

Droegemeier, K. K., and R. B. Wilhelmson, 1987: Numerical simulation of thunderstorm outflow dynamics. Part I: Outflow sensitivity experiments and turbulence dynamics. *J. Atmos. Sci.*, **44**, 1180–1210, doi:10.1175/1520-0469(1987)044<1180:NSOTOD>2.0.CO;2.

Emanuel, K. A., 1994: *Atmospheric Convection*. Oxford University Press, 580 pp.

Engerer, N. A., D. J. Stensrud, and M. C. Coniglio, 2008: Surface characteristics of observed cold pools. *Mon. Wea. Rev.*, **136**, 4839–4849, doi:10.1175/2008MWR2528.1.

Feng, Z., S. Hagos, A. K. Rowe, C. D. Burleyson, M. N. Martini, and S. P. de Szoeke, 2015: Mechanisms of convective cloud organization by cold pools over tropical warm ocean during the AMIE/DYNAMO field campaign. *J. Adv. Model. Earth Syst.*, **7**, 357–381, doi:10.1002/2014MS000384.

Fujita, T. T., 1978: Manual of downburst identification for project NIMROD. SMRP Research Paper 156, University of Chicago, 104 pp.

Garcia-Carreras, L., and Coauthors, 2013: The impact of convective cold pool outflows on model biases in the Sahara. *Geophys. Res. Lett.*, **40**, 1647–1652, doi:10.1002/grl.50239.

Gentine, P., A. Garelli, S. Park, J. Nie, G. Torri, and Z. Kuang, 2016: Role of surface heat fluxes underneath cold pools. *Geophys. Res. Lett.*, **43**, 874–883, doi:10.1002/2015GL067262.

Gilmore, M. S., J. M. Straka, and E. N. Rasmussen, 2004: Precipitation and evolution sensitivity in simulated deep convective storms: Comparisons between liquid-only and simple ice and liquid phase microphysics. *Mon. Wea. Rev.*, **132**, 1897–1916, doi:10.1175/1520-0493(2004)132<1897:PAESIS>2.0.CO;2.

Goff, R. C., 1976: Vertical structure of thunderstorm outflows. *Mon. Wea. Rev.*, **104**, 1429–1440, doi:10.1175/1520-0493(1976)104<1429:VSOTO>2.0.CO;2.

Grabowski, W. W., and M. W. Moncrieff, 2001: Large-scale organization of tropical convection in two-dimensional explicit numerical simulations. *Quart. J. Roy. Meteor. Soc.*, **127**, 445–468, doi:10.1002/qj.49712757211.

Grandpeix, J.-Y., and J.-P. Lafore, 2010: A density current parameterization coupled with Emanuel's convection scheme. Part I: The models. *J. Atmos. Sci.*, **67**, 881–897, doi:10.1175/2009JAS3044.1.

Grant, L. D., T. P. Lane, and S. C. van den Heever, 2017a: The role of cold pools in tropical oceanic convective systems. *J. Atmos. Sci.*, submitted.

Grant, L. D., and S. C. van den Heever, 2014: Aerosol-cloud-land surface interactions within tropical sea breeze convection. *J. Geophys. Res. Atmos.*, **119**, 8340–8361, doi:10.1002/2014JD021912.

Grant, L. D., and S. C. van den Heever, 2015: Cold pool and precipitation responses to aerosol loading: Modulation by dry layers. *J. Atmos. Sci.*, **72**, 1398–1408, doi:10.1175/JAS-D-14-0260.1.

Grant, L. D., and S. C. van den Heever, 2016: Cold pool dissipation. *J. Geophys. Res. Atmos.*, **121**, 1138–1155, doi:10.1002/2015JD023813.

Grant, L. D., and S. C. van den Heever, 2017: Cold pool - land surface interactions in a dry continental environment. *Geophys. Res. Lett.*, submitted.

Grant, L. D., and Coauthors, 2017b: Midlatitude cold pool variability from C3LOUD-Ex observations. *J. Atmos. Sci.*, in prep.

Harrington, J. Y., 1997: The effects of radiative and microphysical processes on simulated warm and transition season Arctic stratus. Dissertation, Colorado State University, 289 pp.

Hartmann, D. L., 1994: *Global Physical Climatology*. Academic Press, 411 pp.

Held, I. M., R. S. Hemler, and V. Ramaswamy, 1993: Radiative-convective equilibrium with explicit two-dimensional moist convection. *J. Atmos. Sci.*, **50**, 3909–3927, doi:10.1175/1520-0469(1993)050<3909:RCEWET>2.0.CO;2.

Heymsfield, G. M., L. Tian, A. J. Heymsfield, L. Li, and S. Guimond, 2010: Characteristics of deep tropical and subtropical convection from nadir-viewing high-altitude airborne Doppler radar. *J. Atmos. Sci.*, **67**, 285–308, doi:10.1175/2009JAS3132.1.

Hill, G. E., 1974: Factors controlling the size and spacing of cumulus clouds as revealed by numerical experiments. *J. Atmos. Sci.*, **31**, 646–673, doi:10.1175/1520-0469(1974)031<0646:FCTSAS>2.0.CO;2.

Hohenegger, C., and C. S. Bretherton, 2011: Simulating deep convection with a shallow convection scheme. *Atmos. Chem. Phys.*, **11**, 10389–10406, doi:10.5194/acp-11-10389-2011.

Jabouille, P., J. L. Redelsperger, and J. P. Lafore, 1996: Modification of surface fluxes by atmospheric convection in the TOGA COARE region. *Mon. Wea. Rev.*, **124**, 816–837, doi:10.1175/1520-0493(1996)124<0816:MOSFBA>2.0.CO;2.

Jeevanjee, N., and D. M. Romps, 2013: Convective self-aggregation, cold pools, and domain size. *Geophys. Res. Lett.*, **40**, 994–998, doi:10.1002/grl.50204.

Jin, Y., S. E. Koch, Y.-L. Lin, F. M. Ralph, and C. Chen, 1996: Numerical simulations of an observed gravity current and gravity waves in an environment characterized by complex stratification and shear. *J. Atmos. Sci.*, **53**, 3570–3588, doi:10.1175/1520-0469(1996)053<3570:NSOAOG>2.0.CO;2.

Johns, R. H., and C. A. Doswell, 1992: Severe local storms forecasting. *Wea. Forecasting*, **7**, 588–612, doi:10.1175/1520-0434(1992)007<0588:SLSF>2.0.CO;2.

Johnson, R. H., S. L. Aves, P. E. Ciesielski, and T. D. Keenan, 2005: Organization of oceanic convection during the onset of the 1998 east Asian summer monsoon. *Mon. Wea. Rev.*, **133**, 131–148, doi:10.1175/MWR-2843.1.

Johnson, R. H., and M. E. Nicholls, 1983: A composite analysis of the boundary layer accompanying a tropical squall line. *Mon. Wea. Rev.*, **111**, 308–319, doi:10.1175/1520-0493(1983)111<0308:ACAOTB>2.0.CO;2.

Keenan, T. D., and R. E. Carbone, 1992: A preliminary morphology of precipitation systems in tropical northern Australia. *Quart. J. Roy. Meteor. Soc.*, **118**, 283–326, doi:10.1002/qj.49711850406.

Keulegan, G. H., 1958: The motion of saline fronts in still water. U.S. National Bureau of Standards Report No. 5831.

Khairoutdinov, M., and D. Randall, 2006: High-resolution simulation of shallow-to-deep convection transition over land. *J. Atmos. Sci.*, **63**, 3421–3436, doi:10.1175/JAS3810.1.

Kingsmill, D. E., 1995: Convection initiation associated with a sea-breeze front, a gust front, and their collision. *Mon. Wea. Rev.*, **123**, 2913–2933, doi:10.1175/1520-0493(1995)123<2913:CIAWAS>2.0.CO;2.

Klemp, J. B., and R. B. Wilhelmson, 1978: The simulation of three-dimensional convective storm dynamics. *J. Atmos. Sci.*, **35**, 1070–1096, doi:10.1175/1520-0469(1978)035<1070:TSOTDC>2.0.CO;2.

Lac, C., J.-P. Lafore, and J.-L. Redelsperger, 2002: Role of gravity waves in triggering deep convection during TOGA COARE. *J. Atmos. Sci.*, **59**, 1293–1316, doi:10.1175/1520-0469(2002)059<1293:ROGWIT>2.0.CO;2.

Lane, T. P., and M. W. Moncrieff, 2008: Stratospheric gravity waves generated by multiscale tropical convection. *J. Atmos. Sci.*, **65**, 2598–2614, doi:10.1175/2007JAS2601.1.

Lane, T. P., and M. W. Moncrieff, 2015: Long-lived mesoscale systems in a low–convective inhibition environment. Part I: Upshear propagation. *J. Atmos. Sci.*, **72**, 4297–4318, doi:10.1175/JAS-D-15-0073.1.

Lane, T. P., and M. J. Reeder, 2001: Convectively generated gravity waves and their effect on the cloud environment. *J. Atmos. Sci.*, **58**, 2427–2440, doi:10.1175/1520-0469(2001)058<2427:CGGWAT>2.0.CO;2.

Lane, T. P., and F. Zhang, 2011: Coupling between gravity waves and tropical convection at mesoscales. *J. Atmos. Sci.*, **68**, 2582–2598, doi:10.1175/2011JAS3577.1.

Langhans, W., and D. M. Romps, 2015: The origin of water vapor rings in tropical oceanic cold pools. *Geophys. Res. Lett.*, **42**, 7825–7834, doi:10.1002/2015GL065623.

Lapworth, A., 2000: Observations of atmospheric density currents using a tethered balloon-borne turbulence probe system. *Quart. J. Roy. Meteor. Soc.*, **126**, 2811–2850, doi:10.1002/qj.49712656911.

Lareau, N. P., and J. D. Horel, 2015: Turbulent erosion of persistent cold-air pools: Numerical simulations. *J. Atmos. Sci.*, **72**, 1409–1427, doi:10.1175/JAS-D-14-0173.1.

Lee, T. R., M. Buban, E. Dumas, and C. B. Baker, 2017: A new technique to estimate sensible heat fluxes around micrometeorological towers using small unmanned aircraft systems. *J. Atmos. Oceanic Technol.*, **34**, 2103–2112, doi:10.1175/JTECH-D-17-0065.1.

Lilly, D. K., 1962: On the numerical simulation of buoyant convection. *Tellus*, **14**, 148–172, doi:10.1111/j.2153-3490.1962.tb00128.x.

Lima, M. A., and J. W. Wilson, 2008: Convective storm initiation in a moist tropical environment. *Mon. Wea. Rev.*, **136**, 1847–1864, doi:10.1175/2007MWR2279.1.

Linden, P. F., and J. E. Simpson, 1986: Gravity-driven flows in a turbulent fluid. *J. Fluid Mech.*, **172**, 481–497, doi:10.1017/S0022112086001829.

Liu, C., and M. W. Moncrieff, 1996: A numerical study of the effects of ambient flow and shear on density currents. *Mon. Wea. Rev.*, **124**, 2282–2303, doi:10.1175/1520-0493(1996)124<2282:ANSOTE>2.0.CO;2.

Liu, C., and M. W. Moncrieff, 2000: Simulated density currents in idealized stratified environments. *Mon. Wea. Rev.*, **128**, 1420–1437, doi:10.1175/1520-0493(2000)128<1420:SDCIIS>2.0.CO;2.

Liu, C., and M. W. Moncrieff, 2004: Effects of convectively generated gravity waves and rotation on the organization of convection. *J. Atmos. Sci.*, **61**, 2218–2227, doi:10.1175/1520-0469(2004)061<2218:EOCGGW>2.0.CO;2.

Liu, C., and M. W. Moncrieff, 2017: Shear-parallel mesoscale convective systems in a moist low-inhibition Meiyu front environmen. *J. Atmos. Sci.*, in press, doi:10.1175/JAS-D-17-0121.1.

Liu, C., and E. Zipser, 2013: Regional variation of morphology of organized convection in the tropics and subtropics. *J. Geophys. Res. Atmos.*, **118**, 1–14, doi:10.1029/2012JD018409.

Louis, J.-F., 1979: A parametric model of vertical eddy fluxes in the atmosphere. *Boundary Layer Meteor.*, **17**, 187–202, doi:10.1007/BF00117978.

Mahrt, L., 1991: Boundary-layer moisture regimes. *Quart. J. Roy. Meteor. Soc.*, **117**, 151–176, doi:10.1002/qj.49711749708.

Mallet, M., P. Tulet, D. Serça, F. Solmon, O. Dubovik, J. Pelon, V. Pont, and O. Thouron, 2009: Impact of dust aerosols on the radiative budget, surface heat fluxes, heating rate profiles and convective activity over West Africa during March 2006. *Atmos. Chem. Phys.*, **9**, 7143–7160, doi:10.5194/acpd-9-2967-2009.

Manabe, S., and R. F. Strickler, 1964: Thermal equilibrium of the atmosphere with a convective adjustment. *J. Atmos. Sci.*, **21**, 361–385, doi:10.1175/1520-0469(1964)021<0361:TEOTAW>2.0.CO;2.

Mapes, B. E., 1993: Gregarious tropical convection. *J. Atmos. Sci.*, **50**, 2026–2037, doi:10.1175/1520-0469(1993)050<2026:GTC>2.0.CO;2.

Mapes, B. E., 2000: Convective inhibition, subgrid-scale triggering energy, and stratiform instability in a toy tropical wave model. *J. Atmos. Sci.*, **57**, 1515–1535, doi:10.1175/1520-0469(2000)057<1515:CISSTE>2.0.CO;2.

Marsham, J. H., and Coauthors, 2013: Meteorology and dust in the central Sahara: Observations from Fennec supersite-1 during the June 2011 Intensive Observation Period. *J. Geophys. Res. Atmos.*, **118**, 4069–4089, doi:10.1002/jgrd.50211.

Martner, B. E., 1997: Vertical velocities in a thunderstorm gust front and outflow. *J. Appl. Meteor.*, **36**, 615–622, doi:10.1175/1520-0450(1997)036<0615:VVIATG>2.0.CO;2.

McGee, C. J., and S. C. van den Heever, 2014: Latent heating and mixing due to entrainment in tropical deep convection. *J. Atmos. Sci.*, **71**, 816–832, doi:10.1175/JAS-D-13-0140.1.

Mellado, J. P., M. Puche, and C. C. van Heerwaarden, 2017: Moisture statistics in free convective boundary layers growing into linearly stratified atmospheres. *Quart. J. Roy. Meteor. Soc.*, **143**, 2403–2419, doi:10.1002/qj.3095.

Meyers, M. P., R. L. Walko, J. Y. Harrington, and W. R. Cotton, 1997: New RAMS cloud microphysics parameterization. Part II: The two-moment scheme. *Atmos. Res.*, **45**, 3–39, doi:10.1016/S0169-8095(97)00018-5.

Middleton, G. V., 1966: Experiments on density and turbidity currents: I. Motion of the head. *Can. J. Earth Sci.*, **3**, 523–546, doi:10.1139/e66-038.

Miller, S. D., A. P. Kuciauskas, M. Liu, Q. Ji, J. S. Reid, D. W. Breed, A. L. Walker, and A. Al Mandoos, 2008: Haboob dust storms of the southern Arabian Peninsula. *J. Geophys. Res.*, **113**, D01202, doi:10.1029/2007JD008550.

Moncrieff, M. W., and T. P. Lane, 2015: Long-lived mesoscale systems in a low–convective inhibition environment. Part II: Downshear propagation. *J. Atmos. Sci.*, **72**, 4319–4336, doi:10.1175/JAS-D-15-0074.1.

Moncrieff, M. W., and M. J. Miller, 1976: The dynamics and simulation of tropical cumulonimbus and squall lines. *Quart. J. Roy. Meteor. Soc.*, **102**, 373–394, doi:10.1002/qj.49710243208.

Morrison, H., 2012: On the robustness of aerosol effects on an idealized supercell storm simulated with a cloud system-resolving model. *Atmos. Chem. Phys.*, **12**, 7689–7705, doi:10.5194/acp-12-7689-2012.

Morrison, T. J., M. Calaf, H. J. S. Fernando, T. a. Price, and E. R. Pardyjak, 2017: A methodology for computing spatially and temporally varying surface sensible heat flux from thermal imagery. *Quart. J. Roy. Meteor. Soc.*, **143**, 2616–2624, doi:10.1002/qj.3112.

Muller, C., and S. Bony, 2015: What favors convective aggregation and why? *Geophys. Res. Lett.*, **42**, 5626–5634, doi:10.1002/2015GL064260.

Mueller, C. K., and R. E. Carbone, 1987: Dynamics of a thunderstorm outflow. *J. Atmos. Sci.*, **44**, 1879–1898, doi:10.1175/1520-0469(1987)044<1879:DOATO>2.0.CO;2.

Nesbitt, S. W., R. Cifelli, and S. A. Rutledge, 2006: Storm morphology and rainfall characteristics of TRMM precipitation features. *Mon. Wea. Rev.*, **134**, 2702–2721, doi:10.1175/MWR3200.1.

Nesbitt, S. W., E. J. Zipser, and D. J. Cecil, 2000: A census of precipitation features in the tropics using TRMM: Radar, ice scattering, and lightning observations. *J. Climate*, **13**, 4087–4106, doi:10.1175/1520-0442(2000)013<4087:ACOPFI>2.0.CO;2.

Nicholls, M. E., R. H. Johnson, and W. R. Cotton, 1988: The sensitivity of two-dimensional simulations of tropical squall lines to environmental profiles. *J. Atmos. Sci.*, **45**, 3625–3649, doi:10.1175/1520-0469(1988)045<3625:TSOTDS>2.0.CO;2.

Park, S., 2014: A unified convection scheme (UNICON). Part I: Formulation. *J. Atmos. Sci.*, **71**, 3902–3930, doi:10.1175/JAS-D-13-0233.1.

Parker, M. D., and R. H. Johnson, 2004a: Simulated convective lines with leading precipitation. Part I: Governing dynamics. *J. Atmos. Sci.*, **61**, 1637–1655, doi:10.1175/1520-0469(2004)061<1637:SCLWLP>2.0.CO;2.

Parker, M. D., and R. H. Johnson, 2004b: Structures and dynamics of quasi-2D mesoscale convective systems. *J. Atmos. Sci.*, **61**, 545–567, doi:10.1175/1520-0469(2004)061<0545:SADOQM>2.0.CO;2.

Peters, K., and C. Hohenegger, 2017: On the dependence of squall-line characteristics on surface conditions. *J. Atmos. Sci.*, **74**, 2211–2228, doi:10.1175/JAS-D-16-0290.1.

Plant, R. S., and G. J. Keith, 2007: Occurrence of Kelvin-Helmholtz billows in sea-breeze circulations. *Boundary Layer Meteor.*, **122**, 1–15, doi:10.1007/s10546-006-9089-x.

Posselt, D. J., S. C. van den Heever, and G. L. Stephens, 2008: Trimodal cloudiness and tropical stable layers in simulations of radiative convective equilibrium. *Geophys. Res. Lett.*, **35**, L08802, doi:10.1029/2007GL033029.

Posselt, D. J., S. van den Heever, G. Stephens, and M. R. Igel, 2012: Changes in the interaction between tropical convection, radiation, and the large-scale circulation in a warming environment. *J. Climate*, **25**, 557–571, doi:10.1175/2011JCLI4167.1.

Purdom, J. F. W., 1976: Some uses of high-resolution GOES imagery in the mesoscale forecasting of convection and its behavior. *Mon. Wea. Rev.*, **104**, 1474–1483, doi:10.1175/1520-0493(1976)104<1474:SUOHRG>2.0.CO;2.

Purdom, J. F. W., 1982: Subjective interpretation of geostationary satellite data for nowcasting. *Nowcasting*, K. Browning, Ed., Academic Press, 149–166.

Qian, L., G. S. Young, and W. M. Frank, 1998: A convective wake parameterization scheme for use in general circulation models. *Mon. Wea. Rev.*, **126**, 456–469, doi:10.1175/1520-0493(1998)126<0456:ACWPSF>2.0.CO;2.

Ralph, F. M., C. Mazaudier, M. Crochet, and S. V. Venkateswaran, 1993: Doppler sodar and radar wind-profiler observations of gravity-wave activity associated with a gravity current. *Mon. Wea. Rev.*, **121**, 444–463, doi:10.1175/1520-0493(1993)121<0444:DSARWP>2.0.CO;2.

Rauber, R. M., and Coauthors, 2007: Rain in shallow Cumulus over the Ocean: The RICO campaign. *Bull. Amer. Meteor. Soc.*, **88**, 1912–1928, doi:10.1175/BAMS-88-12-1912.

Raymond, D. J., 1994: Convective processes and tropical atmospheric circulations. *Quart. J. Roy. Meteor. Soc.*, **120**, 1431–1455, doi:10.1002/qj.49712052002.

Raymond, D. J., 1995: Regulation of moist convection over the west Pacific warm pool. *J. Atmos. Sci.*, **52**, 3945–3959, doi:10.1175/1520-0469(1995)052<3945:ROMCOT>2.0.CO;2.

Riehl, H., and J. S. Malkus, 1958: On the heat balance in the Equatorial trough zone. *Geophysica*, **6**, 503–538.

Rio, C., F. Hourdin, J.-Y. Grandpeix, and J.-P. Lafore, 2009: Shifting the diurnal cycle of parameterized deep convection over land. *Geophys. Res. Lett.*, **36**, L07809, doi:10.1029/2008GL036779.

Robe, F. R., and K. A. Emanuel, 2001: The effect of vertical wind shear on radiative–convective equilibrium states. *J. Atmos. Sci.*, **58**, 1427–1445, doi:10.1175/1520-0469(2001)058<1427:TEOVWS>2.0.CO;2.

Roberts, A., and P. Knippertz, 2012: Haboobs: Convectively generated dust storms in West Africa. *Weather*, **67**, 311–316, doi:10.1002/wea.1968.

Robinson, F. J., M. D. Patterson, and S. C. Sherwood, 2013: A numerical modeling study of the propagation of idealized sea-breeze density currents. *J. Atmos. Sci.*, **70**, 653–668, doi:10.1175/JAS-D-12-0113.1.

Rooney, G. G., 2015: Descent and spread of negatively buoyant thermals. *J. Fluid Mech.*, **780**, 457–479, doi:10.1017/jfm.2015.484.

Ross, A. N., A. M. Tompkins, and D. J. Parker, 2004: Simple models of the role of surface fluxes in convective cold pool evolution. *J. Atmos. Sci.*, **61**, 1582–1595, doi:10.1175/1520-0469(2004)061<1582:SMOTRO>2.0.CO;2.

Rotunno, R., J. B. Klemp, and M. L. Weisman, 1988: A theory for strong, long-lived squall lines. *J. Atmos. Sci.*, **45**, 463–485, doi:10.1175/1520-0469(1988)045<0463:ATFSLL>2.0.CO;2.

Saleeby, S. M., and W. R. Cotton, 2004: A large-droplet mode and prognostic number concentration of cloud droplets in the Colorado State University Regional Atmospheric Modeling System (RAMS). Part I: Module descriptions and supercell test simulations. *J. Appl. Meteor.*, **43**, 182–195, doi:10.1175/1520-0450(2004)043<0182:ALMAPN>2.0.CO;2.

Saleeby, S. M., and W. R. Cotton, 2008: A binned approach to cloud-droplet riming implemented in a bulk microphysics model. *J. Appl. Meteor. Climatol.*, **47**, 694–703, doi:10.1175/2007JAMC1664.1.

Saleeby, S. M., and S. C. van den Heever, 2013: Developments in the CSU-RAMS aerosol model: Emissions, nucleation, regeneration, deposition, and radiation. *J. Appl. Meteor. Climatol.*, **52**, 2601–2622, doi:10.1175/JAMC-D-12-0312.1.

Saxen, T. R., and S. A. Rutledge, 1998: Surface fluxes and boundary layer recovery in TOGA COARE: Sensitivity to convective organization. *J. Atmos. Sci.*, **55**, 2763–2781, doi:10.1175/1520-0469(1998)055<2763:SFABLR>2.0.CO;2.

Schlemmer, L., and C. Hohenegger, 2014: The formation of wider and deeper clouds as a result of cold-pool dynamics. *J. Atmos. Sci.*, **71**, 2842–2858, doi:10.1175/JAS-D-13-0170.1.

Schlemmer, L., and C. Hohenegger, 2016: Modifications of the atmospheric moisture field as a result of cold-pool dynamics. *Quart. J. Roy. Meteor. Soc.*, **142**, 30–42, doi:10.1002/qj.2625.

Schumacher, C., S. N. Stevenson, and C. R. Williams, 2015: Vertical motions of the tropical convective cloud spectrum over Darwin, Australia. *Quart. J. Roy. Meteor. Soc.*, **141**, 2277–2288, doi:10.1002/qj.2520.

Schumacher, R. S., 2015: Sensitivity of precipitation accumulation in elevated convective systems to small changes in low-level moisture. *J. Atmos. Sci.*, **72**, 2507–2524, doi:10.1175/JAS-D-14-0389.1.

Seigel, R. B., and S. C. van den Heever, 2012a: Dust lofting and ingestion by supercell storms. *J. Atmos. Sci.*, **69**, 1453–1473, doi:10.1175/JAS-D-11-0222.1.

Seigel, R. B., and S. C. van den Heever, 2012b: Simulated density currents beneath embedded stratified layers. *J. Atmos. Sci.*, **69**, 2192–2200, doi:10.1175/JAS-D-11-0255.1.

Seigel, R. B., and S. C. van den Heever, 2013: Squall-line intensification via hydrometeor recirculation. *J. Atmos. Sci.*, **70**, 2012–2031, doi:10.1175/JAS-D-12-0266.1.

Shige, S., and T. Satomura, 2001: Westward generation of eastward-moving tropical convective bands in TOGA COARE. *J. Atmos. Sci.*, **58**, 3724–3740, doi:10.1175/1520-0469(2001)058<3724:WGOEMT>2.0.CO;2.

Simpson, J. E., 1969: A comparison between laboratory and atmospheric density currents. *Quart. J. Roy. Meteor. Soc.*, **95**, 758–765, doi:10.1002/qj.49709540609.

Simpson, J. E., 1972: Effects of the lower boundary on the head of a gravity current. *J. Fluid Mech.*, **53**, 759–768, doi:10.1017/S0022112072000461.

Simpson, J., N. Westcott, R. Clerman, and R. A. Pielke, 1980: On cumulus mergers. *Arch. Meteor. Geophys. Bioklim.*, **29A,** 1–40.

Smagorinsky, J., 1963: General circulation experiments with the primitive equations. I. The basic experiment. *Mon. Wea. Rev.*, **91**, 99–164, doi:10.1175/1520-0493(1963)091<0099:GCEWTP>2.3.CO;2.

Soderholm, J., H. McGowan, H. Richter, K. Walsh, T. Weckwerth, and M. Coleman, 2016: The Coastal Convective Interactions Experiment (CCIE): Understanding the role of sea breezes for hailstorm hotspots in eastern Australia. *Bull. Amer. Meteor. Soc.*, **97**, 1687–1698, doi:10.1175/BAMS-D-14-00212.1.

Stephens, G. L., 1990: On the relationship between water vapor over the oceans and sea surface temperature. *J. Climate*, **3**, 634–645, doi:10.1175/1520-0442(1990)003<0634:OTRBWV>2.0.CO;2.

Stephens, G. L., S. van den Heever, and L. Pakula, 2008: Radiative–convective feedbacks in idealized states of radiative–convective equilibrium. *J. Atmos. Sci.*, **65**, 3899–3916, doi:10.1175/2008JAS2524.1.

Stephens, G. L., N. B. Wood, and L. A. Pakula, 2004: On the radiative effects of dust on tropical convection. *Geophys. Res. Lett.*, **31**, L23112, doi:10.1029/2004GL021342.

Storer, R. L., and S. C. van den Heever, 2013: Microphysical processes evident in aerosol forcing of tropical deep convective clouds. *J. Atmos. Sci.*, **70**, 430–446, doi:10.1175/JAS-D-12-076.1.

Storer, R. L., S. C. van den Heever, and G. L. Stephens, 2010: Modeling aerosol impacts on convective storms in different environments. *J. Atmos. Sci.*, **67**, 3904–3915, doi:10.1175/2010JAS3363.1.

Straka, J. M., R. B. Wilhelmson, L. J. Wicker, J. R. Anderson, and K. K. Droegemeier, 1993: Numerical solutions of a non-linear density current: A benchmark solution and comparisons. *Int. J. Numer. Methods Fluids*, **17**, 1–22, doi:10.1002/fld.1650170103.

Tan, J., C. Jakob, and T. P. Lane, 2013: On the identification of the large-scale properties of tropical convection using cloud regimes. *J. Climate*, **26**, 6618–6632, doi:10.1175/JCLI-D-12-00624.1.

Tao, W.-K., X. Li, A. Khain, T. Matsui, S. Lang, and J. Simpson, 2007: Role of atmospheric aerosol concentration on deep convective precipitation: Cloud-resolving model simulations. *J. Geophys. Res.*, **112**, D24S18, doi:10.1029/2007JD008728.

Terai, C. R., and R. Wood, 2013: Aircraft observations of cold pools under marine stratocumulus. *Atmos. Chem. Phys.*, **13**, 9899–9914, doi:10.5194/acp-13-9899-2013.

Thorpe, A. J., M. J. Miller, and M. W. Moncrieff, 1980: Dynamical models of two-dimensional downdraughts. *Quart. J. Roy. Meteor. Soc.*, **106**, 463–484, doi:10.1002/qj.49710644906.

Thorpe, A. J., M. J. Miller, and M. W. Moncrieff, 1982: Two-dimensional convection in non-constant shear: A model of mid-latitude squall lines. *Quart. J. Roy. Meteor. Soc.*, **108**, 739–762, doi:10.1002/qj.49710845802.

Tompkins, A. M., 2000: The impact of dimensionality on long-term cloud-resolving model simulations. *Mon. Wea. Rev.*, **128**, 1521–1535, doi:10.1175/1520-0493(2000)128<1521:TIODOL>2.0.CO;2.

Tompkins, A. M., 2001: Organization of tropical convection in low vertical wind shears: The role of cold pools. *J. Atmos. Sci.*, **58**, 1650–1672, doi:10.1175/1520-0469(2001)058<1650:OOTCIL>2.0.CO;2.

Tompkins, A. M., and G. C. Craig, 1998: Radiative–convective equilibrium in a three-dimensional cloud-ensemble model. *Quart. J. Roy. Meteor. Soc.*, **124**, 2073–2097, doi:10.1002/qj.49712455013.

Torri, G., and Z. Kuang, 2016a: A Lagrangian study of precipitation-driven downdrafts. *J. Atmos. Sci.*, **73**, 839–854, doi:10.1175/JAS-D-15-0222.1.

Torri, G., and Z. Kuang, 2016b: Rain evaporation and moist patches in tropical boundary layers. *Geophys. Res. Lett.*, **43**, 9895–9902, doi:10.1002/2016GL070893.

Torri, G., Z. Kuang, and Y. Tian, 2015: Mechanisms for convection triggering by cold pools. *Geophys. Res. Lett.*, **42**, 1943–1950, doi:10.1002/2015GL063227.

Trier, S. B., C. A. Davis, D. A. Ahijevych, M. L. Weisman, and G. H. Bryan, 2006: Mechanisms supporting long-lived episodes of propagating nocturnal convection within a 7-day WRF model simulation. *J. Atmos. Sci.*, **63**, 2437–2461, doi:10.1175/JAS3768.1.

Trier, S. B., J. H. Marsham, C. A. Davis, and D. A. Ahijevych, 2011: Numerical simulations of the postsunrise reorganization of a nocturnal mesoscale convective system during 13 June IHOP_2002. *J. Atmos. Sci.*, **68**, 2988–3011, doi:10.1175/JAS-D-11-0112.1.

Trier, S. B., W. C. Skamarock, M. A. LeMone, D. B. Parsons, and D. P. Jorgensen, 1996: Structure and evolution of the 22 February 1993 TOGA COARE squall line: Numerical simulations. *J. Atmos. Sci.*, **53**, 2861–2886, doi:10.1175/1520-0469(1996)053<2861:SAEOTF>2.0.CO;2.

Tulich, S. N., and B. E. Mapes, 2008: Multiscale convective wave disturbances in the tropics: Insights from a two-dimensional cloud-resolving model. *J. Atmos. Sci.*, **65**, 140–155, doi:10.1175/2007JAS2353.1.

van den Heever, S. C., and Coauthors, 2017: Diving into cold pools and flying into updrafts. *Bull. Amer. Meteor. Soc.*, in prep.

van den Heever, S. C., and W. R. Cotton, 2004: The impact of hail size on simulated supercell storms. *J. Atmos. Sci.*, **61**, 1596–1609, doi:10.1175/1520-0469(2004)061<1596:TIOHSO>2.0.CO;2.

van den Heever, S. C., and W. R. Cotton, 2007: Urban aerosol impacts on downwind convective storms. *J. Appl. Meteor. Climatol.*, **46**, 828–850, doi:10.1175/JAM2492.1.

Varble, A., and Coauthors, 2014: Evaluation of cloud-resolving and limited area model intercomparison simulations using TWP-ICE observations: 1. Deep convective updraft properties. *J. Geophys. Res. Atmos.*, **119**, 13,891-13,918, doi:10.1002/2013JD021371.

Wakimoto, R. M., 1982: The life cycle of thunderstorm gust fronts as viewed with Doppler radar and rawinsonde data. *Mon. Wea. Rev.*, **110**, 1060–1082, doi:10.1175/1520-0493(1982)110<1060:TLCOTG>2.0.CO;2.

Wakimoto, R. M., H. V. Murphey, A. Nester, D. P. Jorgensen, and N. T. Atkins, 2006: High winds generated by bow echoes. Part I: Overview of the Omaha bow echo 5 July 2003 storm during BAMEX. *Mon. Wea. Rev.*, **134**, 2793–2812, doi:10.1175/MWR3215.1.

Walko, R. L., and Coauthors, 2000a: Coupled atmosphere–biophysics–hydrology models for environmental modeling. *J. Appl. Meteor.*, **39**, 931–944, doi:10.1175/1520-0450(2000)039<0931:CABHMF>2.0.CO;2.

Walko, R. L., W. R. Cotton, G. Feingold, and B. Stevens, 2000b: Efficient computation of vapor and heat diffusion between hydrometeors in a numerical model. *Atmos. Res.*, **53**, 171–183, doi:10.1016/S0169-8095(99)00044-7.

Webster, P. J., and Coauthors, 2002: The JASMINE pilot study. *Bull. Amer. Meteor. Soc.*, **83**, 1603–1630, doi:10.1175/BAMS-83-11-1603.

Weisman, M. L., and R. Rotunno, 2004: "A theory for strong long-lived squall lines" revisited. *J. Atmos. Sci.*, **61**, 361–382, doi:10.1175/1520-0469(2004)061<0361:ATFSLS>2.0.CO;2.

Weisman, M. L., and R. Rotunno, 2005: Reply. *J. Atmos. Sci.*, **62**, 2997–3002, doi:10.1175/JAS3515.1.

Wilhelmson, R. B., and C.-S. Chen, 1982: A simulation of the development of successive cells along a cold outflow boundary. *J. Atmos. Sci.*, **39**, 1466–1483, doi:10.1175/1520-0469(1982)039<1466:ASOTDO>2.0.CO;2.

Wilson, J. W., and W. E. Schreiber, 1986: Initiation of convective storms at radar-observed boundary-layer convergence lines. *Mon. Wea. Rev.*, **114**, 2516–2536, doi:10.1175/1520-0493(1986)114<2516:IOCSAR>2.0.CO;2.

Wood, R., C. S. Bretherton, D. Leon, A. D. Clarke, P. Zuidema, G. Allen, and H. Coe, 2011: An aircraft case study of the spatial transition from closed to open mesoscale cellular convection over the Southeast Pacific. *Atmos. Chem. Phys.*, **11**, 2341–2370, doi:10.5194/acp-11-2341-2011.

Xu, Q., 1992: Density currents in shear flows – A two-fluid model. *J. Atmos. Sci.*, **49**, 511–524, doi:10.1175/1520-0469(1992)049<0511:DCISFA>2.0.CO;2.

Xu, Q., M. Xue, and K. K. Droegemeier, 1996: Numerical simulations of density currents in sheared environments within a vertically confined channel. *J. Atmos. Sci.*, doi:10.1175/1520-0469(1996)053<0770:NSODCI>2.0.CO;2.

Xue, M., 2002: Density currents in shear flows: Effects of rigid lid and cold-pool internal circulation, and application to squall line dynamics. *Quart. J. Roy. Meteor. Soc.*, **128**, 47–73, doi:10.1256/00359000260498789.

Young, G. S., S. M. Perugini, and C. W. Fairall, 1995: Convective wakes in the equatorial western Pacific during TOGA. *Mon. Wea. Rev.*, **123**, 110–123, doi:10.1175/1520-0493(1995)123<0110:CWITEW>2.0.CO;2.

Zuidema, P., and Coauthors, 2012: On trade wind cumulus cold pools. *J. Atmos. Sci.*, **69**, 258–280, doi:10.1175/JAS-D-11-0143.1.